Dynamics of coupled modes in two-section semiconductor lasers with saturable absorption

Finbarr O'Callaghan

NATIONAL UNIVERSITY OF IRELAND, CORK

FACULTY OF SCIENCE

DEPARTMENT OF PHYSICS

TYNDALL NATIONAL INSTITUTE

Thesis submitted for the degree of Doctor of Philosophy

1 October 2015

Supervisor: Dr Stephen O'Brien

Co-supervisor: Prof Eoin O'Reilly

Head of Department/School: Prof John McInerney

Research supported by SFI

Contents

I, Finbarr O'Callaghan, certify that this thesis is my own work and I have not obtained a degree in this university or elsewhere on the basis of the work submitted in this thesis.

Finbarr O'Callaghan

Acknowledgements

First and foremost, I thank my supervisor Stephen O'Brien, for all of his guidance, support, and patience during my studies. I also thank my co-supervisor Eoin O'Reilly. I would like to acknowledge those in Tyndall and the wider scientific and open source communities who helped out during my PhD.

I would like to thank my family and friends for their patience and unwavering support whilst I was in the process of "finishing up". I thank Irene Yeriskin for her patience and solidarity.

List of Publications

Papers

- F. O'Callaghan, S. Osborne, and S. O'Brien, "Dispersion-induced dynamics of coupled modes in a semiconductor laser with saturable absorption," *Phys. Rev. A*, vol. 89, 033848, 2014.
- F. O'Callaghan, D. Bitauld, and S. O'Brien, "Design optimization of passively mode-locked semiconductor lasers with intracavity grating spectral filters," *IEEE J. Quantum. Electron.*, vol. 50, 863, 2014.

Conference papers presented at OSA Integrated Photonics Research [IPR] San Diego 2014

- Finbarr O'Callaghan, David Bitauld, and Stephen O'Brien, "Mode-Locking of semiconductor lasers with intracavity grating spectral filters." doi:10.1364/IPRSN.2014.IW4A.2
- Finbarr O'Callaghan, David Bitauld, and Stephen O'Brien, "Distributed feedback grating filters for tailoring comb laser spectra." doi:10.1364/IPRSN.2014.IW4A.3

Conference talks

- Finbarr O'Callaghan, David Bitauld, Andreas Amann, Simon Osborne, and Stephen O'Brien, "Dynamics in two-mode diode lasers with saturable absorption", Semiconductor and Integrated OptoElectronics Conference [SIOE] Cardiff 2013.

Conference posters

- Finbarr O'Callaghan, David Bitauld, Andreas Amann, Simon Osborne, and Stephen O'Brien, "Modelling of Q-switching dynamics in two mode diode lasers with saturable absorption", Photonics Ireland 2011.

List of Acronyms

ML mode-locking

SP self-pulsation

FP Fabry-Pérot

CW continuous wave

QSML Q-switched mode-locking

HML Harmonic mode-locking

RF radio-frequency

WDM wave division multiplexing

SNR signal-to-noise ratio

HR high-reflection

LSA laser with saturable absorption

DDE delay-differential equation

DM discrete-mode

SN saddle-node (bifurcation)

H Hopf (bifurcation)

TC Transcritical (bifurcation)

CP Cusp (bifurcation)

RH Routh-Hurwitz

LC limit-cycle

PD period doubling

BT Bogdanov-Takens

Abstract

Semiconductor lasers have the potential to address a number of critical applications in advanced telecommunications and signal processing. These include applications that require pulsed output that can be obtained from self-pulsing and mode-locked states of two-section devices with saturable absorption. Many modern applications place stringent performance requirements on the laser source, and a thorough understanding of the physical mechanisms underlying these pulsed modes of operation is therefore highly desirable.

In this thesis, we present experimental measurements and numerical simulations of a variety of self-pulsation phenomena in two-section semiconductor lasers with saturable absorption. Our theoretical and numerical results will be based on rate equations for the field intensities and the carrier densities in the two sections of the device, and we establish typical parameter ranges and assess the level of agreement with experiment that can be expected from our models. For each of the physical examples that we consider, our model parameters are consistent with the physical net gain and absorption of the studied devices.

Following our introductory chapter, the first system that we consider is a two-section Fabry-Pérot laser. This example serves to introduce our method for obtaining model parameters from the measured material dispersion, and it also allows us to present a detailed discussion of the bifurcation structure that governs the appearance of self-pulsations in two-section devices. In the following two chapters, we present two distinct examples of experimental measurements from dual-mode two-section devices. In each case we have found that single mode self-pulsations evolve into complex coupled dual-mode states following a characteristic series of bifurcations. We present optical and mode resolved power spectra as well as a series of characteristic intensity time traces illustrating this progression for each example. Using the results from our study of a two-section Fabry-Pérot device as a guide, we find physically appropriate model parameters that provide qualitative agreement with our experimental results. We highlight the role played by material dispersion and the underlying single mode self-pulsing orbits in determining the observed dynamics, and we use numerical continuation methods to provide a global picture of the governing bifurcation structure.

In our concluding chapter we summarise our work, and we discuss how the presented results can inform the development of optimised mode-locked lasers for performance applications in integrated optics.

Chapter 1

Introduction

1.1 Self-pulsations and mode-locking of semiconductor lasers

Semiconductor lasers with saturable absorption have the potential to address a great number of applications in advanced telecommunications and signal processing. In particular, a number of applications such as time-division multiplexing and optical data storage require a compact and robust source of high-repetition rate optical pulses. Two mechanisms which allow for the generation of short and high-power optical pulses in semiconductor lasers are self-pulsations and mode-locking. These modes of operation are typically associated with different timescales, determined respectively by the relaxation frequency of the laser [GHz] and the round trip time in the cavity [10s - 100s GHz]. Many of the potential applications of self-pulsations (SPs), and of mode-locking (ML) in particular, place stringent performance requirements on the laser source. As a result, a thorough understanding of the physical mechanisms underlying these modes of operation is highly desirable.

The terminology used to describe the SP phenomenon is non standard and it is often referred to as passive Q-switching [1]. Regardless of the terminology however, the physical mechanism responsible for SPs and Q-switching is essentially the same. In both active and passive Q-switching the laser cavity begins in a highly lossy state (low Q). Because of the degradation of the resonator Q-factor in the presence of this large loss, the gain medium can be pumped to a high level without reaching laser threshold. By dynamically restoring the cavity Q to a large value, a high intensity pulse can be emitted by the active medium.

In an actively Q-switched system this transition is achieved by either mechanical or electrical means, while in a passively Q-switched system, the transition is achieved by saturation of the resonator absorption by the intracavity field intensity. In this case the

dynamics are referred to as SPs because the system itself favours periodic saturation of the absorption and its recovery leading to pulsed intensity output [2]. Mathematically, this tendency is expressed as an instability of the continuous wave (CW) output leading to undamped relaxation oscillations [3]. These pulsations can also be interpreted as hamiltonians in a Toda-like potential [4, 5].

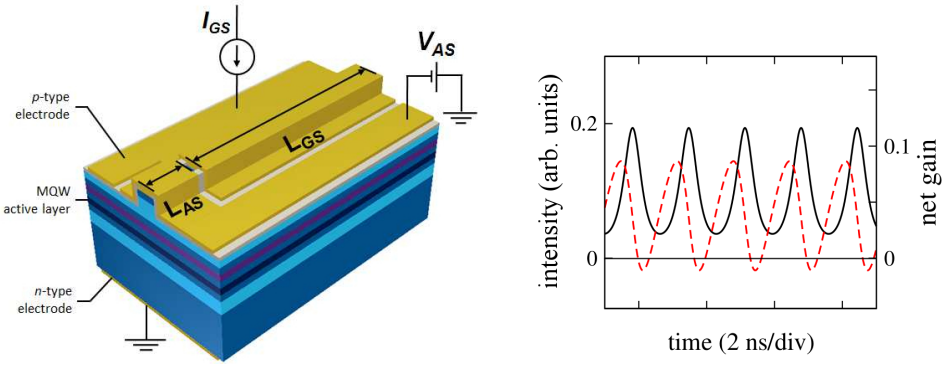

Figure 1.1: Left Panel: Schematic of a two-section device [6]. Right panel: Numerical simulation of self-pulsations generated by passive Q-switching of a two-section semiconductor laser. The solid line is the laser intensity, and the dashed line is the net gain of the cavity.

Self-pulsating semiconductor lasers typically employ a short reverse biased section that functions as a saturable absorber. Once the resonator is in a state of low loss, the stored energy is extracted efficiently in the form of a laser pulse. The diminished intracavity intensity then leads the absorption to recover, returning the cavity to the low-Q state, and the process thereby repeats itself. A schematic picture of a two-section semiconductor ridge-waveguide Fabry-Pérot laser is shown in the left panel of Fig. 1.1 [6]. The right hand panel of Fig. 1.1 shows the relationship between the net gain in the laser cavity and the dynamics of the intensity. One can see that the net gain alternates between a high and a low-loss state, which leads to the generation of a train of pulses in the time-domain. This example is taken near the onset of SPs, which results in a relatively weak modulation of the intensity. These simulations were performed using a delay-differential model of a two-section semiconductor laser that we will introduce in Chapter 2.

Self-pulsating semiconductor lasers are promising for a number of applications including high-power pulse generation [7], optical data storage [8, 9, 10], and optical signal processing [11]. This is primarily because SPs provide a very simple means to generate short optical pulses with a low-cost and mechanically stable device.

Furthermore, pulsed operation provides a mechanism to concentrate pump energy into short pulses and thereby increase peak power output. With pulsed output intensity the device spends a considerable amount of time in the 'off' state, which makes it more difficult for a given intensity perturbation to destabilise the system [13]. In optical data storage there is considerable interest in GaN based self-pulsating devices, which have the potential to become enabling components for next generation technology replacing

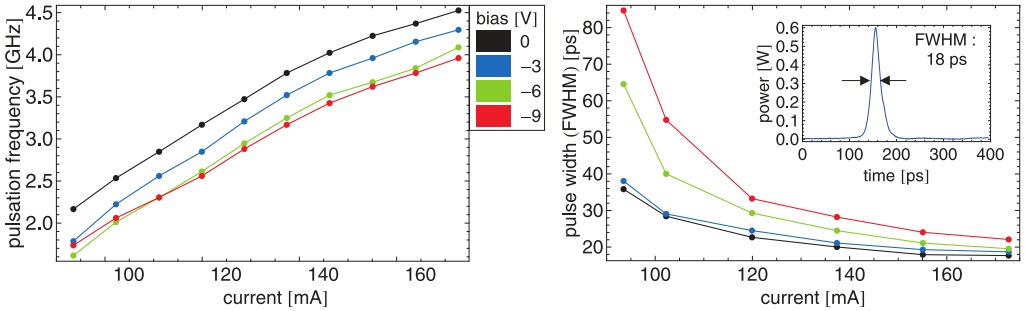

Figure 1.2: Left panel: Oscillation frequency of pulses as a function of pump current for a series of bias voltages. Right panel: Pulse width a function of pump current for the same voltages. The inset shows the pulse shape at 0 V absorber bias and 173 mA gain section current [12].

the Blu-ray optical data storage standard [12]. Results from [12] in Fig. 1.2 show the pulsation frequency and pulse shape for a series of bias voltages as a function of pump current. The authors attribute the occurrence of self-pulsations to a de-stabilisation of relaxation oscillations by the saturable absorber. Note the dependence of pulse frequency on bias conditions and the dramatic effect of the reverse bias voltage level on the pulse width for smaller device currents. The effect of noise in a self-pulsating system is to increase the likelihood of triggering a pulse, as studied in [14]. However, as the gain has less time to recover in this regime, the output intensity of the pulses is consequently lower.

SPs can also be major causes of instability in mode-locked lasers [15, 16]. This mode-locking instability is referred to as QSML (Q-switched mode-locking) as it generally involves large amplitude intensity modulation of the mode-locked pulse train. It is therefore of interest to understand the origins of SPs in order to optimise devices for applications but also to suppress their appearance leading to stable mode-locking performance.

While SPs can lead to energetic pulses and are easy to excite, the pulse duration is limited by the recovery dynamics of the cavity gain and losses. Typically this recovery time is of the order of nanoseconds [ns] or longer, which means that for ultrafast [sub-ps] applications, mode-locking of the device is necessary. The mechanism underlying ultrashort pulse formation and mode-locking in two section laser diodes can be explained as follows: Spontaneous emission leads to intensity fluctuations which circulate in the laser cavity. On entering the absorbing section of the laser, both large and small pulses are diminished, but because the smaller amplitude pulses saturate the losses less efficiently, they are more strongly absorbed by the cavity. Over each round trip, this process repeats itself and the larger pulses grow. Eventually, over many round trips, a single dominant pulse forms that is successively shortened and amplified by the combined action of the gain and absorbing media. Stable mode-locking corresponds to a balance between the competing actions of the gain and absorber sections, and in the time domain, an ultrafast pulse train is emitted by the laser. By the Fourier

transform relation, the optical spectrum in this state is formed by a coherent comb of cavity modes.

From the point of view of both fundamental science and applications, mode-locked laser sources have had enormous impact. In particular, they have revolutionised optical frequency metrology by enabling self-referenced optical frequency combs that span an octave in frequency. By stabilising the individual modes of a passively mode-locked laser to a microwave standard reference, frequency combs have enabled absolute measurement of optical frequencies [17], new tests of fundamental theories such as QED [18], and the measurement of physical constants with unprecedented accuracy [19]. The revolutionary impact of this technology was recognised with the awarding of the Nobel Prize in Physics to Theodor Hänsch and John Hall in 2005.

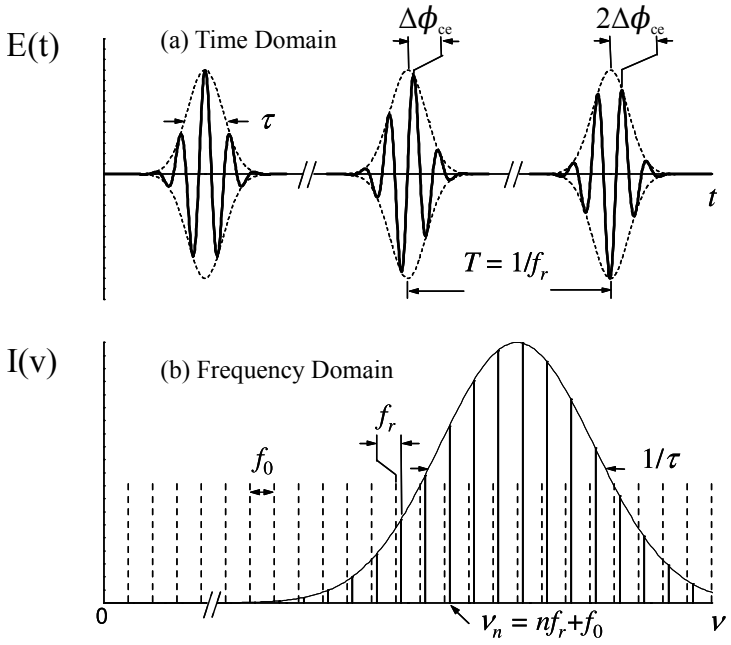

Figure 1.3: Schematic illustrating the time-frequency correspondence for mode-locked laser generating a pulse train with evolving carrier-envelope phase [17].

The broadband spectral coherence property of a mode-locked laser leads to the time-frequency correspondence shown in Fig. 1.3. The laser emits a regular series of pulses in time, with a well defined relative carrier envelope phase from pulse to pulse. The pulse train corresponds to a spectrum of equally spaced modes or comb "teeth" separated by the repetition rate. However, the comb frequencies are not necessarily integer multiples of the repetition rate as they may also have an offset frequency. The significance of octave spanning combs is that they enable self-referencing through detection of the f-2f beat frequency of the source. With active feedback stabilisation, the frequencies of the comb teeth can be locked to a microwave or optical reference frequency. This is the famous "phase-coherent link" between the microwave and optical domains achieved by the groups of Hall and Hänsch. Because the carrier envelope phase and the offset

frequency are connected through the fundamental Fourier transform relationship, comb stabilisation also enables coherent control of the electric field phase.

The current state of the art in short pulse generation by semiconductor lasers is represented by optically pumped vertical external cavity surface emitting lasers (also called semiconductor disk lasers). These devices have advantages including high power and the potential to generate very short pulses including a recent demonstration of 100 fs pulses at a wavelength of 1050 nm [20]. On the other hand, in-plane semiconductor lasers have the distinct advantages of compactness, low-cost, robustness and efficiency. Also, electrically pumped devices based on Indium Phosphide gain material are optimised for operation at the crucial telecommunications window near 1.5 μm. Thus in-plane semiconductor laser sources could lead to the widespread impact of emerging technologies based on mode-locked lasers and frequency combs, especially where low-cost and compactness of the source are critical.

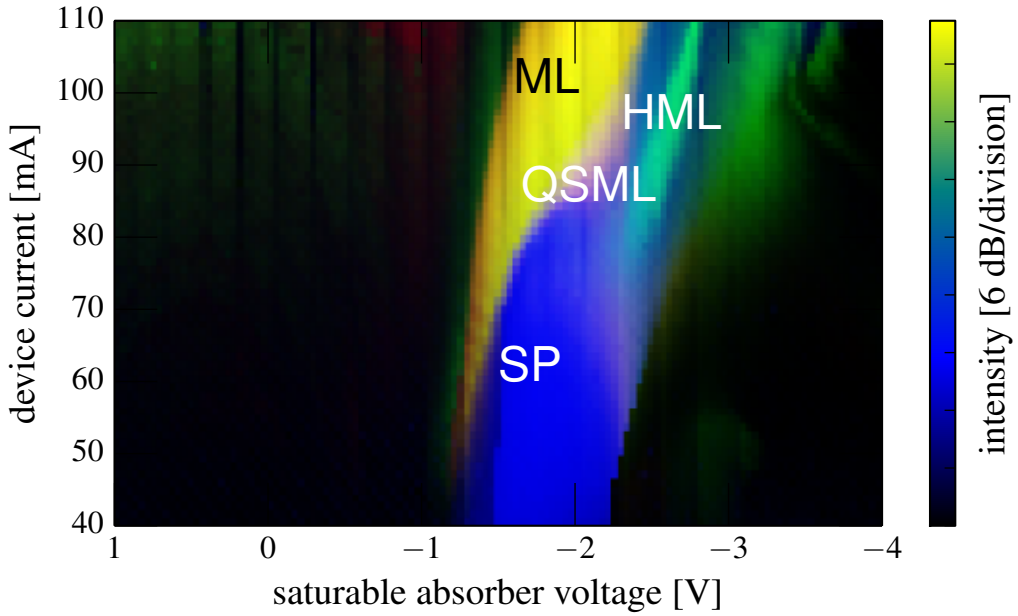

Figure 1.4: Measured phase space data of a two-section plain Fabry-Pérot laser. Labeled phase-space regions are SP (self-pulsation), ML (mode-locking), QSML (Q-switched mode-locking), and HML (harmonic mode-locking) [21].

The shortest pulses currently generated directly with in-plane devices are close to 300 fs in duration [22]. This is despite the fact that modern self-assembled gain materials provide sufficient gain bandwidth to reach much shorter pulses of order 100 fs. One reason for this is the presence of material dispersion, which makes it difficult to engage the available bandwidth without chirping of pulses. Pulsewidth is also limited due to group velocity dispersion (GVD), which tends to broaden pulses, unless compensated for with a sufficiently large frequency interval over which the dispersion is nearly linear [23]. Another limitation is the large circulating energy of very short pulses, which leads

to spatial and spectral hole burning and to carrier heating effects. Gain is replenished by intraband scattering and thermalisation on a 100 fs timescale, which suggests that carrier dynamics represent a fundamental obstacle to ultrashort pulse generation [24]. Though in this thesis we limited ourselves to the study of in-plane devices, [25] contains a useful review of the field of ultrafast pulse generation.

In order to illustrate the dynamical complexity of a simple two-section FP mode-locked laser, in Fig. 1.4 we have shown a measured phase-space map of the dynamical states as the device current and reverse bias voltage applied to the short section of the device are varied. This device has a length of 545 μm, with a saturable absorber section of length 30 μm The measured threshold current with a single current density over the whole device length was 12.5 mA. One can see that a large region of self-pulsations is found near threshold, and that these tend to evolve into mode-locked operation through a region of QSML. The current range where QSML is found becomes wider as the reverse bias is increased, and harmonic mode-locking (HML) is also found in a small region for large negative values of the absorber bias.

In Fig. 1.5 we have included optical spectra and the corresponding intensity autocorrelation measurements at two points in the phase space of Fig. 1.4. The autocorrelation in the left panel of Fig. 1.5 has a modulation envelope as a result of the QSML instability. The result from the right panel of Fig. 1.5 shows a flat profile, which indicates stable mode-locking. These two dramatically different states of the laser are separated by a change in the reverse bias applied to the short section of only 0.2 V. Despite this small change in the bias conditions, we find a large change in the optical spectral profile and a significant shift in the peak emission between these two spectra [21].

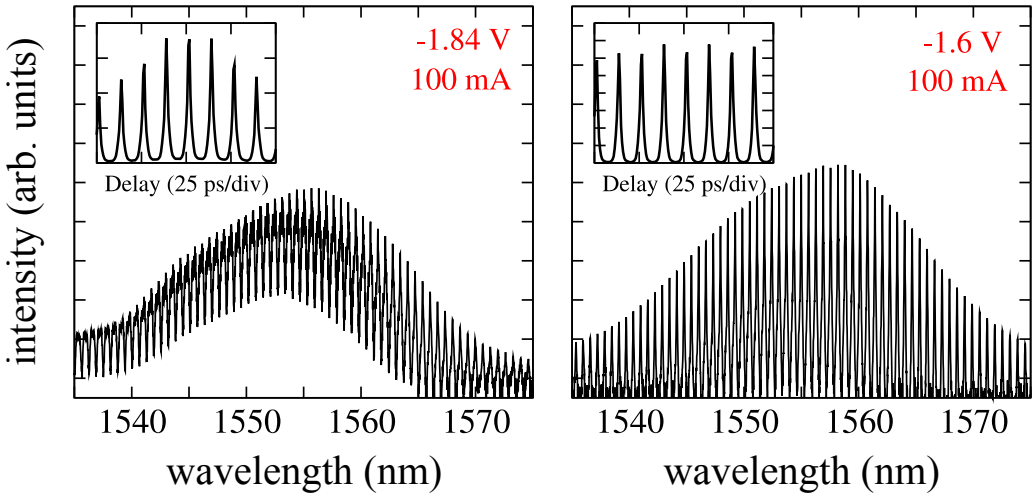

Figure 1.5: Optical spectra and intensity autocorrelation measurements from the device of Fig. 1.4 for a series of drive parameters as indicated [21].

1.1.1 Modelling of mode-locked semiconductor lasers

The classical results of mode-locking theory employed time domain lumped element models. The basic mechanism was explained by New, who showed that a short temporal window of net gain for pulses could open in a two-section laser provided the differential saturation of the gain and absorption were favourable [26]. New assumed small gain and loss per cavity round trip and neglected spectral filtering. Haus extended this model to take spectral filtering into account [27]. He first considered the limit of fast absorber recovery time in the sense that the pulse duration was long compared to the absorber recovery time. This limit is can be useful for understanding the dynamics of Kerr-lens mode-locking, where the nonlinearity is effectively instantaneous. Haus then extended his model to allow for physical absorber recovery times and was able to obtain a closed form expression for the pulse shape.

New's model and the later work of Haus showed how mode-locking could be obtained even when the pulse duration of 1 ps was much shorter than the absorber recovery time of c. 10 ps. This so-called slow-saturable absorber model with weak saturation gave good agreement with experimental results from dye lasers. While Haus did obtain the pulse shape explicitly, a weakness of his treatment however, was his assumption of weak saturation of the gain and absorption. In semiconductor lasers, the gain and losses per round trip are large and saturation is also strong. Thus the models of New and Haus are inadequate for describing the dynamics of mode-locking in certain solid-state lasers and they are inadequate for describing the dynamics in mode-locked semiconductor lasers in general.

Detailed spatio-temporal numerical models of mode-locked semiconductor lasers were developed which found that slow absorber dynamics were crucial for obtaining stable mode-locking in in-plane devices [24, 28]. They also showed that, in a semiconductor laser, the interplay between the gain and absorber dynamics determines the pulse width. In Haus' theory it is the interplay between saturable absorption and gain (both leading to pulse shortening) and dispersion (leading to pulse broadening) that determines the pulse width. The key message of both of these works is that although the gain bandwidth must ultimately determine the pulse duration, the action of the absorber is primarily responsible for pulse compression during propagation.

The delay-differential model developed by Vladimirov et al [29] provides an alternative to fully spatio-temporal simulations. This model allows for large gain and losses per round trip and also for strong gain saturation, and it contains the solutions of New and Haus as limiting cases. As it is still a lumped element method, it does not account for spatial hole burning and self-interference of the pulse at the cavity mirrors. The physical picture is therefore one of a unidirectional ring cavity. The attraction of this method is that one can obtain an understanding of the mode-locking dynamics at the level of phase-space bifurcation structure using numerical continuation tools. Thus

bifurcation lines leading to Q-switching or higher harmonic mode-locked solutions can be obtained.

1.1.2 Applications of mode-locked lasers in integrated optics

As we have indicated in Section 1.1, many applications of semiconductor lasers place stringent requirements on the laser source. For this reason, a number of interesting techniques have been developed to enhance the timing and phase-noise performance of semiconductor ML devices. Many applications of interest to our group can be addressed in an integrated optics setting, and for these applications, significant performance enhancements have been achieved using a variety of intracavity spectral filtering schemes.

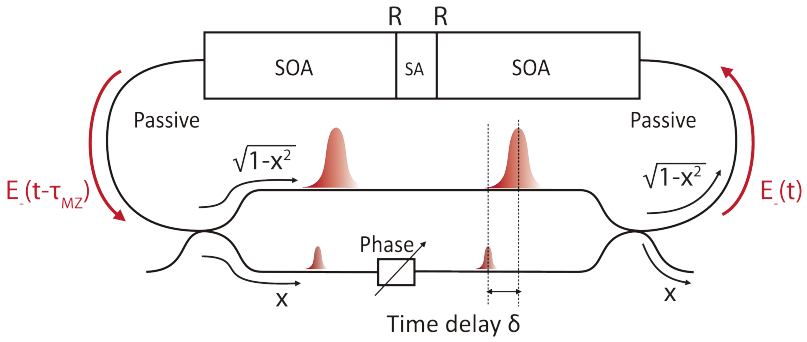

Figure 1.6: Diagram of mode-locked ring laser with an intracavity Mach-Zehnder interferometer for flattening of the gain spectrum. SOA - semiconductor optical amplifier, SA - saturable absorber [30].

As shown in Fig. 1.6, a Mach-Zehnder interferometer (MZI) can be used to smoothly impose a modulation correcting for material gain variation [30]. With a colliding pulse geometry this method of gain spectrum flattening theoretically allows for pulsed output with pulse-widths as short as 500 fs. The MZI acts to flatten the gain profile of the unfiltered device by suppressing the stronger modes toward the centre of the gain profile. This process is inherently lossy, and as a result the laser must be operated well above threshold. Tuning the path length difference between the two arms of the MZI also introduces a degree of variability of the pulse and spectral width. The phase of the MZI is optimised to provide the widest possible gain bandwidth, reaching up to 2 THz. Such large bandwidth makes these sources ideal for practical applications of comb-line emission spectra such as wavelength division multiplexing (WDM).

Stable microwave frequency oscillators, which can be based on optoelectronic detection of mode-locked pulse trains, represent another very useful application of ML devices. For these applications, modal frequency stability rather than optical bandwidth is of primary importance. To this end, harmonic mode-locking (HML) of extended cavity devices with integrated ring resonator filters have been shown to dramatically reduce

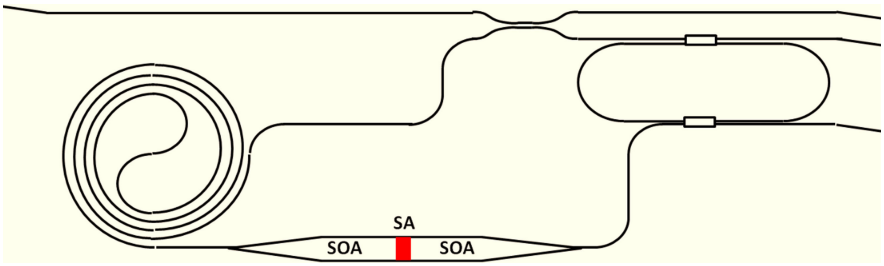

Figure 1.7: Schematic of mode-locked laser diode with an intra-cavity filter. Black lines indicate passive Si waveguides. SOA - semiconductor optical amplifier, SA - saturable absorber [31].

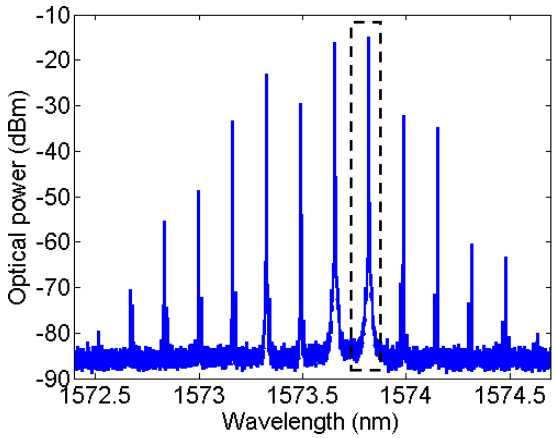

Figure 1.8: Optical spectrum of mode locked laser diode with a 20 GHz FSR intra-cavity filter. The SOA current is 220 mA and the saturable absorber is -0.5 V [31].

radio-frequency (RF) phase noise. A device demonstrated by a group at UCSB in the United States employs an intracavity 20 GHz ring resonator to filter output from a base cavity at 2 GHz. The RF linewidth of the filtered output is only 50 kHz, which is due to the quadratic dependence of the RF linewidth on the operating harmonic [31]. A schematic of the device is shown in Fig. 1.7, and the optical spectrum of the output from such a scheme is shown in Fig. 1.8. In the time domain this optical spectrum generates a sinusoidal output. Note the large optical signal-to-noise ratio (SNR) of greater than 60 dB that this device achieves. The device is also interesting from a modelling perspective, and in this case, with relatively narrow bandwidth, it seems reasonable that a frequency domain picture would be useful.

1.2 Discrete-mode semiconductor lasers

Our group has demonstrated an intracavity spectral filtering technique that enables the selection and locking of a discrete comb of lasing modes in a Fabry-Pérot (FP) semiconductor laser. These Discrete-Mode (DM) or indexed-patterned devices are designed using a Fourier transform technique that is based on a perturbative transfer matrix treatment of the lasing modes of a Fabry-Pérot resonator. In this case, a first

order scattering approximation allows one to directly link the index profile in real space to the threshold gain modulation in wavenumber space.

By applying this approach to the problem of passive mode-locking, our group has demonstrated mode-locked semiconductor lasers that generate both sinusoidal and pulsed intensity output [32, 33]. The cavity schematic and mode-locked spectrum of a fabricated device designed to support a comb of six modes is shown in Fig. 1.9. The device shown incorporates 48 slotted regions etched into the ridge waveguide of the laser and generates near-transform limited pulsed output with 2 ps duration. The repetition rate of 100 GHz is designed to be twice the fundamental [32].

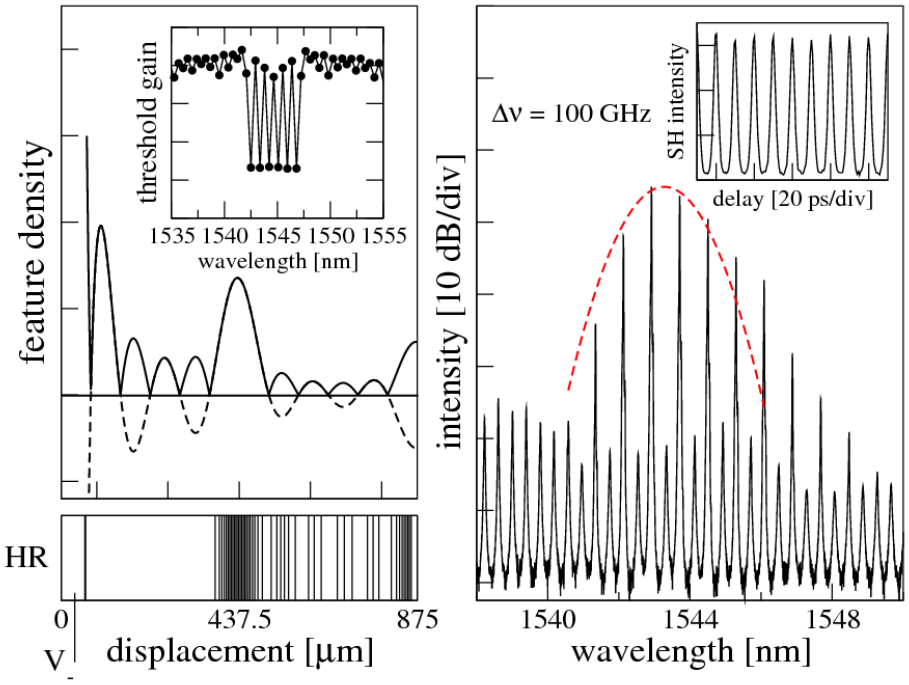

Figure 1.9: Left panel: Feature density function (solid line). Inset: Calculation of the threshold gain of the modes for the laser cavity. Lower panel: Laser cavity schematic. The device is high-reflection (HR) coated and includes a saturable absorber section as indicated. Right panel: Mode-locked spectrum of the device. The voltage across the saturable absorber section is -2.20 V while the current in the gain section is 120 mA. Inset: Autocorrelation measurement showing pulsed output at 100 GHz repetition rate [32].

To understand how the DM devices are designed, consider a one-dimensional model of the Fabry-Pérot cavity geometry as shown in Fig. 1.10. The system comprises a FP cavity of length L_c, the mirror reflectivities are r_1 and r_2 and N additional index steps are introduced. By treating the effect of these index-steps on the lasing mode structure of the cavity as a perturbation, a set of self-consistent equations for the lasing mode frequencies and their thresholds can be derived.

Suppose the transfer matrix T relates the right and left moving electric fields at the

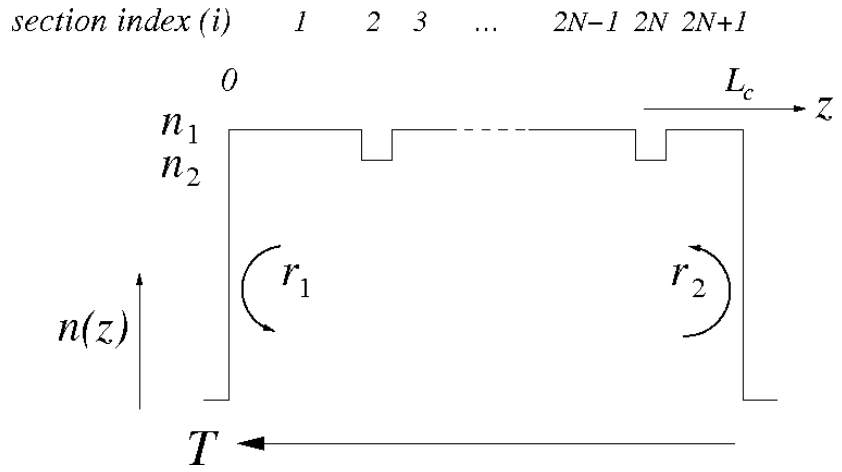

Figure 1.10: One dimensional model of a Fabry-Pérot laser cavity of length L_c. The cavity includes N index steps and has effective index n_1, while the additional features providing the index step have effective index n_2. All cavity sections are numbered $1 \leq i \leq 2N+1$ beginning on the left. The matrix T relates the left and right moving fields inside the cavity at the cavity mirrors. The mirror reflectivities are r_1 and r_2 as shown.

cavity mirrors. Then the lasing modes of the cavity are defined by the relation

$$T_{11} - T_{22} r_1 r_2 = T_{21} r_1 - T_{12} r_2. \tag{1.1}$$

At first order in the index step this equation can be written as

$$\begin{aligned} 1 - r_1 r_2 \exp(2i\Sigma\theta_i) = \\ i\tfrac{\Delta n}{n} \textstyle\sum_j \sin\theta_{2j} \left[r_1 \exp(2i\phi_j^-) + r_2 \exp(2i\phi_j^+) \right], \end{aligned} \tag{1.2}$$

where the quantities ϕ_j^- and ϕ_j^+ are the optical path lengths from the centre of each additional feature to the left and right mirrors respectively, $\sum_{i=1}^{2N+1} \theta_i$ is the adjusted complex optical path length across the cavity, $\theta_i = n_i k_0 L_i$, and $\Delta n = n_2 - n_1$. Note that this equation describes the coupling between each feature and the external mirrors exactly, but neglects any coupling between the features themselves.

If we neglect a factor describing the background losses associated with each mode, for a vanishing index step, the threshold gain for lasing is determined by the mirror losses: $\gamma_m^{(0)} = L_c^{-1} \ln 1/r_1 r_2$. In the perturbed case, self-consistent equations for the lasing modes are found by making an expansion in Eqn. 1.2 about the cavity resonance condition: $\sum \theta_i' = \phi_j^{-'} + \phi_j^{+'} = m\pi + \delta_m$, where δ_m determines the shift in the lasing mode frequency due to the effect of the additional features.

The inverse problem at first order is solved by choosing a particular cavity resonance, m_0, as an origin in wavenumber space. One finds that the effect of the spatially varying refractive index is maximised where each feature is placed such that a half wavelength subcavity at the wavelength of mode m_0 is formed between the feature and one of the external mirrors. The threshold gain can then be expressed at each resonance, m, where

$m = m_0 + \Delta m$, as $\gamma_m = \gamma_m^{(0)} + (\Delta n/n)\gamma_m^{(1)}$, where

$$\gamma_m^{(1)} = \frac{1}{L_c\sqrt{r_1 r_2}} \cos(m_0\pi)\cos(\Delta m\pi) \times \sum_{j=1}^{N} A(\epsilon_j)\sin(2\pi\epsilon_j m_0)\cos(2\pi\epsilon_j \Delta m). \quad (1.3)$$

In the above expression, the factor $A(\epsilon_j) = r_1 \exp(\epsilon_j L_c \gamma_m^{(0)}) - r_2 \exp(-\epsilon_j L_c \gamma_m^{(0)})$ and ϵ_j is the fractional position of the centre of each feature measured from the centre of the cavity.

The change in threshold gain is now expressed with respect to Δm and Fourier analysis can be used in order to build up a particular threshold gain modulation in wavenumber space. The positions of the index step features are adjusted so that half-wave and quarter-wave subcavities are formed with the external mirrors to the left and right as appropriate. Corrections for the finite index step associated with each feature are also accounted for [34].

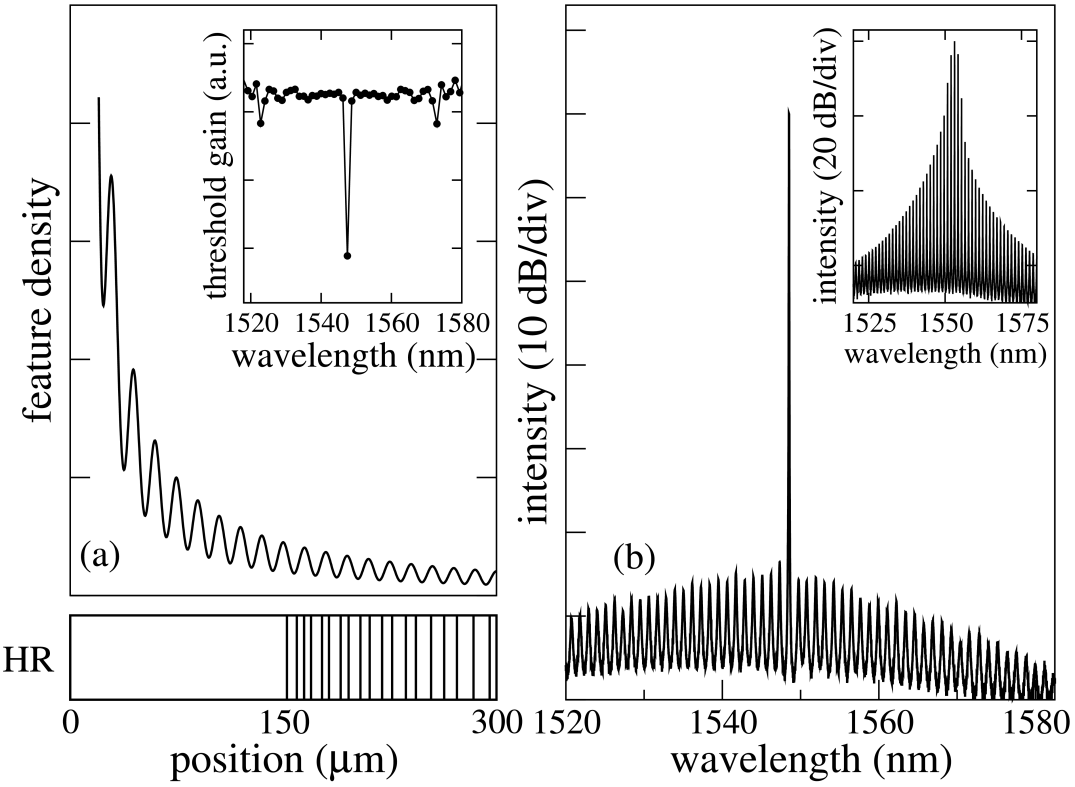

Figure 1.11: (a) Feature density function. Inset: calculated threshold gain of modes. Lower panel: laser cavity schematic indicating the locations of the reflective features. (b) Laser spectrum of the device, which is pumped at twice the threshold. Inset: spectrum at twice the threshold of an equivalent FP laser [35].

In order to select a single mode at the origin chosen in wavenumber space, the threshold modulation we require is simply $\gamma_m^{(1)} = \mathrm{sinc}(\Delta m)$. This function naturally selects a single FP mode at the origin and leaves all others unperturbed. The sinc function can

be written as the Fourier transform of the unit rectangle $\Pi(\epsilon)$. That is,

$$\text{sinc}(\Delta m) = \int_{\epsilon=-1/2}^{\epsilon=1/2} \cos(2\pi\epsilon\Delta m) d\epsilon. \tag{1.4}$$

Assuming that the mirror reflectivities are equal, the function $[A(\epsilon)]^{-1}$ diverges and changes sign at the device centre. Therefore, when adjusting feature positions for resonance a $\pi/2$ phase shift or equivalently a half-wave subcavity is found at the device centre. To avoid the problem of the central density divergence, an asymmetric cavity with one high-reflection (HR) mirror is advantageous.

The experimental laser spectrum of a single-mode device at twice threshold is shown in Figure 1.11 (b). This experiment device, as well as all others presented in this thesis, unless otherwise specified, were prepared by Eblana Photonics. The HR mirror allows features to be placed on the side opposite the HR mirror where the feature density is more uniform. We observe a single lasing peak at 1547.8 nm, which differs from the designed wavelength by much less than the fundamental Fabry-Pérot mode spacing. The side-mode suppression ratio measured at twice the threshold is greater than 50 dB. For comparison, a Fabry-Pérot laser fabricated without the etched features shows the expected multimode spectrum presented in the inset of Figure 1.11 (b).

Although these devices are FP lasers and are therefore difficult to integrate, the design approach developed by our group can be adapted to the case of open resonator geometries and an integrated optics platform. This integration potential is significant for applications, and the measured characteristics of the ML DM devices raise a number of critical questions that we must address if we are to realise this potential. For example, the pulses generated by the device of Fig. 1.9 have excellent pulse-to-pulse timing jitter as low as 20 fs, which is a considerable improvement on the performance of an otherwise identical mode-locked Fabry-Pérot laser [36]. This could be a fundamental aspect where the spectral filtering that we perform acts to limit dispersion coupled timing fluctuations, so-called Gordon-Haus timing jitter. Although the grating in the example of Fig. 1.9 is designed to support six modes with a bandwidth of 500 GHz, the optical spectrum has a bandwidth of c. 250 GHz. This is despite the fact that more than six modes are locked on account of power transfer by four-wave mixing. The reduced bandwidth we observe could reflect the fact that our design approach acts to predetermine the carrier wave frequency. We must therefore establish where the spectral filter should be placed with respect to the material gain and loss dispersion in order to optimise the performance of the device. These and other fundamental questions can only be answered by detailed modelling of the device dynamics.

In addition, published results suggest that we can expect further significant performance improvements with integrated devices. If we consider the HML device of Section 1.1.1, we can identify a number of similarities with the DM device of Fig. 1.9, which point to the possibility of our obtaining improved performance. For example, the

HML device operates at the tenth harmonic of the underlying 2 GHz cavity, which is the origin of the very narrow RF linewidth. The DM device shown had an RF linewidth of 2.5 MHz, but if we imagine operating the device at the tenth harmonic of an underlying cavity using a grating filter, we would expect a 25 times reduction in the RF linewidth to c. 100 kHz. Thus, although the FP and integrated waveguide cavities are very different at first sight, there are universal physical relationships that fundamentally govern the performance of these passively mode-locked devices.

Finally, we mention also that our approach could have advantages related to the spectral response of the filter. An intracavity ring-resonator filter has a periodic spectral response, which means that the precise number of locked modes is determined by the gain bandwidth, rather than by the filter directly. By contrast, our grating filter design approach allows us to precisely specify the distribution of primary lasing modes in a device.

The DM devices developed by our group represent testbeds for modelling dynamics of semiconductor lasers. In recent work, our group has had significant success in frequency domain modelling of complex multimode dynamics in both free-running and optically injected dual-mode devices [33, 37, 38]. Our group's current interest is in developing models of the mode-locked system that can reproduce the phase space structure and noise characteristics that are observed in laboratory experiments. Because these models must reflect the predefined structure of the laser optical spectrum, a frequency domain picture of individual lasing modes may be appropriate in these cases also. By careful calibration and comparison with experiment, we can understand how spectral stability and timing noise are simultaneously optimised. This will involve optimising the bias conditions but also the wavelength location of the spectral filter itself.

In this thesis we will describe a series of experimental measurements from two-section FP and DM devices. Although our interests from an applied perspective are primarily in ML devices, here we will restrict our attention to dynamical phenomena that are directly related to SPs. A thorough understanding of the origins of SPs is necessary in order to optimise ML lasers, particularly for devices with engineered spectra, such as those developed in our group. Here, the role of gain and absorption dispersion is of key importance, and SPs provide an ideal test bed for the suitability and appropriateness of any proposed models.

We also propose a foundation for a frequency domain ML model to compliment DDE and spatio-temporal approaches. This may allow for insights into factors that limit the RF and optical phase noise spectra, which are complicated as a consequence of multimode interactions. Despite only looking at SPs we will show that our experiments raise a large number of interesting questions requiring both understanding of current SP models in some detail, but also extension of these models to describe novel physical

phenomena present in the case of dual-mode devices. Using this approach we can also extend previous treatments of the problem to the multimode case with precise numbers of primary lasing modes. This allows for the potential to revisit bifurcation structure and seek new examples beyond the single mode approximation. Thus the work presented here provides a foundation for future applied research while also revealing new physics of interest to the broader nonlinear dynamics community.

1.3 Structure of this thesis

In our introduction to this thesis we have attempted to highlight the novelty of our laser design approach and the promising performance characteristics of passively mode-locked DM devices. In the remaining chapters we will present experimental measurements and modelling results for two section semiconductor lasers. We have structured the document so that our results are presented in three chapters.

The first set of results will be presented in Chapter 2, where we will map the phase-space structure of SP dynamics in a two-section Fabry-Pérot laser as a function of injected current and reverse bias applied to the saturable absorber section. We then introduce the well-known saturable absorber rate equation model of the dynamics and we derive the model parameters using a semi-analytic approximation for the gain and absorption in the laser. Experimental measurements of the Fabry-Pérot laser are compared with the results of numerical simulations based on the rate equation model and also on a delay-differential model of the laser.

In Chapters 3 and 4, we turn our attention to the dynamics of dual-mode two-section DM devices. In Chapter 3, we present our first example of coupled SP dynamics. We show how to extend the LSA model to the multimode case and show that our experimental results can be interpreted in terms of synchronisation of self-pulsations of the individual modes of the laser. We calculate the bifurcation structure that governs the appearance of these dynamics, and present evidence that suggests that we may have observed an example of chaotic SPs in the dual-mode system.

In Chapter 4, we present a second example of complex dual-mode SP dynamics. In this example, we present measurements of novel time-reversed waveforms of the individual coupled modes. We show that these dynamics can be reproduced with high accuracy by the multimode LSA model, and we quantify the role of material dispersion in organising the bifurcation structure. To complete this chapter we revisit the dynamics of Chapter 3, and show how the two examples of complex dynamics can be understood in a unified picture where material dispersion imposed by the spectral filter determines the characteristic dynamics that we observe in a given device. In the final chapter the main results of this thesis are summarised, and possible directions for future research along with an outlook are presented.

Chapter 2

Self-pulsations in Fabry-Pérot diode lasers with saturable absorption

2.1 Introduction

In this chapter we present experimental measurements of self-pulsations (SPs) in a two-section Fabry-Pérot (FP) semiconductor laser. Our goal is to establish typical parameter ranges and assess the level of agreement with experiment that we can expect of the LSA model. This will form the basis of our dual-mode simulations presented in the following two chapters of this thesis.

In recent work our group has demonstrated a number of ML devices with engineered spectra defined by an intracavity spectral filter [32, 33, 36]. These devices mode-lock with a bandwidth and optical spectrum determined by the design of the spectral filter. In our measurements of the mode-locking phase-space defined by the device current and reverse bias parameters, we have also found examples of SP and QSML. In order to optimise the design of ML lasers with engineered spectra, we must therefore understand the origin of these instabilities. We are interested in the dispersion of the gain and saturable absorption with wavelength in passively mode-locked DM devices. In particular, we would like to understand the effects of material dispersion on the dynamics and stability of mode-locked states of these devices. In order to do this, we must first calibrate current modelling approaches with real experimental parameters.

We will calibrate our models using an analytic function that provides a qualitative description of the susceptibility of a quantum-well active region [39]. In order to obtain parameter values for our device we fit analytic curves to the measured modal gain as a function of device current and we fit the measured absorption as a function of reverse bias. We test the accuracy of the LSA model description of observed self-pulsation dynamics in the device using experimentally calibrated model parameters on the basis

of a simplified picture of the FP laser, with a single dynamical variable representing the total field intensity.

As we will discuss, the LSA model does not provide a physically appropriate description of the large gains and losses that are typically found in semiconductor lasers. For this reason, we will see that the LSA model can only provide us with a qualitative picture of the measured SP dynamics. We therefore also make a comparison with a more physically appropriate delay-differential equation (DDE) model of the two-section laser [29]. We find that the DDE model can provide an accurate description of the observed SP dynamics, and we use this model to estimate the value of the carrier lifetime in the absorber section of the device.

Although the comparison reveals the approximate nature of the LSA, we will show in the following two chapters that a multimode extension of the model established here can provide a qualitative description of complex dynamics of coupled modes in dual-mode devices. The LSA model can be used to describe and explain the physical origin of multimode instabilities in two-section devices. As a result, this work can provide a basis to approximately describe a mode-locked laser in a frequency domain picture of individual modes based on the LSA with calibrated parameters.

This chapter is organised as follows: We first describe a typical example of a region of self-pulsations using optical and power spectral data. We then map the structure of the phase-space where self-pulsations are found as a function of injected current and reverse bias applied to the short section of the laser. We also present measured time-traces of self-pulsations under various drive conditions. We then describe our approach for calibrating the parameters of the device. From these fits we derive the differential gain and absorption near threshold for the device. Next we introduce the LSA rate-equation model of the two-section laser. In order to provide a comparison with the LSA model, we repeat our numerical modeling based on a system of delay-differential equations. We compare the numerical results of both models with equivalent parameters, and we use the results of our modelling work with the DDE model to estimate the carrier lifetime in the absorber section of the device.

2.2 Experimental measurements of self-pulsations in a two-section semiconductor laser

The device we consider is a multi-quantum well Indium Phosphide based ridge-waveguide Fabry-Pérot laser with one high-reflection (HR) coated mirror. The total device length is 545 μm with a saturable absorber section of length 30 μm adjacent to the HR mirror. Although this device length is the same as for the device presented in our introductory chapter, the material composition is different, which leads to a

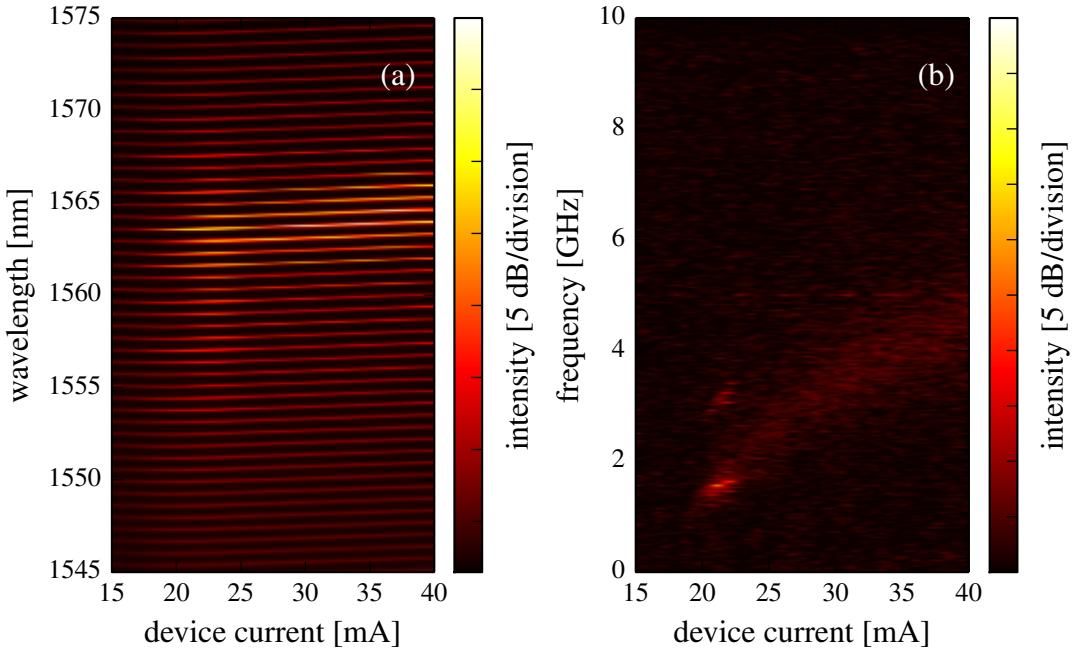

Figure 2.1: (a) Experimentally measured optical spectrum of the two-section FP device for a range of device currents. (b) Power spectrum of the total intensity output for a range of device currents. In both cases a bias of -0.4 V is applied across the absorbing section, with the temperature stabilised at 20.5°C

different phase-space structure. The active material has a peak gain near 1550 nm, and the device was mounted on a copper block with the temperature stabilised at 20.5°C. With both of the device contacts operating in forward bias we find a threshold current of 13.5 mA. We use this value to define a scale for the normalised device current density, j_s, and the corresponding current density is defined to be equal to 1 in normalised units. This will allow to us to compare threshold currents across equivalent devices with absorbing sections operated under different bias conditions.

The optical spectrum shown in Fig. 2.1 (a), was obtained by keeping a constant bias of -0.4 V on the back contact (absorber section) and sweeping the device current from 15 to 40 mA. The optical spectrum here was detected using a a fast photodiode (Thorlabs with 100 ps rise time), and the waveform was acquired using an Agilent Infiniium oscilloscope (70 ps). These devices were used for all subsequent measurements presented in the thesis, unless otherwise specified. We see the device reaches threshold shortly before 20 mA, beginning to lase at a wavelength around 1562 nm and moving to longer wavelengths as the pump current is further increased. We also see some spectral broadening here, particularly around 21 mA. The corresponding power spectrum is shown in Fig. 2.1 (b). Here we can discern a spectral peak near the relaxation oscillation frequency in a region centred around 21 mA. This peak indicates the presence of a sinusoidal intensity modulation associated with the undamping of the device relaxation oscillation.

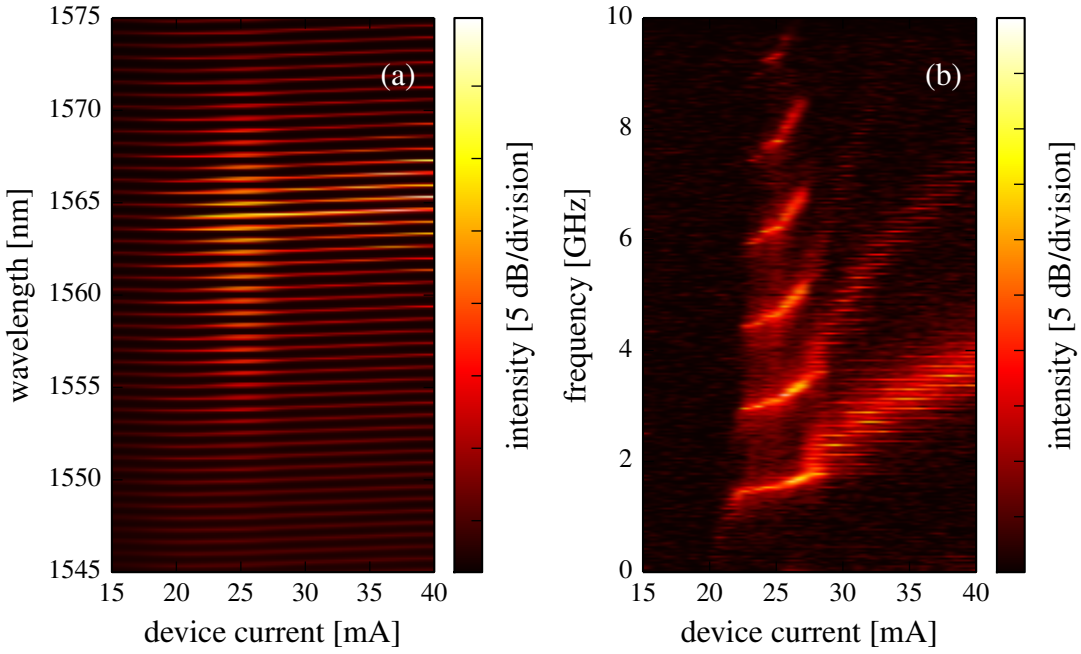

Figure 2.2: (a) Experimentally measured optical spectrum of the device for a range of device currents. (b) Power spectrum of the total intensity output for a range of device currents. In this instance a bias of -0.6 V is applied across the absorbing section in both cases, with the temperature stabilised at 20.5°C

Examples of optical and power spectral data at a fixed reverse bias voltage of -0.6 V are shown in Fig. 2.2. The optical spectrum in the left hand panel shows that the device reaches threshold at approximately 19 mA, with peak emission near 1564 nm wavelength. One can also see that the spectral bandwidth is relatively narrow near threshold, and that this bandwidth broadens considerably as the bias current in the long section of the device is increased. Examining the corresponding power spectral data in Fig. 2.2 (b), we can see that the intensity output of the device is constant in time at threshold, and that sinusoidal self-pulsations with a frequency of about 1.5 GHz appear above a bias current of 21 mA. As the pump current is increased the oscillations evolve from sinusoidal to large amplitude pulsations with many harmonic components. The fundamental frequency of these pulsations increases only slightly across the region of dynamics. After the SP region, the sharp SP frequency is replaced by a broad peak whose centre frequency increases more rapidly with drive current than the fundamental frequency in the SP region.

A plot of the measured threshold current, regions of constant output, and regions of SP dynamics are shown as a function of reverse bias in Fig. 2.3. One can see that the SP region is already open at zero reverse bias, but with very small extent. Note also that for small reverse bias voltages, the SP region is located some distance from threshold, and that a region of constant output separates the SP region from the device threshold for all reverse bias values. In the upper inset of Fig. 2.3 we have plotted the measured

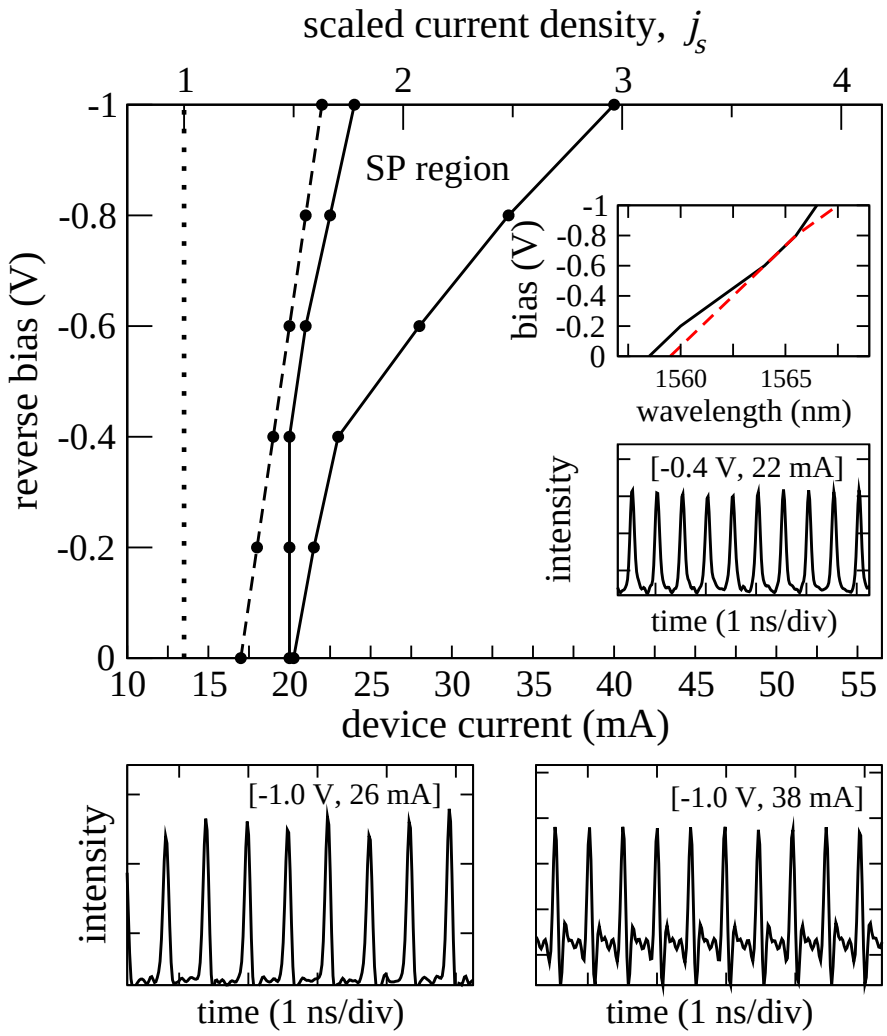

Figure 2.3: Upper panel: Threshold current (dashed line) and boundaries of the self-pulsation region (solid lines) as a function of the reverse bias applied to the absorber section of the device. The dotted vertical line is the threshold current of the device with both sections forward biased. The upper inset shows the measured variation of the wavelength of the lasing mode at threshold (solid line) and the position of the peak gain at threshold derived from numerical fits of the gain and absorption (dashed line). The lower inset shows a time-trace of self-pulsations measured at a reverse bias of -0.4 V and a current in the long section of 22 mA. The lower left and right figures show time-traces of self-pulsations measured at a reverse bias of -1.0 V and currents in the long section of 26 mA and 38 mA respectively.

value for the peak lasing wavelength at threshold together with the location of the peak gain derived from our numerical calibration of the gain and absorption functions. Note the dramatic shift we observe as the reverse bias is increased, with the peak intensity at threshold experiencing a red-shift of over 10 nm. In the lower inset we have also included a representative time trace of the SP dynamics found near the onset of SPs at a reverse bias voltage of -0.4 V. These are large amplitude pulsations with a pulse interval of 0.5 ns and a duration of approximately 200 ps.

Further measurements taken at -1.0 V are shown in the lower panels of Fig. 2.3. These measurements indicate that, near the onset of SPs, the pulse interval and duration are not strongly dependent on the drive parameters. In addition, only limited pulse shortening is apparent with increasing reverse bias. We also find that, at larger reverse bias values, the pulse shape becomes more complex with increasing drive current, with a shorter pulse peak developing together with a non-uniform pedestal.

2.3 Modelling of the device response

Our objectives in this section are to determine the device parameters and test calibrated numerical models by comparison with experimental measurements of self-pulsations. We will first consider a rate equation model that treats the dynamics of the field on time scales that are long compared to the round trip time in the cavity. Although this model cannot therefore describe mode-locked states of the device, it has provided valuable insights into the origins of SPs and the factors that lead to the appearance of bistability in devices with saturable absorbers [8, 40, 41].

In order to derive the rate equations we begin with the Maxwell-Bloch equations that describe the dynamics of electric field, the polarisation and the population inversion [42]. The equations are written:

$$\begin{aligned} i(\partial_t + \gamma_m^E)\beta_m(t) - \omega_m\beta_m(t) &= L^{-1}\int dz g_m^*(z)P(z,t) \\ i(\partial_t + \gamma_\perp)P(z,t) - \omega_a P(z,t) &= -N(z,t)\sum_m g_m(z)\beta_m(t) \\ i(\partial_t + \gamma_\parallel)N(z,t) &= iJ + 2\sum_m [g_m(z)\beta_m(t)P^*(z,t) - \text{c.c.}]. \end{aligned} \tag{2.1}$$

Here $m = 1, 2, ..., M$, with M equal to the total number of modes. The electric field associated with mode m, $\beta_m(t) = E_m(t)\exp[i\eta_m(t)]$ has amplitude $E_m(t) \in \Re$ and phase $\eta_m(t) \in \Re$. The decay rate of the electric field is γ_m^E. The polarisation is

$$P(z,t) = \sum_m g_m(z)p_m(z,t)\exp[i\eta_m(t)], \tag{2.2}$$

with a decay rate $\gamma_\perp$. The carrier density N has a decay rate given by $\gamma_\parallel$. The coupling

constants, g_m, are determined by the spatial modes of the laser resonator, the ω_m are the cold cavity eigenfrequencies, and ω_a is the atomic transition frequency. J is the pump current density and L the length of the device cavity.

The convention established in [43] classifies lasers by the relationships between $\gamma_m^E, \gamma_\perp$ and $\gamma_\parallel$. In the simplest case, a class A laser, only the electric field equation is required to describe the device dynamics, as both the inversion and polarisation can be adiabatically eliminated. Here, $\gamma_m^E \ll \gamma_\perp, \gamma_\parallel$. For a class C laser, all three equations are required, as $\gamma_m^E, \gamma_\perp$ and $\gamma_\parallel$ are all of a similar magnitude. In the case of a class B laser, which we consider, $\gamma_\perp \gg \gamma_\parallel, \gamma_m^E$. As the polarisation evolves at a much faster rate than the field and inversion we can adiabatically eliminate the polarisation to give

$$p_m(z,t) \simeq \frac{N(z,t)E_m(t)}{(\omega_a - \dot{\eta}_m) + i\gamma_\perp} \tag{2.3}$$

Substituting for $P(z,t)$ and $E_m(t)$ in the field equation, we obtain

$$\begin{aligned}[i(\partial_t + \gamma_m^E) - \omega_m + \dot{\eta}_m]E_m(t) = &\sum_{m'} \frac{(\omega_a - \dot{\eta}_{m'}) - i\gamma_\perp}{(\omega_a - \dot{\eta}_{m'})^2 + \gamma_\perp^2} E_{m'}(t) \\ &\times \exp[i[\eta_{m'}(t) - \eta_m(t)]]L^{-1} \int dz g_{m'}(z) g_m^*(z) N(z,t)\end{aligned} \tag{2.4}$$

We define

$$\frac{(\omega_a - \dot{\eta}_{m'}) - i\gamma_\perp}{(\omega_a - \dot{\eta}_{m'})^2 + \gamma_\perp^2} \equiv \frac{1}{\gamma_\perp} \cdot \frac{\Delta_{m'} - i}{\Delta_{m'}^2 + 1} \tag{2.5}$$

and

$$g_m(z) \equiv g \cdot \varphi_m(z) \tag{2.6}$$

The carrier density equation then becomes

$$\begin{aligned}i(\partial_t + \gamma_\parallel)N(z,t) - iJ = \quad &2\sum_m \sum_{m'} \{E_m(t)E_{m'}(t)\exp[i[\eta_m(t) - \eta_{m'}(t)]] \\ &\times \quad \frac{|g|^2}{\gamma_\perp} \frac{\Delta_{m'} - i}{\Delta_{m'}^2 + 1} N(z,t)\varphi_m(z)\varphi_{m'}^*(z) - \text{c.c.}\Big\}\end{aligned} \tag{2.7}$$

Defining

$$g_m = \frac{|g|^2}{\gamma_\perp(\Delta_m^2 + 1)} \tag{2.8}$$

the field equation becomes

$$\begin{aligned}[i(\partial_t + \gamma_m^E) - \omega_m + \dot{\eta}_m]E_m(t) = &\sum_{m'} g_{m'}(\Delta_{m'} - i)E_{m'}(t) \\ &\times \quad \exp[i[\eta_{m'}(t) - \eta_m(t)]]L^{-1} \int dz N(z,t)\varphi_m(z)\varphi_{m'}^*(z)\end{aligned} \tag{2.9}$$

To derive the rate equations we neglect oscillating terms with $\eta_{m'}(t) - \eta_m(t) \neq 0$. We

define

$$\tilde{G}_m(t) = g_m L^{-1} \int dz N(z,t)\varphi_m(z)\varphi_m^*(z), \tag{2.10}$$

and define a new field variable

$$\tilde{E}_m(t) = E_m \exp[-i[\eta_m(t) - \Omega_m^{\text{thr}} t]], \tag{2.11}$$

which shifts our reference frequency to the threshold eigenfrequency Ω_m^{thr}. We define the spatial average of the carrier density as

$$N(t) = L^{-1} \int dz N(z,t) \tag{2.12}$$

and we introduce the phase-amplitude coupling through the α factor. This quantity is identified with the detuning parameter Δ_m. We also identify the carrier lifetime τ_s with the inversion decay rate $\gamma_\parallel$. Our set of $M+1$ rate equations then become

$$\begin{aligned} \dot{\tilde{E}}_m &= \frac{1}{2}(1+i\alpha)(\tilde{G}_m - \gamma_m)\tilde{E}_m \\ \dot{N} &= j - \frac{N}{\tau_s} - \sum_m \tilde{G}_m |\tilde{E}_m|^2. \end{aligned} \tag{2.13}$$

where γ_m is the cavity decay rate and j is now the current density. Note that by writing a single equation for the averaged carrier density, these equations implicitly assume that carrier diffusion washes out any fast varying spatial inhomogeneity such that the carrier density may be assumed uniform along the length of the cavity. This assumption is commonly referred to as the uniform-field limit [44, 45].

We now restrict our attention to a single lasing mode, which represents the total field in a Fabry-Pérot device. Rewriting equations (2.13) in terms of the field intensity, the equation for the phase decouples and we obtain:

$$\begin{aligned} \dot{S}(t) &= (\tilde{G}(N_g) - \gamma)S(t) \\ \dot{N}_g(t) &= j - \frac{N_g}{\tau_s} - \tilde{G}S(t). \end{aligned} \tag{2.14}$$

Here S is the photon density, $\tilde{G}(N_g)$ is the modal gain and N_g is the carrier density in the gain section. In a steady-state with finite intensity these equations require that $\tilde{G}(N_g) - \gamma = 0$. Since γ is a constant, we see that the carrier density N_g is clamped once the laser threshold is reached. We define the threshold value of the carrier density as N_g^0, and we linearise the gain around the threshold value to define $\tilde{G} = \tilde{G}_0 + \tilde{g}(N_g - N_g^0)$, where $\tilde{g}$ is the differential gain and $\tilde{G}_0$ is modal gain at threshold. Note that if we take a vanishing intensity at threshold, we find that $N_g^0 = j_0\tau_s$, where j_0 is the threshold current density.

The Jacobian matrix associated with equations (2.14) evaluated for the $S \neq 0$ steady-

state or equilibrium solution is given by

$$A = \begin{pmatrix} 0 & \tilde{g}S \\ -\gamma & -\frac{1}{\tau_s} - \tilde{g}S \end{pmatrix} \tag{2.15}$$

The characteristic equation of the system is obtained from the Jacobian using the relation $|A - \lambda I_d| = 0$. Here λ represents the complex eigenvalues of the system and I_d the identity matrix. The characteristic equation is given by:

$$\lambda^2 + (1/\tau_s + \tilde{g}S)\lambda + \gamma\tilde{g}S = 0. \tag{2.16}$$

The eigenvalues of the system obtained by solving (2.16) are:

$$\lambda_{1/2} = -(1/2)(1/\tau_s + \tilde{g}S) \pm (1/2)\sqrt{(1/\tau_s + \tilde{g}S)^2 - 4\tilde{g}\gamma S} \tag{2.17}$$

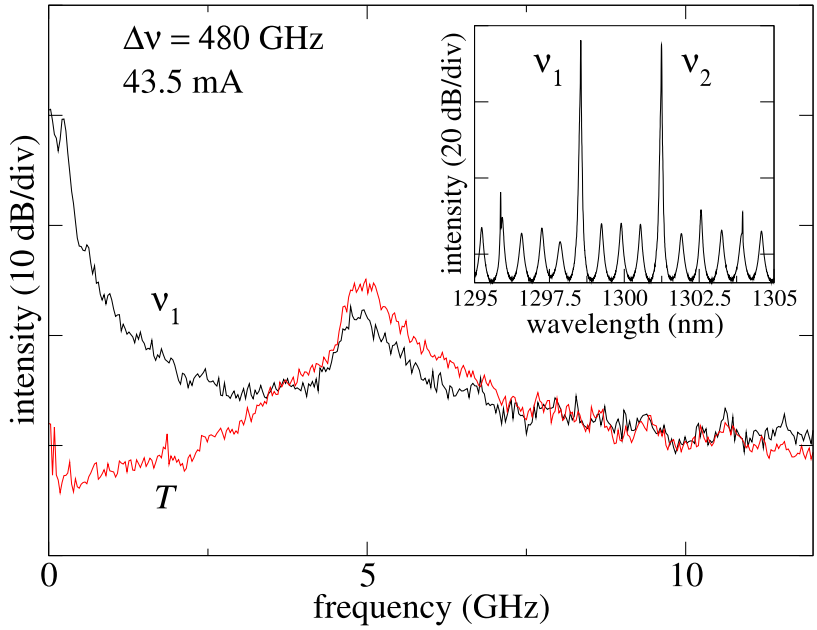

Figure 2.4: Power spectra of one of the primary modes and of the total intensity T, of a dual-mode device, measured at the two-colour point. Inset: Optical spectrum of the device at a device current of 43.5 mA (two-colour point). The lower amplitude of the Total output below 2.5 GHz is a result of anti-phase interaction of the constituent modes.

The cavity decay rate γ is typically three orders of magnitude larger than the carrier decay rate $1/\tau_s$. Since $(1/\tau_s + \tilde{g}S)^2 \ll 4\tilde{g}\gamma S$, we can neglect the $(1/\tau_s + \tilde{g}S)^2$ term. This approximation allows us to obtain the following expressions for the frequency (ω_{RO})

and the damping (σ_{RO}) of the relaxation oscillations:

$$\begin{aligned} \omega_{RO} &\approx \sqrt{\tilde{g}\frac{N_g^0}{\tau_s}(j_s-1)} \\ \sigma_{RO} &= -\frac{1}{2}\left(\frac{1}{\tau_s}+\frac{\tilde{g}N_g^0(j_s-1)}{\gamma\tau_s}\right) \end{aligned} \tag{2.18}$$

where $j_s = j/j_0$. To obtain an order of magnitude estimate of the relaxation oscillation frequency note that the lasing condition determines that $\gamma = \tilde{G}_0 \simeq \tilde{g}N_g^0$. In physical units, the cavity decay rate is in turn given by $(\alpha_{\text{mir}} + \alpha_{\text{int}})v_g$, where α_{mir} and α_{int} are the mirror and internal losses of the cavity respectively, and v_g is the group velocity. Typical values are $\alpha_{\text{mir}} + \alpha_{\text{int}} = 25$ cm^{-1}, $n_g = 3.4$, and $\tau_s = 1$ ns. At twice threshold ($j_s = 2$), the relaxation oscillation frequency is then equal to 2.4 GHz, which is in broad agreement with our estimate from the power spectral peak observed in our measurements.

Note that the damping of the relaxation oscillations has a linear dependence on the device pump current, while the frequency of the relaxation oscillations has a square-root dependence. This dependence is visible in Fig. 2.2 (b) where the peak associated with the relaxation oscillations evolves with a sub-linear dependence on the pump current from 30 to 40 mA. Figure 2.4 shows a measurement made by colleagues of the intensity power spectrum of a single-section dual-mode device. This device is similar to the two-section dual-mode devices which we will study in subsequent chapters. Data are presented for the power spectrum of the total intensity and for the intensity of one of the primary modes of the device. One can see the characteristic peak in the noise spectrum at the relaxation oscillation frequency around 5 GHz in this example. This measurement was made at the two-colour point, where the intensity of both modes is approximately equal. The corresponding optical spectrum of the device is shown in the inset of Fig. 2.4. The low frequency peak in ν_1 is not present in the total intensity T as it is associated with antiphase intensity dynamics, where the intensity of each of the individual modes varies but the total intensity remains constant.

In order to formulate a physical model for a Fabry-Pérot laser and ultimately for a device such as that shown in Fig. 2.4, we must determine a large number of parameters that describe the variation of the gain and saturable absorption of the device both as a function of carrier density and frequency. Even in the case where we are describing a Fabry-Pérot device using a total intensity variable, we must still allow for the frequency to enter as a variable due to the experimentally observed shift of the peak emission wavelength in Fig. 2.1 (a) and Fig. 2.2 (a). In addition, we must estimate the value of the carrier recovery time in each section of the laser. The physical structure of our governing equations is illustrated in Eqn (2.19). These equations extend the single-section model of Eqn (2.14) to describe a two-section device. Again the total field approximation is made to describe the intensity of the FP laser, and now the saturable absorber section of the laser is described as an unpumped region, with an unsaturated

loss determined by the applied voltage.

In physical units our rate equations for the two-section laser read

$$\begin{aligned} \dot{S} &= [(1-\rho)\tilde{G}(N_g) + \rho\tilde{A}(N_q) - \gamma]S \\ \dot{N}_g &= j - \frac{N_g}{\tau_s} - \tilde{G}(N_g)S \\ \dot{N}_q &= \quad -\frac{N_q}{\tau_q} - \tilde{A}(N_q)S \end{aligned} \tag{2.19}$$

Here S is again the photon density, $\tilde{G}$ is the modal gain and $\tilde{A}$ is the modal absorption. N_g and N_q are the carrier densities in the gain and absorber sections, respectively. The functional forms for the modal gain and absorption are

$$\tilde{G}(N_g) = \tilde{G}_0 + \tilde{g}_g(N_g - N_g^0), \tag{2.20}$$

and

$$\tilde{A}(N_q) = \tilde{g}_q N_q - \tilde{A}^0. \tag{2.21}$$

In the expression for $\tilde{G}(N_g)$, $\tilde{G}_0$, $\tilde{g}_g$, and N_g^0 are respectively the threshold gain assuming a transparent absorber section, and the corresponding differential gain and carrier density. In the expression for the modal absorption, $\tilde{A}(N_q)$, $\tilde{A}^0$, and $\tilde{g}_q$ are the unsaturated absorption and the differential absorption. The ratio of the absorber section length to the total device length is ρ, which defines $\tilde{G}_0 = (1-\rho)^{-1}\gamma$. The current density in the gain section is j, while the carrier lifetimes in the gain and absorber sections are respectively τ_s and τ_q.

In previous work colleagues have made extensive use of rate equation models to simulate the dynamics of dual-mode semiconductor lasers with optical injection and feedback [37, 46]. These models provide excellent agreement with experiment [47]. We now derive convenient normalised equations which allow comparison with these works. We rescale time in units of the cavity decay rate, γ, and we define the normalised pump current, $p = (j - j_0)/j_0 \equiv j_s - 1$. We also define the normalised carrier densities in each section of the device: $n_g = (N_g - N_g^0)/N_g^0$ and $n_q = (N_0 - N_q)/N_g^0$, where $N_0 = \tilde{A}^0/\tilde{g}_q$. In normalised units the equations then read

$$\begin{aligned} \dot{I} &= [(1-\rho)G(n_g) + \rho A(n_q) - 1]I \\ T\dot{n}_g &= p - n_g - G(n_g)I \\ T\dot{n}_q &= \Delta(q_0 - n_q) + A(n_q)I \end{aligned} \tag{2.22}$$

where $q_0 = \dfrac{N_0}{N_g^0}$, $T = \gamma\tau_s$, and $\Delta = \tau_s/\tau_q$. In these equations the normalised gain functions are

$$G(n_g) = (1-\rho)^{-1} + g_g N_g^0 n_g \tag{2.23}$$

where $g_g = \gamma^{-1}\tilde{g}_g$. The normalised modal absorption function is

$$A(n_q) = -g_q N_g^0 n_q \tag{2.24}$$

where $g_q = \gamma^{-1}\tilde{g}_q$. The normalised intensity is now $I = (\tau_s\gamma/N_g^0)S$, and for convenience we have defined the normalised absorption function so that the absorption is proportional to the carrier density in the absorber section.

2.4 Bifurcations of a single-mode semiconductor laser with a saturable absorber

A typical gain and absorption profile in a two-section semiconductor laser is shown schematically in Fig 2.5 (a). Here we have indicated the position of the peak gain, and the negative offset of the gain function at long wavelength gives an estimate of the internal or background losses, α_{int}. The threshold gain and absorption are defined at the wavelength of the peak gain as shown. We will extract physical parameters from experimentally measured gain and absorption profiles later in this chapter. However, for now we simply use the parameters shown in Table 2.1, which will allow us to discuss the experimentally relevant aspects of the system's behaviour. Although these parameters are representative in general they are not directly extracted from any of the presented experimental results.

Table 2.1: Parameters for bifurcation diagrams Figs. 2.5 - 2.11

N_g^0	$A^0\gamma^{-1}$	g_g	$g_q\rho^-1$
2.2	0.6	1.0	1.4

We now consider the bifurcation structure that determines the existence and physical origin of SP dynamics in the LSA system of Eqn (2.22). The non-zero steady state intensities of the system are given by the solution of the quadratic equation

$$aI^2 + b(p)I + c(p) = 0 \tag{2.25}$$

where

$$\begin{aligned} a &= -\gamma g_g g_q N_g^0 \\ b(p) &= (1-\rho)g_g g_q N_g^0 p - \Delta(\rho g_g g_q q_0 N_g^0 + (1-\rho)g_g G(n_g^0)) \\ c(p) &= \Delta(1-\rho)g_g p - \Delta q_0 \rho g_q \end{aligned}$$

In general as p is varied we may find regions with no real roots, where the discriminant $(b^2 - 4ac)$ is negative. In this case we have a region of p with no physical (real valued) steady states. Varying p we will encounter a double root when $b^2 - 4ac = 0$, and thereafter, with a positive discriminant, the system will have two real roots. For

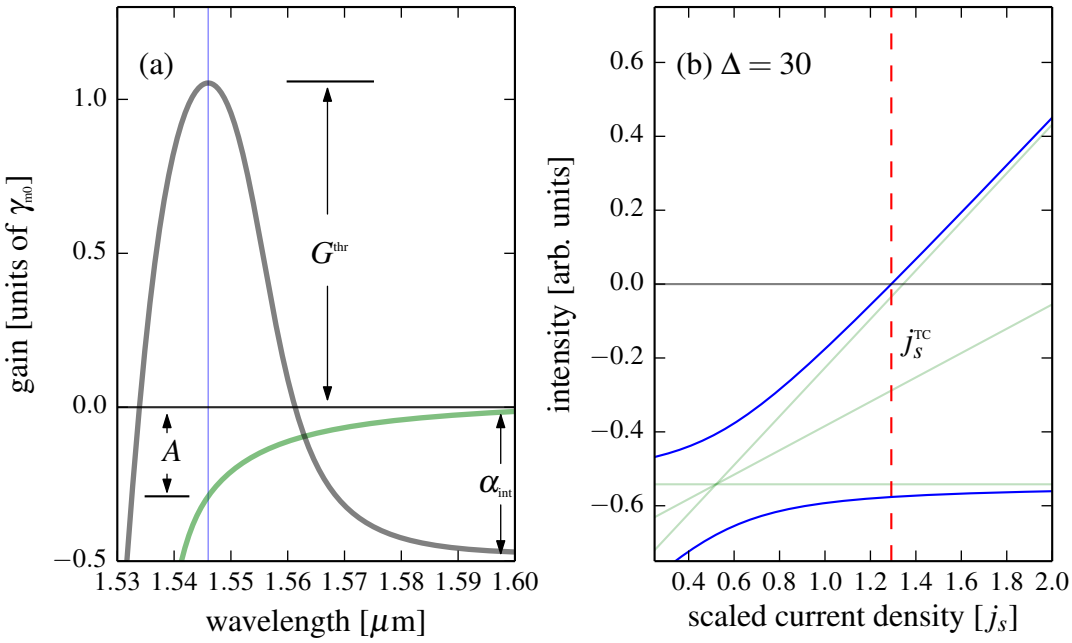

Figure 2.5: (a) Schematic diagram of the material gain and absorption in a typical semiconductor laser. The location of the peak gain is indicated. The model parameters describing the dispersion of the modal gain and absorption are also highlighted. (b) Branches of equilibrium solutions of the model with $\Delta = 30$ shown in blue, for the parameters given in Table 2.1. The vertical dashed red line is the lasing threshold, j_s^{TC}, where the zero field solution becomes unstable. The asymptotes and centre axis of the hyperbola (2.26) are also shown in light green.

positive p and I this gives us real values of the intensity which are allowed physical equilibrium states of the model. Mathematically, the occurrence of this double root corresponds to a saddle-node bifurcation. In one dimensional systems, a saddle-node bifurcation implies the creation of a stable and unstable equilibrium state in the system. However, as we are dealing here with a higher dimensional system this will not be true in general. Here we will instead use physical arguments together with knowledge of the effects of nearby Hopf and transcritical bifurcations to determine the stability of the steady-states.

The structure of the steady states of the system can be understood more clearly by recasting (2.25) as a hyperbola in the $p - I$ plane. The steady-state solutions form a hyperbola in the $p - I$ plane of the form

$$A_{xx}p^2 + A_{yy}I^2 + 2A_{xy}pI + 2B_xp + 2B_yI + C = 0 \tag{2.26}$$

provided the determinant condition

$$D = \begin{vmatrix} A_{xx} & A_{xy} \\ A_{xy} & A_{yy} \end{vmatrix} < 0. \tag{2.27}$$

is obeyed. Here

$$\begin{aligned} A_{xx} &= 0 \\ A_{yy} &= -\gamma g_g g_q N_g^0 \\ A_{xy} &= \frac{1}{2}(1-\rho) g_g g_q N_g^0 \\ B_x &= \frac{1}{2}\Delta(1-\rho) g_g \\ B_y &= -\frac{1}{2}\Delta(\rho g_g g_q q_0 N_g^0 + (1-\rho) g_g G(n_g^0) \\ C &= -\Delta \rho g_q q_0 \end{aligned} \tag{2.28}$$

which means that since $A_{xx} = 0$ the determinant condition is trivially satisfied.

The centre of the hyperbola is given by

$$(x_0, y_0) = -\frac{1}{D}\left(\begin{vmatrix} B_x & A_{xy} \\ B_y & A_{yy} \end{vmatrix}, \begin{vmatrix} A_{xx} & B_x \\ A_{xy} & B_y \end{vmatrix}\right), \tag{2.29}$$

with the centre axis given in this case by

$$-\frac{A_{xy}}{A_{yy}}(p - x_0) + y_0. \tag{2.30}$$

The asymptotes are given by

$$-\frac{2A_{xy}}{A_{yy}}(p - x_0) + y_0 \tag{2.31}$$

and

$$y_0. \tag{2.32}$$

The orientation of the hyperbola can be determined from the sign of the determinant

$$\begin{vmatrix} A_{xx} & A_{xy} & B_x \\ A_{xy} & A_{yy} & B_y \\ B_x & B_y & C \end{vmatrix} \tag{2.33}$$

which, in our case simplifies to the quantity

$$\Delta - s \tag{2.34}$$

where $s = g_q/g_g$.

If (2.34) is negative the hyperbola opens along the p-axis. In this case branches of steady-state solutions are born in a saddle-node bifurcation at p_{SN}, where $b^2 - 4ac = 0$

in Eqn (2.25). We find

$$p_{\text{SN}} = \frac{1}{(1-\rho)g_g N_g^0}\left(\frac{\Delta}{s}(q_0^* - \gamma) + 2\left[\frac{\Delta}{s}(1-\frac{\Delta}{s})q_0^*\gamma\right]^{1/2}\right) \tag{2.35}$$

where we have defined the fractional absorption due to the reverse biased section

$$q_0^* = \rho N_g^0 g_q q_0 = \gamma^{-1}\rho A^0.$$

We can determine the field intensity at the saddle-node bifurcation, I_{SN}, using (2.25):

$$I_{\text{SN}} = \frac{-b(p_{\text{SN}}) \pm \left(b(p_{\text{SN}})^2 - 4ac(p_{\text{SN}})\right)^{1/2}}{2a} \tag{2.36}$$

We will now consider the stability of the only other steady state in the system, which is the trivial zero field solution. This will help us to determine the threshold behaviour of the device, and to do this in a physically minded way we must consider interactions with other dynamical states of the system. The Jacobian of the full system is given by

$$J = \begin{pmatrix} \alpha_{11} & \alpha_{12} & \alpha_{13} \\ \alpha_{21} & \alpha_{22} & \alpha_{23} \\ \alpha_{31} & \alpha_{32} & \alpha_{33} \end{pmatrix}. \tag{2.37}$$

Here,

$$\begin{aligned}
\alpha_{11} &= \partial f_1/\partial I = (1-\rho)G(n_g) + \rho A(n_q) - \gamma \\
\alpha_{12} &= \partial f_1/\partial n_g = (1-\rho)g_g N_g^0 I \\
\alpha_{13} &= \partial f_1/\partial n_q = -\rho g_q N_g^0 I \\
\alpha_{21} &= \partial f_2/\partial I = -\frac{1}{T}(G(n_g^0) + g_g N_g^0 n_g) \\
\alpha_{22} &= \partial f_2/\partial n_g = -\frac{1}{T}(1 + g_g N_g^0 I) \\
\alpha_{23} &= \partial f_2/\partial n_q = 0 \\
\alpha_{31} &= \partial f_3/\partial I = -\frac{1}{T}(g_q N_g^0 n_q) \\
\alpha_{32} &= \partial f_3/\partial n_g = 0 \\
\alpha_{33} &= \partial f_3/\partial n_q = -\frac{1}{T}(\Delta + g_q N_g^0 I)
\end{aligned} \tag{2.38}$$

In the case of the zero field solution, the Jacobian is greatly simplified, with only α_{11} changing sign as we vary p. We find that the zero field solution is stable until a transcritical bifurcation of the system at

$$p_{\text{TC}} = \frac{\rho g_q q_0}{(1-\rho)g_g}. \tag{2.39}$$

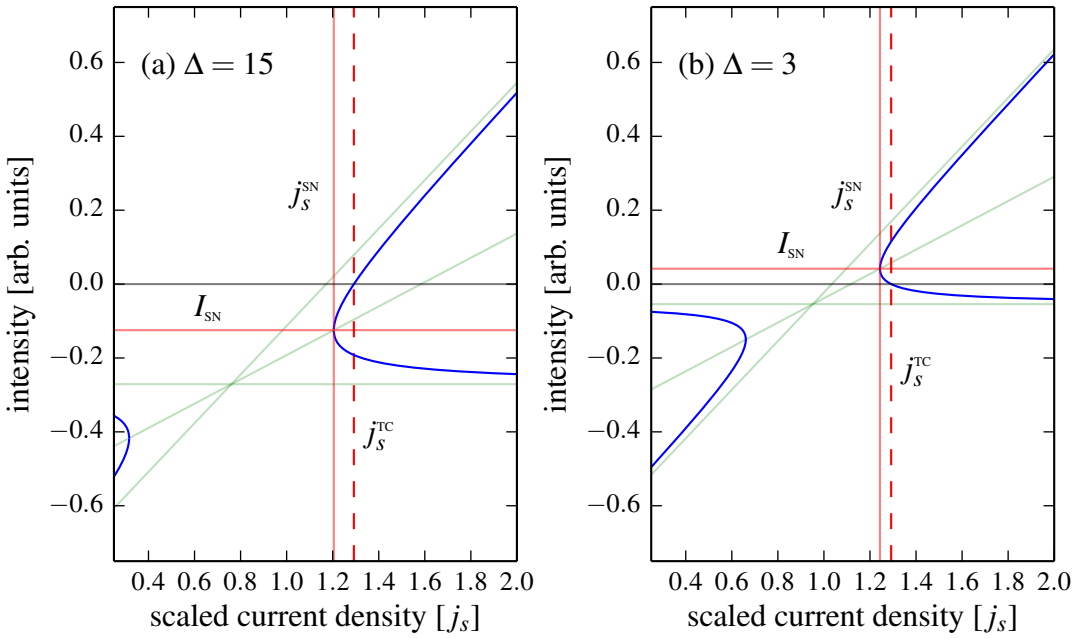

Figure 2.6: Branches of equilibrium solutions of the model (2.25) with (a) $\Delta = 15$ and (b) $\Delta = 3$, for the parameters given in Table 2.1 in blue. The vertical dashed red line is the lasing threshold, j_s^{TC}. The solid red vertical line is j_s^{SN}, the pump value of the physically relevant SN bifurcation. A solid red horizontal line at intensity I_{SN} is also shown in both cases. The asymptotes and centre axis of the hyperbola (2.26) are also shown in light green.

At this value of the pump parameter, the intensity along one steady-state solution branch becomes equal to zero and exchanges stability with the zero field solution. The precise nature of this stability exchange depends on the sign of I_{SN}. In all cases however, with increasing pump, the off state is stable before the transcritical bifurcation, and unstable afterwards. Fig. 2.5 (b) shows the intensity branches of steady state solutions with $\Delta = 30$. In order to generate this figure we took parameters from Table 2.1. Similarly we generate Fig. 2.6 (a) and (b) using the parameters from Table 2.1, for successively smaller values of Δ, equal to 15 and 3.

Though the value of p_{TC} itself is independent of Δ, the bifurcation structure and nature of the dynamics at threshold is strongly dependent on this quantity. In Fig. 2.5 (b), because $\Delta - s$ is positive, the hyperbola opens along the I-axis, meaning there is no saddle node bifurcation in this case. In both Fig. 2.6 (a) and (b) the hyperbola opens along the p-axis, with negative and positive values of I_{SN} respectively.

In both Fig. 2.5 (b) and Fig. 2.6 (a) the increasing branch of (2.25) undergoes a transcritical bifurcation as it crosses the zero axis to take on positive values. This branch of solutions then becomes stable, the system thereby entering a CW state at threshold.

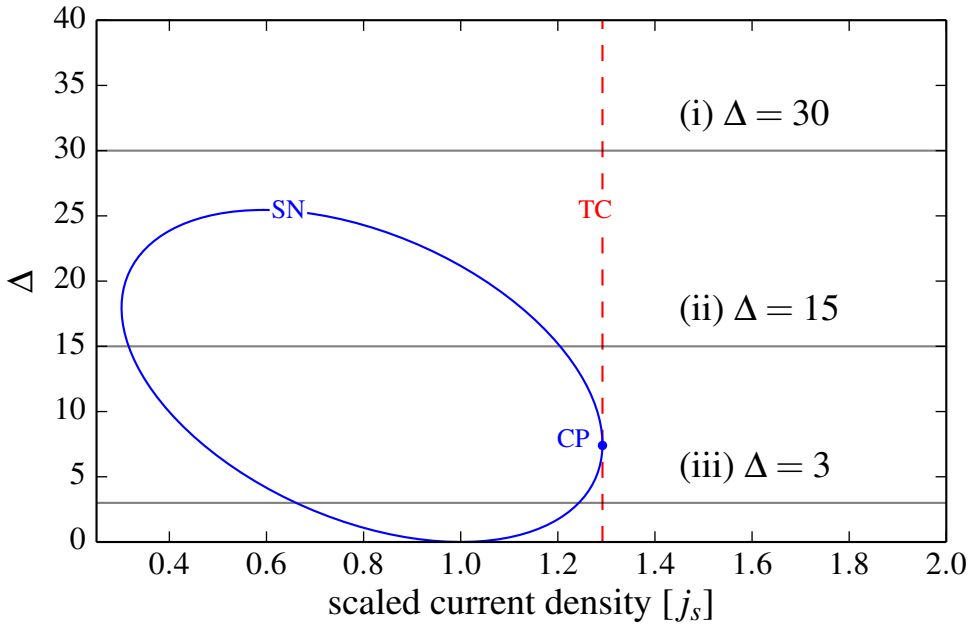

Figure 2.7: Geometry of the saddle node and transcritical bifurcations in the $\Delta - p$ plane. Here, (i) corresponds to Fig. 2.5 (b), where we can clearly see the absence of a saddle node. (ii) and (iii) correspond respectively to Fig. 2.6 (a) and (b), with values of Δ above and below $\Delta_{\text{SN-TC}}$.

The saddle-node and transcritical bifurcations coincide in a cusp bifurcation (CP) at

$$\Delta_{\text{SN-TC}} = s\frac{q_0^*}{1+q_0^*}. \tag{2.40}$$

This value is significant physically in the sense that for values of Δ larger than $\Delta_{\text{SN-TC}}$ we expect to see a CW state at threshold. This behaviour was observed in our experiment as shown in Fig. 2.1 and Fig. 2.2. The geometry of the saddle node and transcritical bifurcations are shown in the $p - \Delta$ plane in Fig. 2.7 (a). Here, (i) corresponds to Fig. 2.5 (b), where we can clearly see the absence of a saddle node bifurcation. (ii) and (iii) correspond to Fig. 2.6 (a) and (b), with values of Δ above and below $\Delta_{\text{SN-TC}}$ respectively.

If I_{SN} is positive we must account for the stability of two physically allowable branches of the steady state intensity. Since the branch of decreasing intensity will exchange stability with the off solution we can infer that it is born as an unstable equilibrium, becoming stable but unphysical in a transcritical threshold bifurcation. The increasing branch however, may be born as a stable or unstable object. If it is stable we will have an on/off bistability for the range of p between the transcritical and saddle node bifurcations.

The other possibility is that the increasing branch is born as an unstable object. In this case for increasing p at p_{TC} there are no remaining stable and physically allowed equilibrium states in the system. Because on physical grounds we expect to see CW output at large values of p, we must conclude that since there are no stable equilibrium

states at threshold, the CW state must have become unstable with decreasing current density at an intermediate value of p. An undamping of the relaxation oscillations of the CW state in a Hopf bifurcation for decreasing p could then account for the dynamics observed at large pump in Fig. 2.1 and Fig. 2.2.

We now look at the stability of the steady state solutions with respect to Hopf bifurcations. The conditions that determine the occurrence of Hopf bifurcations in the LSA system can be found from the characteristic equation of the system. The characteristic equation is found from the determinant of the Jacobian (2.37). The characteristic polynomial for the system is given by

$$a_3\lambda^3 + a_2\lambda^2 + a_1 b\lambda + a_0 c = 0 \tag{2.41}$$

where

$$\begin{aligned} a_3 &= 1 \\ a_2 &= -(\alpha_{11} + \alpha_{22} + \alpha_{33}) \\ a_1 &= (\alpha_{11}\alpha_{22} + \alpha_{22}\alpha_{33} + \alpha_{11}\alpha_{33} - \alpha_{12}\alpha_{21} - \alpha_{13}\alpha_{31} - \alpha_{23}\alpha_{32}) \\ a_0 &= -(\alpha_{11}\alpha_{22}\alpha_{33} - \alpha_{11}\alpha_{23}\alpha_{32} + \alpha_{12}\alpha_{23}\alpha_{31} - \alpha_{12}\alpha_{21}\alpha_{33} + \alpha_{13}\alpha_{21}\alpha_{32} - \alpha_{13}\alpha_{22}\alpha_{31}) \end{aligned} \tag{2.42}$$

We know that $\alpha_{11} = 0$ along the steady state solutions of the system, which simplifies the calculation of the coefficients of the characteristic polynomial. The coefficients are given by

$$\begin{aligned} a_3 &= 1 \\ a_2 &= -\alpha_{22} - \alpha_{33} \\ a_1 &= \alpha_{22}\alpha_{33} - \alpha_{12}\alpha_{21} - \alpha_{13}\alpha_{31} \\ a_0 &= \alpha_{12}\alpha_{21}\alpha_{33} + \alpha_{13}\alpha_{22}\alpha_{31} \end{aligned} \tag{2.43}$$

The Routh-Hurwitz criteria provides a convenient method to determine the stability of equilibrium states of a dynamical system. The criteria are both necessary and sufficient tests for stability. It works by determining the number roots of a system in the right half of the complex plane as well as the number of roots along the imaginary axis. In this way we can determine the stability of a polynomial without needing to find the exact location of the roots, which for large systems can be prohibitively time consuming. The Routh array of this system is given by

λ^3	a_3	a_1	0
λ^2	a_2	a_0	0
λ^1	γ	0	0
λ^0	β	0	0

where

$$\gamma = \frac{-\begin{vmatrix} a_3 & a_1 \\ a_2 & a_0 \end{vmatrix}}{a_2} = \frac{a_2 a_1 - a_0}{a_2}$$

and (2.44)

$$\beta = \frac{-\begin{vmatrix} a_2 & a_0 \\ \gamma & 0 \end{vmatrix}}{\gamma} = a_0.$$

We find that necessary and sufficient conditions for stability are:

(i) all coefficients a_2, a_1 and $a_0 > 0$ *and*

(ii) no change of sign in the first column.

More simply, we require that a_2, a_0 and $a_2 a_1 - a_0 > 0$. For the current system, the condition $a_2 a_1 - a_0 = 0$, which we label RH, gives us

$$RH = \frac{1}{T}\left(x^2 y + x y^2\right) + (1-\rho) g_g N_g^0 I \left[G(n_g^0) + g_g N_g^0 n_g\right] x - \rho (g_q N_g^0)^2 n_q I y \quad (2.45)$$

where

$$x = (1 + g_g N_g^0 I)$$
$$y = (\Delta + g_q N_g^0 I)$$

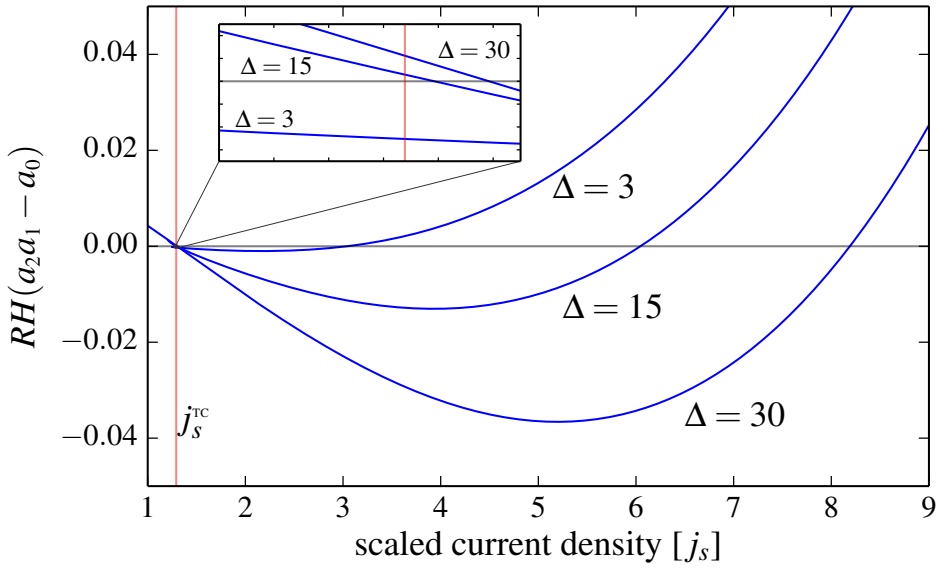

Figure 2.8: The RH condition versus the scaled current density j_s, for a series of Δ values. The solid vertical line indicates the position of the device threshold j_s^{TC}. The roots of the RH condition provide the location of the Hopf bifurcations of the system given by (2.45). Inset: Behaviour close to threshold, for $\Delta = 15$ and 30 there is a Hopf bifurcation just after threshold.

The roots of (2.45) provide exact solutions for the location of the Hopf (HP) bifurcations

of the system. In Fig. 2.8 we have plotted the RH condition for the same data as in Fig. 2.5 (b) and Fig. 2.6. For each successively larger value of Δ, we see larger intervals of p where the equilibrium states of the system are unstable. From Fig. 2.8, we see that in the case of $\Delta = 3$ there are no stable and physically allowed steady-state solutions, and self pulsating (SP) dynamics are therefore observed immediately at threshold. This is the limit considered in detail in [41], where it was shown that for $T \gg 1$, the self-pulsing orbit is born in a homoclinic bifurcation between p_{SN} and p_{TC}. For the larger values of Δ we see a small region in p just after threshold where the steady state is both physically allowed and stable. This bifurcation sequence can therefore account for the dynamical sequence observed in our experimental measurements in Fig. 2.1 and Fig. 2.2, where we found a brief window of CW operation at threshold, followed by two subsequent Hopf bifurcations into and out of a self-pulsating state for increasing p.

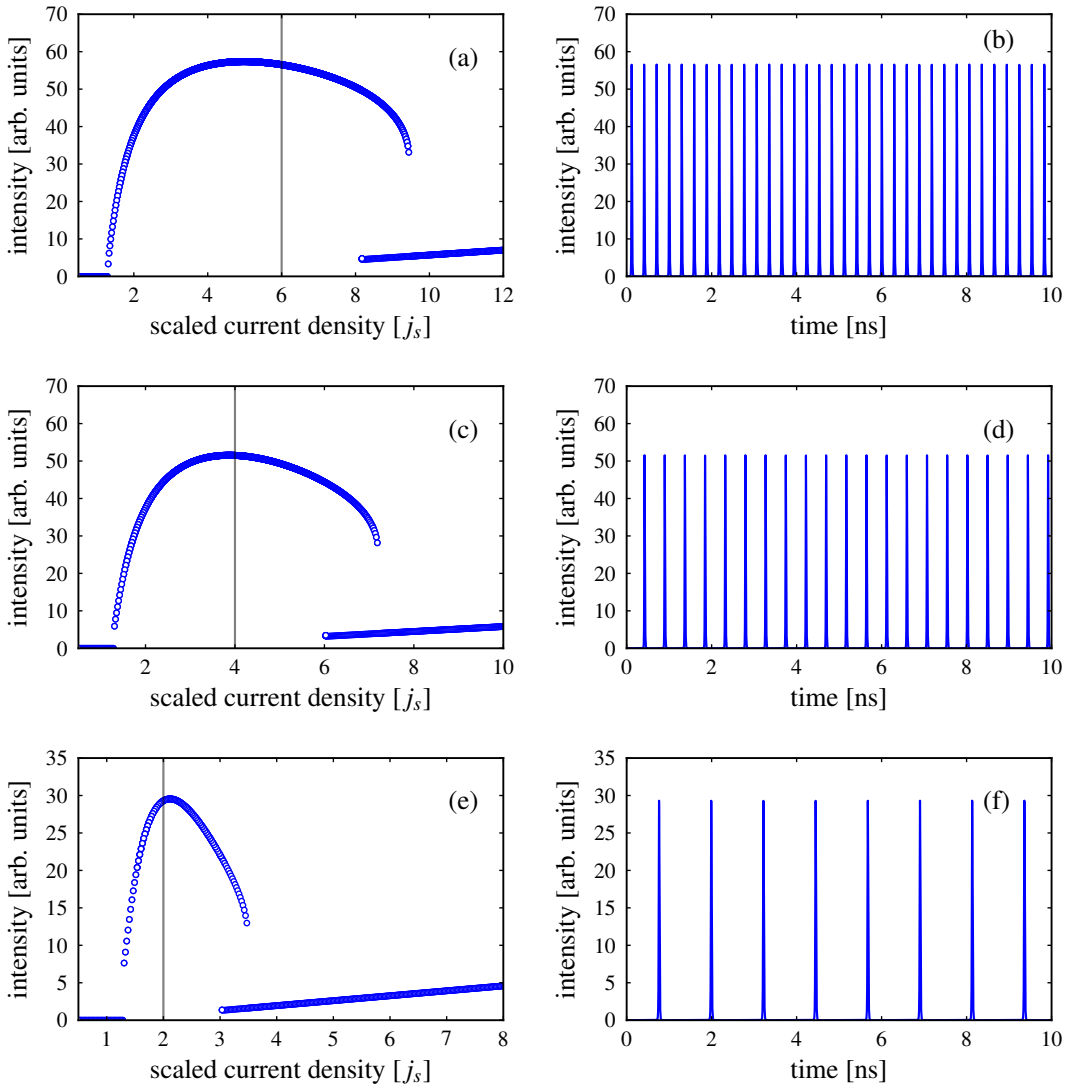

Figure 2.9: Left panels: simulated bifurcation diagrams. Right panels: time traces from the centre of the SP region in each case. (a) and (b): $\Delta = 30$. (c) and (d): $\Delta = 15$. (e) and (f): $\Delta = 3$. All other parameters are the same in each case, as shown in Table 2.1

Numerical bifurcation diagrams and time traces taken from the centres of each of the SP regions are shown in Fig. 2.9. These data describe the dynamics of a two-section device where the absorber recovery time is adjusted such that $\Delta = 30$, 15 and 3 for each of Fig. 2.9 (a), (c) and (e) respectively. Here we can see the influence of varying Δ on both the amplitude of the pulses and the extent of the SP region. These, and all subsequent numerical simulations, were calculated using a 4th order Runge-Kutta method with a step size corresponding to 400 samples per cavity round trip, and a 100 ns transient. In Fig. 2.9, the locations of the Hopf bifurcations at small and large values of the pump current are determined by the change in the RH stability criterion as shown in Fig. 2.8. In the example of Fig. 2.9, the second Hopf bifurcation is of a subcritical nature, which results in the presence of a small region of bistability around the boundary of the SP region at larger pump. The diagram shows a combination of two numerical simulations, one starting at large pump current and the other starting below threshold in order to fully capture the nature of the bistable region.

A time trace taken from the middle of the SP region in Fig. 2.9 (a) is shown in Fig. 2.9 (b). The duration of these pulsations is very short with a frequency of 3.4 GHz, and we find that the pulsation frequency is of the same order throughout the self-pulsation region. In Fig. 2.9 (c), with $\Delta = 15$, the SPs are once again born at and vanish at Hopf bifurcation points, with the SP frequency following a similar trend as in the $\Delta = 30$ example. However, in the final figure, Fig. 2.9 (e), where $\Delta = 3$, the SPs appear immediately at threshold, as the SP orbit is born in a homoclinic bifurcation. In contrast to the situation for larger values of Δ, the period of the SPs becomes infinite as the bifurcation point is approached. This is a consequence of the fact that no stable steady-state solutions are available at the device threshold for $\Delta = 3$, as shown in Fig. 2.8. One can see already the influence of this divergence in the time traces shown in Fig. 2.9 (f), where the SP frequency from the centre of the SP region is markedly lower than the other examples. In the case of Fig. 2.9 (f) the low frequency is partly a result of infinite period homoclinic bifurcation near threshold. This phenomenon can be difficult to observe experimentally however because of vanishing intensity and the impact of noise close to threshold [48].

We will now describe the bifurcation structure that governs the appearance of SPs as the physical parameters of the LSA model are varied. In other studies of this system [41], the primary focus of the study has been the parameter T, which is determined by the carrier lifetime in the gain section and the photon decay rate. A consequence of the structure of the system of Eq. 2.22 is that the steady states of the system, (Eq. 2.25) are completely independent of T, which greatly simplifies the study of its effects. Fig. 2.10 (a) shows the line of Hopf bifurcations in the $p - 1/T$ parameter space for $\Delta = 3$. As the steady states of the system are not impacted, this means that both p_{SN} and p_{TC} can be represented as vertical lines in the $p - 1/T$ plane. In Fig. 2.10 (a) the point where the SN bifurcation (which has no T dependence) coincides with the line of Hopf

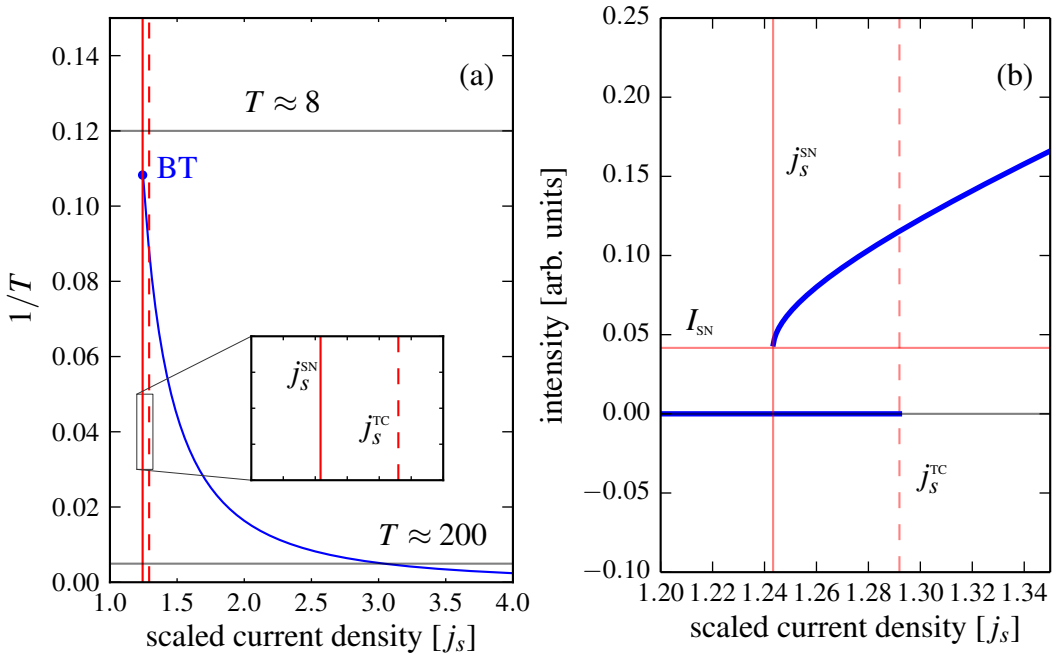

Figure 2.10: (a) Hopf bifurcation line as a function of the pump current and $1/T$ for $\Delta = 3$. The vertical solid line is the position of the SN bifurcation j_s^{SN}, the dashed line is the device threshold j_s^{TC}. The horizontal line at $T \approx 200$ corresponds to the numerical bifurcation diagram shown in Fig. 2.9 (e). (b) Numerical bifurcation diagram for $T \approx 8$.

bifurcations is a Bogdanov-Takens (BT) bifurcation. A double zero eigenvalue occurs at a BT bifurcation, with SN, Hopf, and homoclinic bifurcation curves all emanating from this point. The SN and Hopf curves are shown in Fig. 2.10 (a). The homoclinic curve (not shown) lies between the SN and TC lines, starting at the BT point along the SN line and meeting the TC line at $1/T = 0$. A sweep through this diagram in the limit of small T results in Fig. 2.10 (b), where there is an on-off bistability, but no SPs. A notable property of this $p - 1/T$ parameter space is that, in the arrangement shown in Fig. 2.10 (a), there is no value of T that leads to the observation of a steady state just after threshold followed by a region of SPs. The failure of the $p - 1/T$ parameter space to account for such a sequence means it cannot satisfactorily account for the experimental results observed in Fig. 2.1 and Fig. 2.2.

In Fig. 2.11 we add the Hopf lines to the earlier Fig. 2.7 (a). The geometry of the Hopf lines accounts for all of the features of the numerical bifurcation diagrams of Fig. 2.9. In this figure we now have two BT points along the SN line, with a Hopf line emanating from each. As in Fig. 2.7, the CP point marks the point where the SN and TC bifurcation lines coincide. The lines of Hopf bifurcations mark the beginning and end of the SP region, which expands significantly for large values of Δ.

At this stage we can make some preliminary conclusions about the experimental agreement of the LSA model. The bifurcation sequence observed at $\Delta = 15$ and

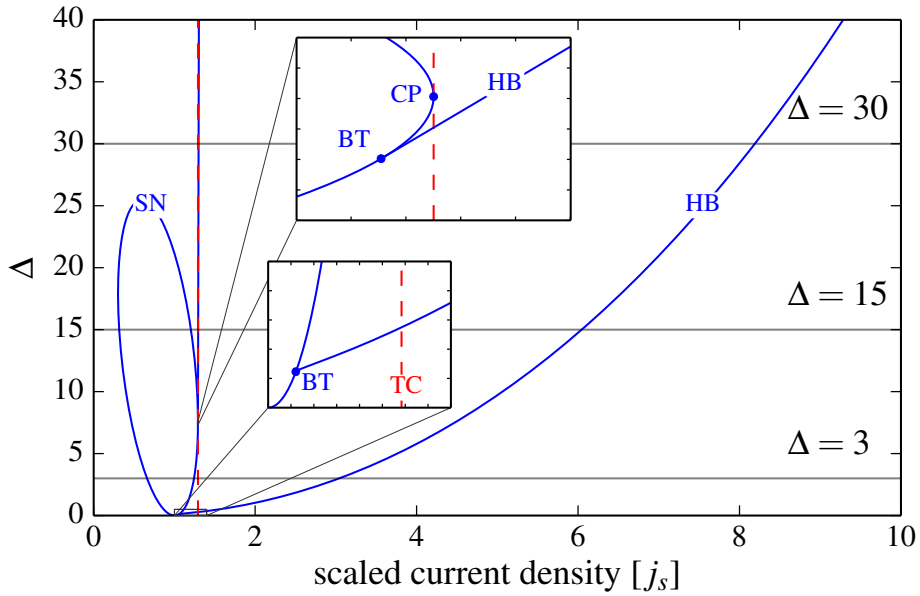

Figure 2.11: Extension of Fig. 2.7 to include position lines of Hopf bifurcations given by the roots of (2.45)

30 adequately explains the sequence of events we observed experimentally at the beginning of this chapter. At these large values of Δ however, while the sequence of bifurcations accounts for the experimental results the width of the SP region is overestimated to a large extent. The width of the SP region at $\Delta = 3$ is closer to experiment, although it is still overestimated, with the SP region extending to 3 times the device threshold. Furthermore, in this case the bifurcation sequence observed cannot be reconciled with the experimental measurements. In Fig. 2.9 (e) we observe SPs directly after threshold, which is in direct contravention with the experimental observation of a narrow, yet distinct region of CW output directly after the device threshold in Fig. 2.2. The numerically integrated results shown in Fig. 2.9 for both of these values result in uncharacteristically singular pulse shapes, which are not commensurate with the results of Fig. 2.3. In order to make a fair judgement on the suitability or otherwise of the LSA model of our devices, it is necessary to calibrate our model parameters using experimental data. In the following section we will use physically motivated arguments to determine the model parameters. We will then use these generated parameters to assess the suitability of the LSA model for quantitative modelling of the SP regimes.

2.5 Parameter extraction based on an analytical model of the semiconductor susceptibility

In the previous section we outlined the principal relevant operating regimes of system (2.22). We also reviewed the relationships between the different regimes, and we uncovered the underlying bifurcation structure. In order to compare our model with the experiments from Section 2.2, we must establish the dependence of the gain and absorption in the device as a function of carrier density and frequency. Ref. [39] provides a very convenient model that can be fitted to measured gain and absorption obtained using the Hakki-Paoli method. This work developed an analytical expression for the susceptibility of a quantum-well semiconductor material at low-temperature and has been used extensively to model the gain and saturable absorption in simulations of free-running and mode-locked semiconductor lasers [28, 49, 50]. The approximation considers a parabolic band and 0 K as the operating temperature.

While the model results cannot be regarded as quantitative, they nevertheless provide a qualitative description of the material susceptibility that is very useful for obtaining physically appropriate parameters to be used in simulations. These simplified methods also allow us to evaluate and compare various numerical models with experimental results, and they can provide a picture of general physical principles that can inform further simulation efforts which employ more sophisticated models of the semiconductor susceptibility. The result given by the model for the modal gain is [39]

$$G(\lambda, D_g) = G_0(\tan^{-1}[u] - 2\tan^{-1}[u - D_g] - \pi/2) \tag{2.46}$$

where λ is the wavelength, G_0 is the material gain coefficient, D_g is the carrier density normalised to the transparency value, and

$$u = \frac{2\pi c}{\gamma_p^{\mathrm{G}}}\left(\frac{1}{\lambda} - \frac{1}{\lambda_{bg}^{\mathrm{G}}}\right) + \sigma D_g^{1/3}. \tag{2.47}$$

Here, $\lambda_{bg}^{\mathrm{G}}$ is the nominal transition wavelength, σ describes the bandgap shrinkage with increasing carrier density, and γ_p^{G} is the linewidth of the optical transition.

We now fit this expression to the modal gain of the active material, G, which we determine using the Hakki-Paoli technique. For these measurements a single current density over the full length of the device was maintained. The negative offset at long-wavelength gives an estimate of the background losses, α_{int}, which are assumed to be wavelength independent and uniformly distributed over the device length. The results of the fit that we obtained for a series of values of the device current density are shown in Fig. 2.12 (a). The mirror losses of the device are estimated to be $\alpha_m = 13.8\ \text{cm}^{-1}$ and we find that the background losses, $\alpha_{\text{int}} = 9.2\ \text{cm}^{-1}$, as indicated in Fig. 2.12 (a).

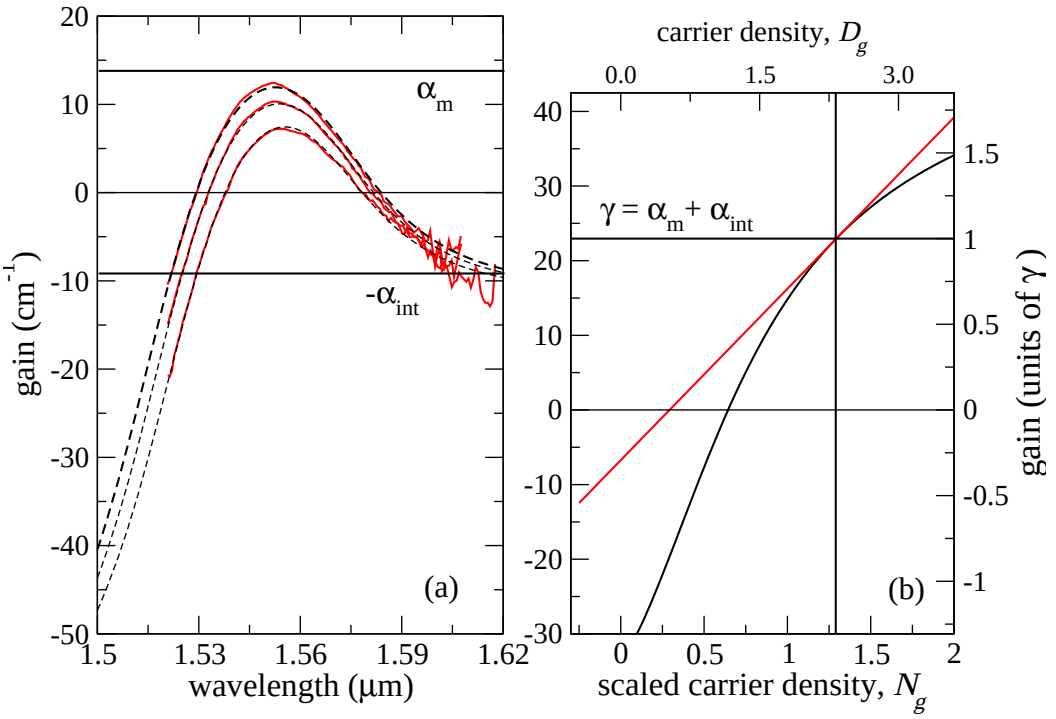

Figure 2.12: (a) Measured modal gain of the Fabry-Pérot laser for a series of values of the current density. A fit to these data obtained for different values of the carrier density variable are also shown. The mirror losses are α_m and the background losses are α_{int} as shown. (b) Variation of the fitted modal gain as a function of carrier density. The wavelength is chosen to be the location of the peak gain at threshold for the Fabry-Pérot laser. The threshold modal gain, γ, is equal to the sum of the mirror and background losses in the device. The differential gain at threshold is defined to be equal to one in normalised units.

From the resulting fit to the data, we determine the value of the carrier density at threshold for the single-section FP laser. Fixing the wavelength at the location of the peak gain at threshold, we determine the differential gain at threshold for the FP laser. We then define the threshold gain and differential gain at the gain peak to be equal to one in normalised units. This scaling then defines our normalised carrier density variable, N_g. The variation of the material gain at the gain peak as a function of carrier density is shown in Fig. 2.12 (b). Here we have plotted the data in physical units and in normalised units. The differential gain at threshold is $\tilde{g}_g = 12.7\ \text{cm}^{-1}[\equiv 1$ in normalised units$]$. Fitting parameters for the susceptibility function are presented in Table 2.2. The values of D_g and N_g at threshold are 2.33 and 1.29 respectively. We have found that the presence of the σ parameter leads to a certain freedom in determining the appropriate bandgap wavelength for the gain section. The value 0.8 was chosen as it gave the best agreement with the measured peak gain at threshold as the reverse bias voltage was varied.

To determine the modal absorption in the reverse bias section, A, we employ a differential Hakki-Paoli technique. The modal absorption is found from the difference between

Table 2.2: Fitting and derived parameters for the gain function.

$\lambda_{bg}^{\mathrm{G}}$	G_0	γ_p^{G}	σ	λ_0	$\tilde{g}_g$
[nm]	[cm^{-1}]	[10^{13}s^{-1}]		[nm]	[cm^{-1}]
1545.0	21.1	2.0	0.8	1551.5	12.7

the modal gain measured with a uniform current density over the whole device length and the modal gain, $G^{'}$, measured with the same current density applied to the long section and a given voltage applied to the short section. The relationship is

$$\rho A(V,\lambda) = G^{'}(V,j,\lambda) + \alpha_{\text{int}} - (1-\rho)G(j,\lambda). \tag{2.48}$$

To fit the derived absorption curve we use the expression

$$A(\lambda, D_q) + \alpha_{\text{abs}} = \quad A^0[\mathrm{V}](\tan^{-1}[u] - 2\tan^{-1}[u - D_q] - \pi/2), \tag{2.49}$$

where D_q is the carrier density normalised to the transparency value as before, the material absorption coefficient, $A^0[\mathrm{V}]$, is now a function of voltage, and

$$u = \frac{2\pi c}{\gamma_p^{\mathrm{Q}}}\left(\frac{1}{\lambda} - \frac{1}{\lambda_{bg}^{\mathrm{Q}}[\mathrm{V}]}\right).$$

Here we have neglected the σ parameter as the carrier density is taken to be much smaller in the reversed biased section. However, in order to obtain a reasonable fit to the data we have had to introduce a voltage dependent bandgap wavelength $\lambda_{bg}^{\mathrm{Q}}[V]$. We have also included an additional carrier density and voltage independent contribution to the absorption in the absorber section, α_{abs}. This was necessary because, while the above expression can fit the absorption function accurately near the bandedge, we found that the derived carrier density was close to the transparency value, which led to an unphysically large value for the differential absorption of the material. We therefore included a small offset, $\alpha_{\text{abs}} = 2.5$ cm^{-1}, in order to obtain accurate fits of the function with small values of the carrier density appropriate for a reverse biased section. Note also that the transition linewidth in the absorber section was taken to be $\gamma_p^{\mathrm{Q}} = 0.85 \times 10^{13}$ s^{-1}. This change in the value of the transition linewidth and the voltage dependence of $\lambda_{bg}^{\mathrm{Q}}$ are consistent with the quantum-confined Stark effect [49].

Experimental and fitted absorption curves for two values of the reverse bias voltage are shown in Fig. 2.13. The absorption curves are only accurate for wavelengths above a characteristic cutoff that depends on the applied voltage. In all cases however, the fits are very close to the measured data for wavelengths larger than approximately 1555 nm, and we will assume that our fits to the absorption are accurate at all wavelengths of interest over this voltage range. A table of fitting parameters for the modal absorption function obtained for voltages ranging from 0.0 to -1.0 V are shown in Table 2.3. Here

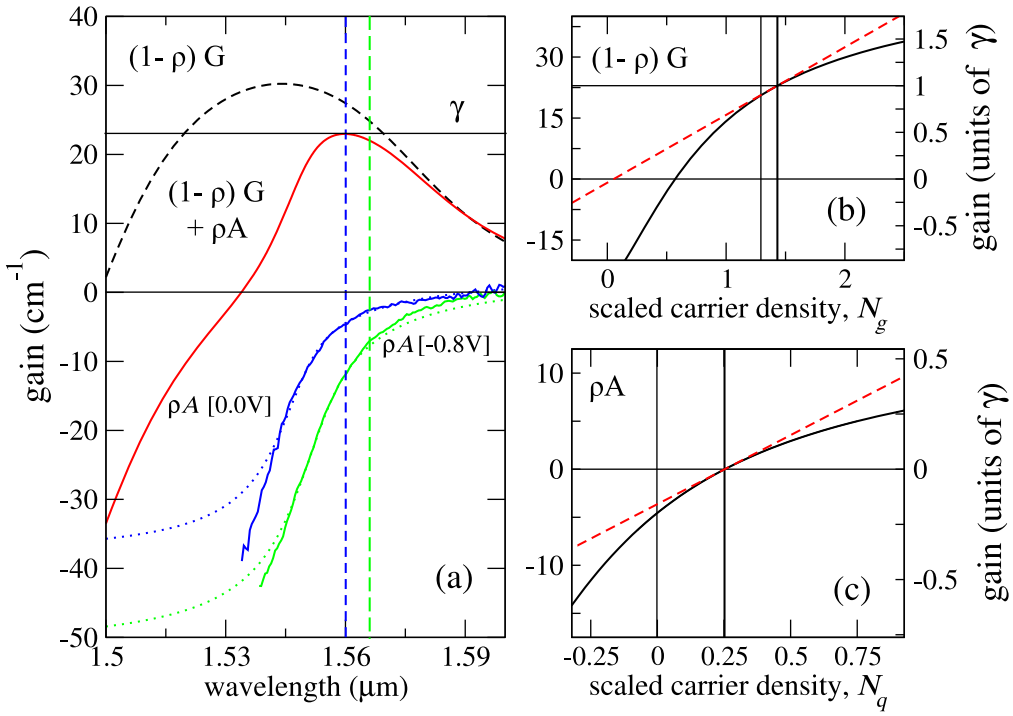

Figure 2.13: (a) Fits to the modal absorption, ρA, at two values of the reverse bias as shown. The modal gain $(1-\rho)G$, and the net gain, $(1-\rho)G+\rho A$, in the two-section device are also shown. The peak of the net gain at threshold determines the wavelength for the calculation of the differential gain and absorption. The variation of this wavelength with reverse bias is indicated by the dashed vertical lines. (b) Variation of the modal gain in the two-section device with carrier density at the wavelength of the peak net gain indicated in (a). The vertical lines indicate the threshold carrier density in the FP and the carrier density in the two-section device assuming a transparent absorber section. (c) Variation of the modal absorption in the two-section device with carrier density. The reverse bias voltage is 0 V, and the wavelength is the same as in (b). The carrier density is zero in the unsaturated device, and the differential absorption is defined at the saturated value.

Table 2.3: Fitting parameters obtained for the modal absorption function for a range of reverse bias voltages.

bias	λ_{bg}	ρA^0	D_q^0	λ_0	ρA^0
[V]	[nm]	[cm^{-1}]		[nm]	[cm^{-1}]
-0.0	1551.9	13.3	0.33	1559.5	4.6
-0.2	1552.3	14.7	0.31	1561.0	5.4
-0.4	1553.4	15.8	0.29	1562.5	6.3
-0.6	1554.7	16.6	0.27	1564.0	7.0
-0.8	1555.9	17.6	0.24	1565.5	7.9
-1.0	1557.7	18.3	0.22	1567.5	8.6

D_q^0 is the value of the carrier density used to fit the measured [unsaturated] absorption.

To define our model parameters we must choose a reference wavelength and carrier density values in each section where the modal gain and absorption functions are linearised. For each voltage value we first determine the reference wavelength as the location of the peak of the net gain in the device at threshold. We then linearise the gain and absorption functions at this wavelength, but we do not linearise the gain function at the threshold carrier density. Instead, we linearise around the gain value that corresponds to the threshold gain assuming a transparent absorber section: $G = G_0 + \tilde{g}_g(N_g - N_g^0)$, where $G_0 = G(N_g^0) = (1-\rho)^{-1}\gamma$. For the absorber section, we linearise the absorption function at the saturation value of the carrier density. Apart from determining the absorption curve directly, in this way the voltage parameter enters the linearisation indirectly through the choice of wavelength. Because of material dispersion, this approach leads to a change in the threshold carrier density with voltage even though the threshold is defined assuming a transparent section. This is illustrated in Fig. 2.13 (a), where we have plotted the modal gain and the sum of the modal gain and absorption at the threshold carrier density for a reverse bias of 0 V. The dashed vertical line at the location of the peak gain defines the reference wavelength λ_0. The dashed line at longer wavelength is at the location of the peak gain at threshold at a reverse bias of -0.8 V.

Table 2.4: Fitting and derived parameters obtained as a function of reverse bias voltage

bias	N_g^0	g_g	ρg_q
[V]			
-0.0	1.43	0.73	0.63
-0.2	1.45	0.70	0.63
-0.4	1.49	0.67	0.65
-0.6	1.53	0.63	0.67
-0.8	1.60	0.58	0.68
-1.0	1.68	0.54	0.70

Fig. 2.13 (b) and Fig. (c) show the modal gain and absorption as a function of carrier density at the reference wavelength for a reverse bias of 0 V. The differential gain at the peak gain wavelength is $\tilde{g}_g = 9.3$ cm^{-1}, and the differential absorption is $\rho\tilde{g}_q = 8.0$ cm^{-1}. The calculated differential gain g_g and differential absorption g_q as a function of reverse bias voltage are shown in Table 2.4. Here we have included the threshold carrier density N_g^0 as defined above, and the differentials are given in dimensionless units defined by the total losses γ.

Notice how the calculated reference wavelengths, λ_0, as shown in Table 2.3, are in good agreement with the experimentally measured values of the peak emission at threshold. The numerical results are plotted alongside the experimental measurements in the inset of Fig. 2.3. The values obtained for the threshold currents are slightly larger than the measured values at larger reverse bias values. This reflects the approximate nature of

the gain function, which appears to underestimate the differential gain with increasing carrier density. The calculated reference wavelengths have a close to linear dependence on the applied reverse bias applied.

To define the reference wavelength in each case we have assumed a linear absorber and taken the location of the peak gain at the device threshold. However, as we then linearise around the gain value corresponding to the threshold gain assuming a transparent absorber section, this can entail a large shift in wavelength. The fact that we reach threshold at a wavelength strongly detuned from the reference wavelength is evidenced by the large values of N_g^0. Strictly speaking, the relatively large values of N_g^0 should be accompanied by correspondingly smaller values of g_q. However, we choose not to make this adjustment, as we have found it does not significantly affect the results.

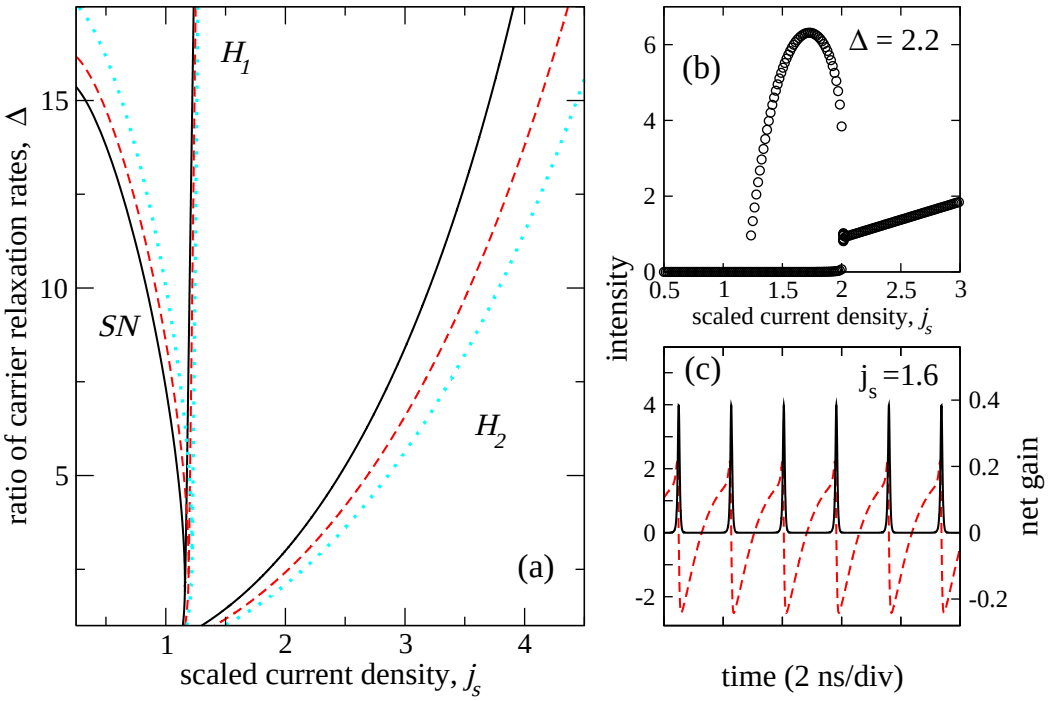

Figure 2.14: (a) Curves of saddle-node (SN) and Hopf ($H_{1,2}$) bifurcations in the $j_s - \Delta$ plane for parameters at 0.0 V (solid lines), -0.2 V (dashed lines), and -0.4 V (dotted lines). (b) Numerical bifurcation diagram with parameters for -0.4 V and $\Delta = 2.2$. (c) Time traces of intensity and dimensionless net gain parameter with $j_s = 1.6$. Other parameters are as in (b).

The final requirement to complete our model is that we must specify the values of the carrier recovery times in the gain and absorbing sections of the device. We use the measured variation of the relaxation oscillation frequency to estimate the carrier lifetime in the gain section. The noise driven peak in the power spectrum of Fig. 2.2 (b) is a signature of damped relaxation oscillations. At a drive current of 40 mA, the peak is at 3.7 GHz. If we neglect the influence of the saturable absorption, the relaxation

oscillation frequency is equal to

$$\omega_{\text{RO}} = \sqrt{\frac{\gamma_{\text{phtn}}(j_s - 1)}{\tau_{\text{g}}}} \tag{2.50}$$

We estimate the threshold for this device, assuming a transparent absorber section to be $(1-\rho)^{-1} I_{\text{thr}}[\text{FP}] = 14.3$ mA. At 40 mA we then have $p \simeq 1.8$. Using the derived parameters for the device at -0.6 V, we find that $T \simeq 130$, which gives $\tau_g = 0.6$ ns. We will defer making an estimate of carrier lifetime in the absorber section until we make a comparison between our experimental results and the results of simulations with a model based on a delay-differential system of equations. At this stage we note only that the carrier lifetime in the absorber section is in general shorter than in the gain section, with a strong dependence on the applied bias [51].

Curves of saddle-node and Hopf bifurcations found with parameters for reverse bias voltages of 0.0, -0.2, and -0.4 are plotted in the $j_s - \Delta$ plane in Fig. 2.14. One can see that a larger value of Δ leads to a larger SP region, and that the LSA model predicts SPs to occur at zero volts, even with $\Delta = 1$. In order to compare the results of simulations with experiment, we have plotted a numerical bifurcation diagram in Fig. 2.14 (b) with parameters for a reverse bias of -0.4 V. We have taken $\Delta = 2.2$ for this simulation, in which case the SP region is bounded by a pair of Hopf bifurcations. We choose this value of Δ to ease comparison with results of the next section, for reasons which will become clear. Time traces of the total intensity and the dimensionless net gain parameter, $(G + A - \gamma)L_c$ with $j_s = 1.6$ are shown in Fig. 2.14 (c). These time traces can be compared with the experimental SP time trace from the inset of the upper panel of Fig. 2.3.

In Fig. 2.9 (e) we presented simulations in which the region of self pulsations was bounded by a homoclinic and Hopf bifurcation at large pump current for a small value of Δ. We observed at the time that this behaviour does not correspond to experimental results from Fig. 2.1 and Fig. 2.2. Here however, with the calibrated description of the dispersion the LSA model gives us the correct bifurcation sequence. The region of self pulsation after threshold is now bounded by two Hopf bifurcations, one just after threshold, and the other at large pump current. Despite this qualitative agreement, at the quantitative level we have not obtained a satisfactory description of our experiment. In the time domain, as shown in Fig. 2.14 (c), the simulated pulsations are very narrow, and they have a much lower frequency than we observe experimentally. This is not reflective of the behaviour seen in Fig. 2.3. Although the results of the LSA simulations are inconclusive, given the small extent of the SP region for small reverse bias voltages, it seems a small value of Δ is implied. Overall, the results of Fig. 2.14 are in poor agreement with the experimental results presented at the beginning of this chapter.

Much of the complication with achieving quantitative agreement follows from proper-

ties inherent to the semiconductor laser. As the large gain and loss of the semiconductor laser are not described with sufficient accuracy by the LSA model, we need a better estimate, particularly as the next modelling stage will be further complicated by many independent parameters. To this end, in the next section we will briefly present a time domain model of a two-section semiconductor laser that can provide a more physically accurate description of the observed dynamics. This model is based on a delay-differential equation for the field variable.

2.6 Delay-differential equation model of the device dynamics

The results of the previous section highlight the importance of accounting for large gain and loss when modelling the dynamics of two-section semiconductor lasers with saturable absorbers. Quantitative dynamical models of semiconductor lasers with saturable absorbers include travelling-wave methods that consider the spatio-temporal dynamics of the slowly-varying electric fields [28, 52]. A lumped element time domain model has also been developed that eliminates the spatial dependence of travelling-wave models in favour of a delay-differential equation for the field variable [29, 53, 54]. This model is significantly easier to implement and requires minimal computing resources as compared to a fully distributed spatio-temporal model, but it also accounts for the large gain and loss in the semiconductor laser. The model is derived assuming a unidirectional travelling electric field profile in a ring cavity geometry, and assumes a Lorentzian gain profile. The model was originally developed in order to study mode-locking in semiconductor lasers, but it also describes SP and QSML solutions. The system of equations is

$$\begin{aligned}
\gamma_G \dot{E}(t) &= -E(t) + \sqrt{\kappa} R(t-\tau) E(t-\tau) \\
\dot{g} &= g_0 - \gamma_r g - \exp -q(\exp g - 1)|E|^2 \\
\dot{q} &= q_0 - q - s(1 - \exp -q)|E|^2
\end{aligned}$$

where

$$R(t) = \exp\left[\frac{1}{2}(1 - i\alpha_g)g - \frac{1}{2}(1 - i\alpha_q)q - i\phi\right]$$

and

$$\kappa = \exp\left[-(\alpha_{mir} + \alpha_{int})L_c\right].$$

In the above, τ is the round-trip time in the cavity, the dynamical variable for the gain is defined as $g = \int_{(1-\rho)L_c} dz \tilde{G}(z,t)$, and the saturable absorption is described by the variable $q = \int_{\rho L_c} dz \tilde{A}(z,t)$. Here $\tilde{G}(z,t)$ and $\tilde{A}(z,t)$ are respectively the modal gain and absorption, which are now assumed to be spatially varying. $\gamma_r = \gamma_g/\gamma_q = \tau_q/\tau_g$ is the ratio of the recovery times in the gain and absorber sections, and $s = g_q/g_g$ is the ratio of the material differential absorption and gain. $\alpha_{g,q}$ are the linewidth

enhancement factors in the gain and absorber sections of the device, and ϕ is the detuning of the gain peak from the nearest cavity mode. With the linearised gain and absorption variables defined as in the previous section, the scaled pump current is $g_0 = (1-\rho)L_c\gamma_q^{-1}[g_g j - \gamma_q(g_g N_g^0 - G_{\text{thr}})]$ and the parameter describing the unsaturated absorption is $q_0 = \rho L_c A^0$. The parameter γ_G defines the bandwidth of the gain medium, which is modelled through the action of a linear Lorentzian filter.

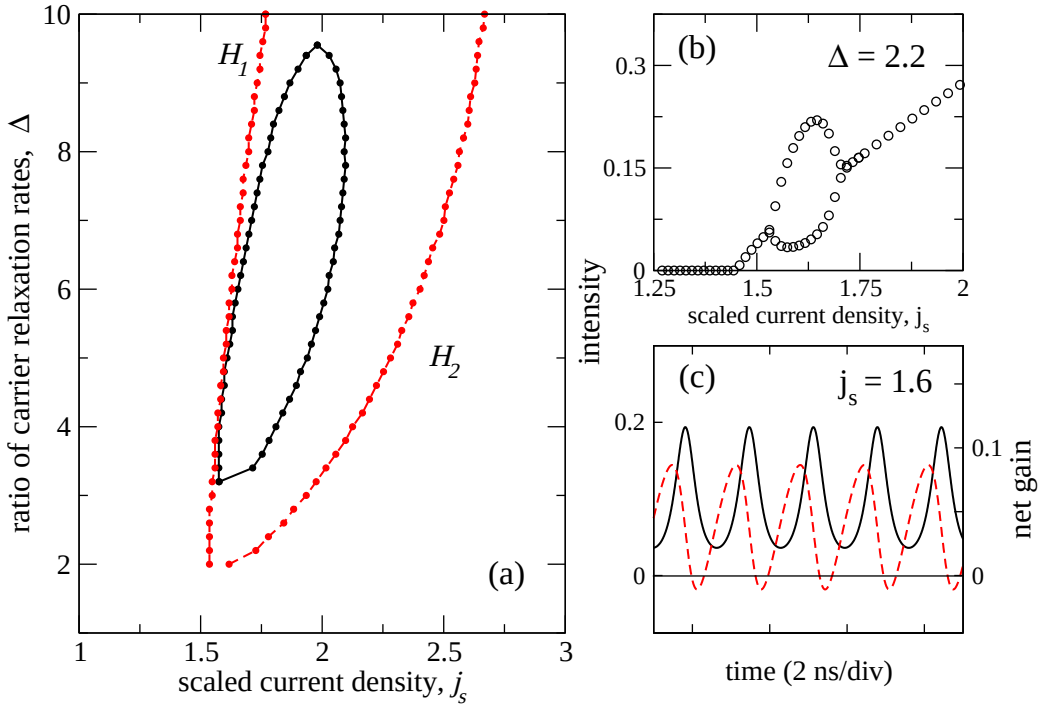

Figure 2.15: (a) Curves of Hopf ($H_{1,2}$) bifurcations in the $j_s - \Delta$ plane for parameters -0.2 V (solid lines), and -0.4 V (dashed lines). (b) Numerical bifurcation diagram with parameters for -0.4 V and $\Delta = 2.2$. (c) Time traces of intensity and dimensionless net gain parameter with $j_s = 1.6$. Other parameters are as in (b).

Fig. 2.15 (a) shows curves of Hopf bifurcations of the delay-differential model with calibrated parameters for -0.2 V and -0.4 V. This figure was obtained numerically by integrating the rate equations and finding the locations of the stability points by inspection. One can see that the exponential terms in these equations lead to a significant change in the structure of the dynamical phase-space when compared to the LSA model. With experimentally calibrated parameters, SPs only appear with values of the reverse bias larger than -0.2 V, but we can see that the minimum Δ value is too large to allow for a consistent match with other voltages. We therefore conclude that the model predicts SPs for reverse biases of at least -0.4 V. The variation of the width of the SP region with Δ then allows us to fit the measured SP region to the numerical data, and we find that the Δ value at onset is 2.2. This was the value used in our previous simulations of the LSA model, and we now repeat them with identical parameters. The results are shown in Fig. 2.15 (b) and (c). In (b) we see that the SP region is again

bounded by a pair of Hopf bifurcations of the steady-state solutions. In contrast to the results of the LSA model, the extent of the SP region is now accurately matched to our experimental results. We have a clearly visible region of constant output near threshold and we obtain a small amplitude harmonic modulation to begin, rather than the large amplitude pulsations that characterise the LSA system. Examining the numerical time trace of Fig. 2.15 (c), we can see that for these identical parameters, the SPs are more weakly modulated than those of the LSA model. The SP frequency is also smaller, and the size of the variation in the net gain parameter over the SP cycle is far more limited.

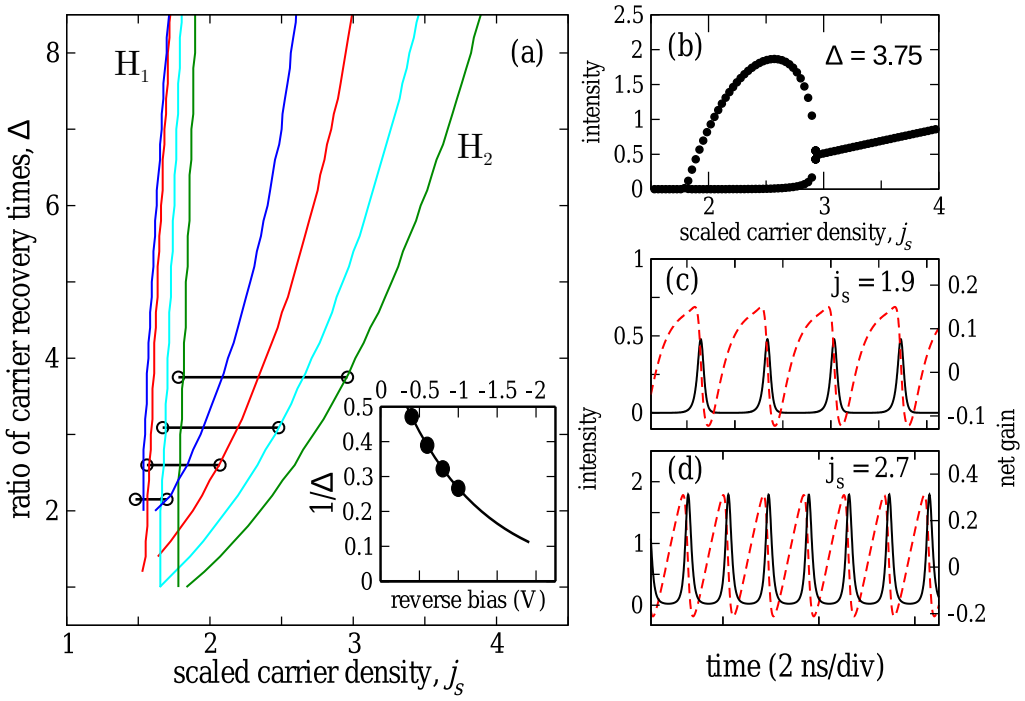

Figure 2.16: (a) Curves of Hopf ($H_{1,2}$) bifurcations in the $j_s - \Delta$ plane for parameters at -0.4 V (blue), -0.6 V (red), and -0.8 V (cyan), and -1.0 V (green). (b) Numerical bifurcation diagram with parameters for -1.0 V and $\Delta = 3.75$. (c) Time traces of intensity and dimensionless net gain parameter with $j_s = 1.9$. Other parameters are as in (b). (d) Time traces of intensity and dimensionless net gain parameter with $j_s = 1.9$. Other parameters are as in (b).

Fig. 2.16 (a) shows curves of Hopf bifurcations obtained numerically for model parameters ranging from -0.4 to -1.0 V. Here we have superposed the experimental results for the width of the SP region. By matching these, we can obtain an estimate of the Δ parameter as a function of voltage. In the inset of Fig. 2.16 (a), we have plotted $1/\Delta$ against voltage, and our results are consistent with a linear variation of this quantity for small voltages. This variation would follow if the carrier lifetime in the absorber section was varying as $\tau_q = \tau_q^0 \exp[-V/V_0]$, with V_0 much larger than 1, which was the functional form suggested in [51]. A numerical bifurcation diagram with parameters for -1.0 V and $\Delta = 3.75$ is plotted in Fig. 2.16 (b). Time traces of the intensity and the net gain taken with parameters for -1.0 V, and with j_s equal to 1.9 and 2.7 are shown in Fig. 2.16 (c) and (d) respectively. One can see that the SP frequency increases by more than a factor of two over this current range. This increase is similar to that found with

the LSA model, although the overall SP frequency is lower. This lower frequency may be due to the lower average intensity found with the DDE model. The result is that the numerical SP frequency near the upper boundary of the SP region at this voltage value is about 30% lower than in our experiment. As we mentioned, the increase of the SP frequency over the SP region is also not observed in our experiments, but we attribute this to the particular and uncharacteristic behaviour of the device.

The level of agreement between the numerical predictions of the SP region width and experiment is pleasantly surprising given the relative simplicity of the model of [39]. When calibrated with experimental parameters, simulations using the delay-differential model of the device provide both quantitative and qualitative agreement with experiment, which is a significant improvement on the results of the LSA system. Addressing individual modes with the DDE model is complicated by the fact that the model makes a total field approximation. To address individual modes with the model it would be necessary to selectively filter modes of interest. For the purposes of a multimode system with no modal selectivity this is not a concern. In subsequent chapters, where we will study the dynamics of dual-mode systems we deem this additional layer of complexity as overly burdensome. It does however, allow us to use physically motivated arguments to physically calibrate the value of Δ, which we have already seen has a significant bearing on the LSA system. Estimates of the value of Δ can be obtained experimentally using pump-probe techniques as in [51, 55]. Though beyond the scope of the work carried out in this thesis due to the challenging nature of the experimental technique, these measurements could provide a useful independent verification of our findings.

As the obtained value of 2.2 is quite close to the boundary, and since we don't expect to have qualitative agreement with the LSA system, we take a slightly larger value of $\Delta = 3$ for use in the next chapter. Having used the DDE model to obtain a physically appropriate estimate of Δ, we can proceed with numerical simulations using the LSA system. This model provides a natural framework for dealing with multimode systems. In [21] we discuss further results from the DDE system based on FP lasers and its potential application in mode locked systems.

2.7 Discussion and outlook

In this chapter we presented experimental measurements of self-pulsations in a two-section Fabry Pérot device. We modelled the observed behaviour using the LSA model, a dual-mode version of which will provide the basis for following chapters. A simple analytical model of the material susceptibility of our device provided a qualitative description which we used to experimentally calibrate the LSA model. In this simplified picture of the FP device, with a single dynamical variable representing the total field

intensity, the model fails to quantitatively predict the behaviour of our devices. This is primarily due to a failure of the LSA model to appropriately account for the large gains and losses typically found in semiconductor lasers.

As a result of the quantitative failures of the LSA model we modelled the SP behaviour using a more physically appropriate delay-differential equation model. In using the DDE model we found that it accurately described the observed SP dynamics. The success of the DDE model in this respect allows us to use it to estimate Δ, the ratio of the carrier lifetimes in the gain and absorber sections of the device. Comparing the results of the DDE model with those of the LSA model reveals the approximate nature of the LSA system. Our approach using the LSA model can provide qualitative agreement, but fails to quantitatively predict the extent of the SP region and the nature of the dynamics in the time-domain. The main sources of error which account for this are both the equations themselves and the fitting of the gain profile. In previous work by our group [38], a linearised gain function provided excellent experimental agreement for a single-section device. In this case however, a consequence of having two sections and saturation of the absorption is the potential for large changes in the carrier density in each section, which a linearised gain function fails to account for appropriately. This property is a limitation of these methods in general, even though they are otherwise ideal for frequency domain simulations with spectral filters, where the spatial dimension is neglected.

In our experimental results we observed movement of the gain peak due to the material dispersion, which provides a basis from which we can draw sensible conclusions about the stability of mode-locked solutions in multi-mode devices. The DDE results however, provide a significant improvement on the LSA model results with identical parameters. Together with the fact that our derived quantities are in general agreement with published values, this suggests that the parameter extraction approach is useful where the objective is to develop an understanding of qualitative trends in an efficient manner.

From this chapter we can conclude that Δ is a significant parameter, and that the results of the DDE model suggest that in the case of our devices it is quite small. However, we will not restrict ourselves to small values of Δ, but instead attempt to show our modelling approach can be successful in a number of regimes. By exploring in detail the relationship between Δ and the dynamics of the LSA system, we hope to gain valuable insight into the dynamical behaviour observed in both our experiment and numerical simulations.

We will show in the following two chapters that a multimode extension of the LSA model established here can provide a qualitative description of complex dynamics of coupled modes in dual-mode devices. As the LSA model can be used to describe and explain the physical origin of multimode instabilities in two-section devices, this

work can provide a basis for an approximate description of a mode-locked laser in a frequency domain picture of individual modes based on the LSA model with calibrated parameters.

Chapter 3

Dual-mode dynamics: Synchronisation of self-pulsations

3.1 Introduction

In the previous chapter we discussed in depth the structure and operating regimes of the single-mode LSA system. The understanding of the bifurcation structure of the single mode system that we have gained will be of critical importance as we turn our attention to the multimode LSA systems in this and the following chapters of this thesis. Our study of the bifurcation structure of the LSA system allowed us to find parameters that can describe the experimentally observed sequence of two Hopf bifurcations bounding the region of SPs. The appearance of this double Hopf structure in the system showed a strong dependence on Δ, the ratio of carrier lifetimes in each section of the laser diode. As the LSA model did not allow us to obtain an accurate estimate for the Δ parameter, we employed a DDE model and found that the value of Δ was limited. We also found that the DDE system provides a significantly better description of the self-pulsating regime, with reasonable quantitative agreement found between theory and experiment for an appropriate choice of parameters in the model.

In this chapter and the next we will focus our attention on dual-mode devices with saturable absorbers. The designs of the two devices that we will study are largely the same, but we will find that each has a distinct dispersion of the net gain and absorption as a consequence of the inherent variability in the manufacturing process. By experimentally investigating these dual-mode systems, we can test our theory and understanding of the role that material dispersion plays in these systems. We will confirm the small value of the Δ parameter through studies of optical and power spectral data as well as time traces of the intensity output of each device.

The device that will be characterised in this chapter provides an interesting example

of quasi-periodic antiphase dynamics. We will show that towards the centre of an observed region of dual-mode output in the device, the dynamics of the total output intensity are much simpler than those of the individual coupled modes. This behaviour is the signature of antiphase dynamics, and we will show that the dynamics in the device are strongly influenced by the interaction between the two modes, which have different characteristic SP frequencies. The behaviour in the system can then be interpreted within the framework of synchronisation phenomena, and although it is difficult to state with complete certainty, we will also demonstrate using measured data and numerical simulations that the dynamics can evolve further and bear many of the hallmarks of chaos. A dual-mode device with a large mode spacing is also an excellent candidate device for testing the effects of material dispersion on the dynamics as both modes can "see" radically different gain and absorption profiles.

The structure of this chapter is as follows. First we will introduce the design method for the dual-mode device. In order to introduce the concept of chaotic dynamics in multimode semiconductor lasers, we will then briefly discuss an interesting example of chaos in an optically injected dual-mode device as studied by our group [56]. We will then present experimental measurements of quasi-periodic antiphase dynamics from a dual-mode two-section laser diode, and in a similar fashion to Chapter 2 build a model of the observed experimental results. To do so we extend the single mode LSA model from Chapter 2. This extended model, combined with elements of the model of the semiconductor susceptibility from the previous chapter will allow us to study in detail the bifurcation structure of the two mode regime. We will then present qualitatively representative numerical results and compare them with our experiment. Finally we will present a two-dimensional bifurcation study in the pump parameter and Δ which offers further justification for the choice of a small value of Δ.

3.1.1 Dual-mode diode laser

We now consider the design approach and present experimental measurements from a single-section dual-mode device. Following our discussion of the design of a single mode device presented in Chapter 1, when designing a dual-mode device, the appropriate basis for the feature density or index pattern function is a pair of $sinc$ functions, centred at a given Fabry-Pérot mode m_0 and with a spacing of a underlying FP modes. The Fourier transform of this function is $\cos(\pi a \epsilon)$, for $-1/2 \leq \epsilon \leq 1/2$ and is zero otherwise. The feature density that results for the case $a = 4$ and one high-reflection HR coated mirror is shown in the left panel of Fig. 3.1. While in the single mode case the Fourier transform function we chose was always positive, the function $\cos(\pi a \epsilon)$ changes sign along the length of the cavity. At each zero of this function, the result is that additional $\pi/2$ phase shifts are introduced into the index pattern along the device length. Between each consecutive zero of the feature density function, a sampled

Bragg profile is created where each etched feature forms either a half or a quarter wave subcavity with the HR mirror.

The right hand panel of Fig. 3.1 shows measurements from a dual-mode device with a primary mode spacing of four modes and a device length of 350 μm. This determines the frequency spacing to be 480 GHz. For this device, with increasing current the short wavelength mode reaches threshold first with the two colour point at 43.5 mA. This is the device whose noise spectrum we presented in Fig. 2.4.

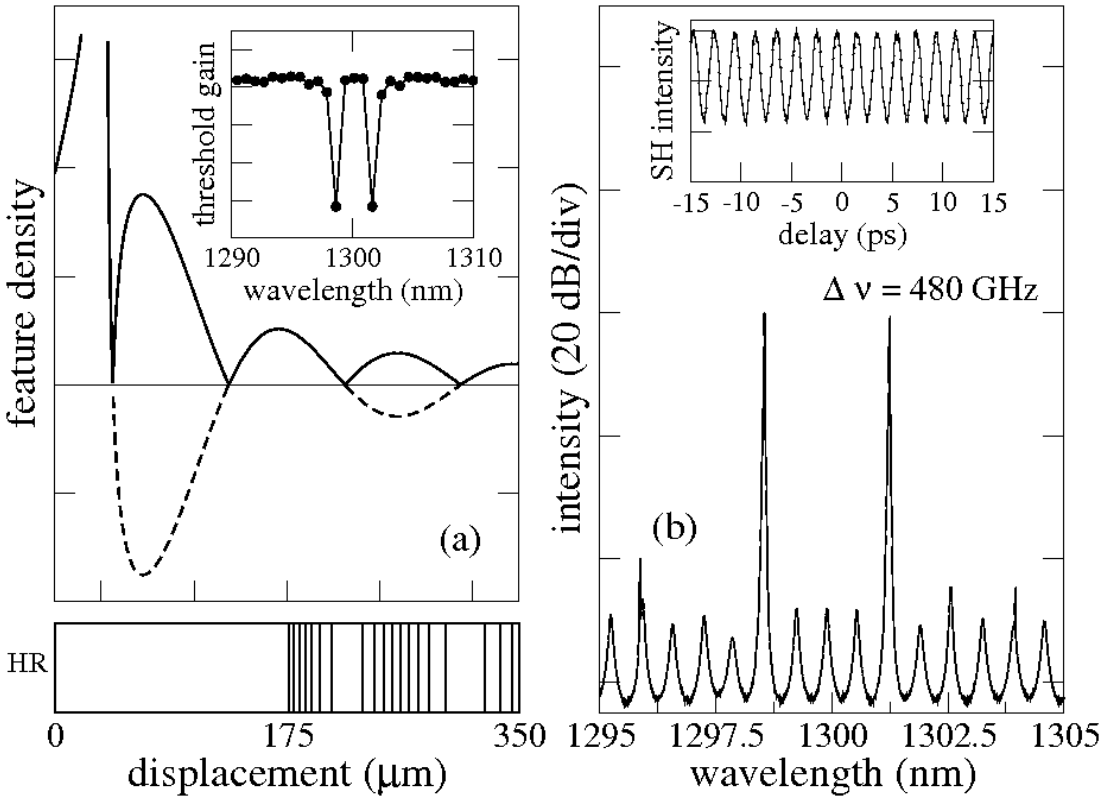

Figure 3.1: (a) Feature density function (solid line). Inset: Calculation of the threshold gain of modes for the laser cavity schematically pictured in the lower panel of the figure. Lower panel: Laser cavity schematic indicating the locations of the additional index step features. In the fabricated devices considered, these features are slotted regions etched into the ridge waveguide of the laser. The device is high-reflection (HR) coated as indicated. (b) Optical spectrum of the device at a device current of 43.5 mA (two-colour point). Inset: Background free intensity autocorrelation measurement showing mode beating at 480 GHz.

3.1.2 Chaos in optically injected dual-mode devices

It is well known that the single-mode semiconductor laser with optical injection exhibits a variety of complex dynamical behaviours including chaos [57, 58]. The single mode injected system is accurately modelled in a three-dimensional phase space that describes the intensity and phase dynamics of the injected mode and the carrier density.

Colleagues have extended these studies to the dual-mode case, and they found that

following a conventional period doubling route to chaos in the injected mode of the device, a further transition to a chaotic dual-mode state can be observed. With the addition of the second primary mode to the model equations, the single-mode injected system becomes an invariant sub-manifold of the larger dual-mode system, with the carrier density variable providing the coupling to the intensity of the uninjected primary mode. They showed that the chaotic dual-mode state in the injected system was an example of on-off intermittency. The characteristic behaviour associated with these dynamics is shown in Fig. 3.2.

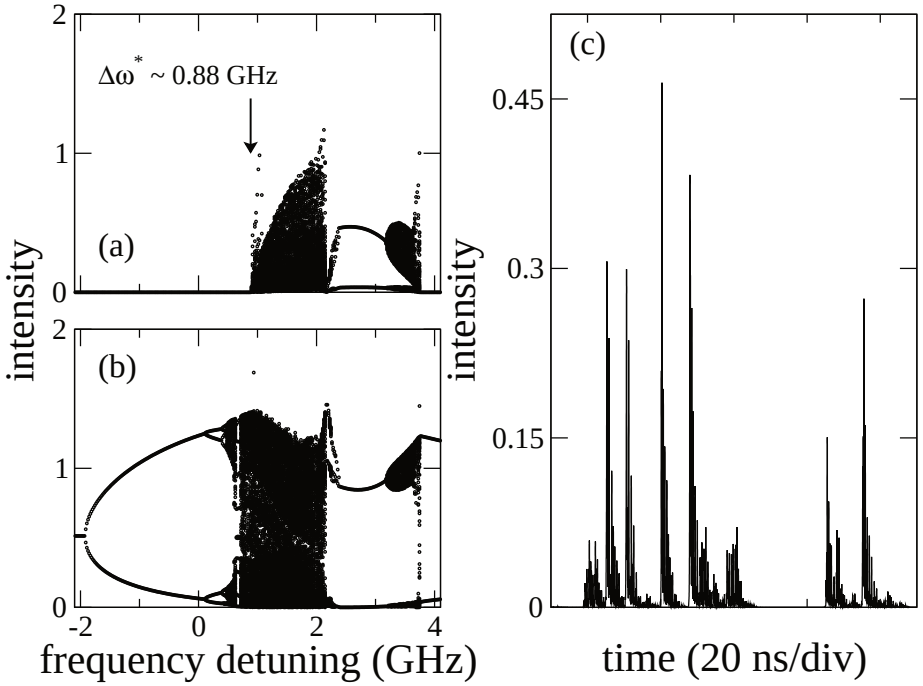

Figure 3.2: Left panels: Local extrema of the field intensities (a) $|E_1|^2$ and (b) $|E_2|^2$ obtained from numerical integration of Eqs. (1)–(3) as a function of the detuning. The injected field strength is K = 0.008. Right panel: Numerical time traces of the dynamics of the uninjected mode. The frequency detuning is 0.89 GHz. The injected field strength is the same as in (a).

In Fig. 3.2 (left panels) we plot the local extrema of the numerically calculated field intensities, $|E_1|^2$ and $|E_2|^2$, as a function of the frequency detuning in the injected dual-mode system. To locate this region of dynamics in the global bifurcation picture, see [38]. On the left of the diagram at negative frequency detuning we find an equilibrium region of stable injection locking where the uninjected mode is off. As the detuning is increased toward zero, a Hopf bifurcation occurs, and we enter the unstable locking region. Further increasing the detuning, a series of period doubling bifurcations are encountered before the dynamics of the injected mode become chaotic [56]. Over this detuning range the uninjected mode remains off. However, at a point inside the chaotic

region, we find that the uninjected mode turns on and that its intensity envelope increases smoothly at first. The value of the detuning where the uninjected mode turns on is approximately 0.88 GHz, which we label as $\Delta\omega^*$.

In the right hand panel of Fig. 3.2 the intensity is switching on to large values in a quasi-random manner, and these bursts of activity can be separated by long periods where the intensity is very small. This is the characteristic behaviour associated with on-off intermittency and matches closely the dynamics found in the injection experiment presented in [56].

The transition to on-off intermittency occurs when the chaotic attractor located in the three dimensional single mode submanifold loses transverse stability and the system enters a two mode-state. We find that the intensity of the uninjected primary mode takes on small values, remaining close to zero for long periods before being interrupted by bursting dynamics at irregular intervals. In our study of two-section dual-mode devices to be presented in this chapter and the next we will find that period doubling routes to chaos and loss of transverse stability of invariant sub-manifolds also play an important role in organising the dynamics in dual-mode two-section devices.

3.2 Experimental measurements of antiphase self-pulsations in a two-section semiconductor laser

For our experiments in this section, the device we consider is a multi-quantum well Indium Phosphide based ridge-waveguide Fabry-Pérot laser with one high-reflection (HR) coated mirror. The total device length is 545 μm with a saturable absorber section of length 30 μm adjacent to the HR mirror. Figure 3.3 shows the optical spectrum of one of these dual mode device at 16.3°C. This figure was obtained by applying a reverse bias of 0 V to the absorbing section of the device and varying the pump current in the gain section from 30 to 100 mA. The device has a peak gain at approximately 1549 nm, with the two primary device modes near 1546 nm and 1550 nm. As was the case with our previous examples, slotted regions etched in the ridge of the laser cavity define a spectral filter, which selects these two modes, with a primary mode spacing of six modes, or 480 GHz. The short and long wavelength modes are labeled ν_1 and ν_2 respectively. The device exhibits good modal selectivity, with the intensity output of the two primary modes at least 20 dB stronger than any of the others in the active region. The device reaches threshold on the long wavelength mode (ν_2) close to 35 mA. The short wavelength mode (ν_1) becomes active shortly thereafter, beginning to lase just before 40 mA. As the pump current is further increased, ν_1 begins to dominate the spectrum. The intensity output gradually transitions from long to short wavelength over a range of approximately 30 mA, up to a pump current just below 70 mA. Throughout the transition both modes are spectrally broadened. The

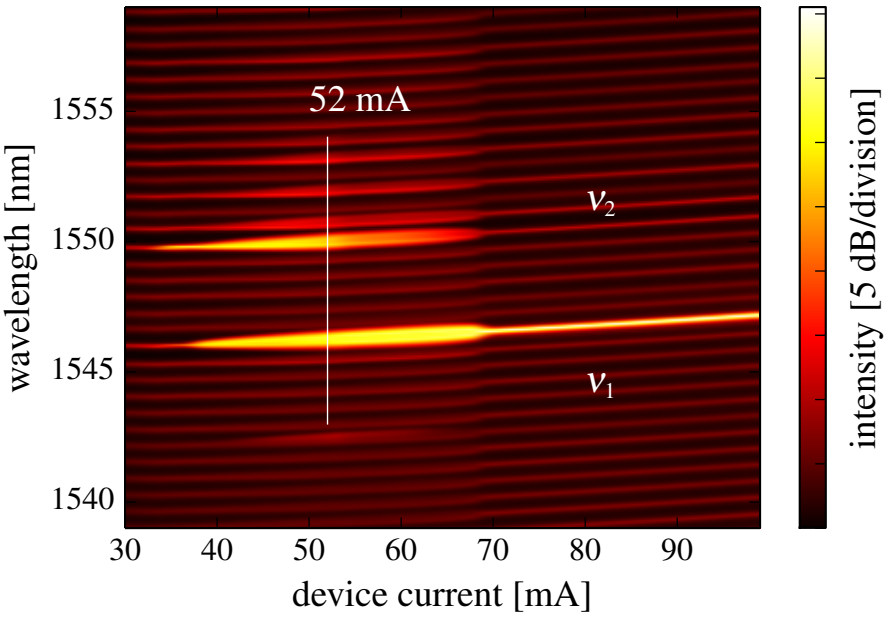

Figure 3.3: Optical spectrum of the dual-mode device for a range of pump currents. The bias applied to the absorber is 0 V. The short and long wavelength modes are labelled ν_1 and ν_2 respectively. For these measurements the device was mounted on a copper block with the temperature stabilised at 16.3°C.

intensity output of ν_2 is significantly diminished after 60 mA and by 70 mA almost all of the intensity is output on the short wavelength.

A measurement of the time trace of the total intensity and spectrally resolved measurements of the dynamics of the individual coupled modes are shown in Fig. 3.4. Here, the optical spectrum shows a significant reduction in the optical power in ν_2. These measurements were not taken simultaneously, but a device pump current of 52 mA and 0 V reverse bias in the absorber section was maintained in all cases. An overall intensity time trace was taken, subsequently the two primary modes were then isolated with intensity time traces taken in each case. The time trace of the total intensity shows an SP signal with a large amplitude modulation on a nanosecond timescale. Interestingly, the intensity of the pulses in the total intensity trace is almost uniform with only small variations from pulse to pulse. Despite the majority of the time trace in Fig. 3.4 (a) appearing to be a regular SP orbit, there are brief intervals where the pulse train breaks down. We can identify several large *drop outs* in the overall intensity time trace, where the peak intensity is momentarily significantly weakened, resulting in a relatively large overall intensity modulation over the course of two or three periods of the underlying SP orbit.

The time trace of Fig. 3.4 (b) shows the isolated intensity output of the long wavelength mode (ν_2). In this trace there is a much weaker average intensity, and an irregular pulsed intensity output with highly variable amplitude. Some of the pulses are of a

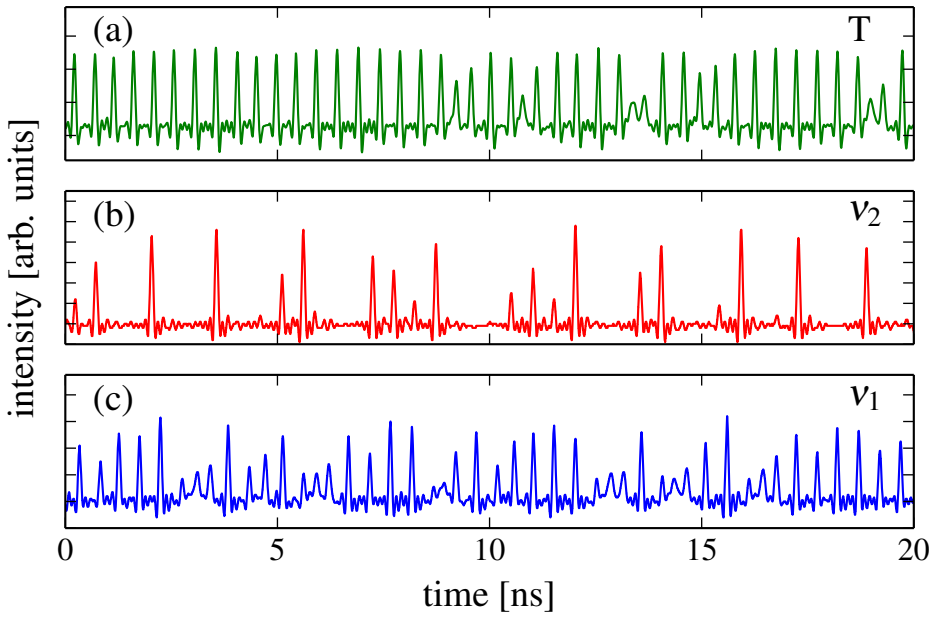

Figure 3.4: (a) Measured time trace of the total intensity for a device current of 52 mA. (b) and (c) Mode resolved time traces (ν_2 and ν_1 respectively) for a current of 52 mA in the gain section with reverse bias voltage of 0 V in the saturable absorber section. Measurements taken with a device temperature of 16.3°C.

sufficient amplitude that they appear to correspond to the total intensity, in which case the dynamics have become almost single mode. Moving to the trace in Fig. 3.4 (c) of the short wavelength mode (ν_1), we see a trace that is broadly similar to the total intensity. However, the drop outs here are more frequent, and the overall intensity is also reduced.

By comparing these figures and the structure of each time trace, we can see that the irregular broadened pulses from the total intensity trace seem to correspond to moments when the intensity switches between the long and short wavelength modes. Fig. 3.5 displays power spectra obtained for a reverse bias voltage of 0 V and a series of gain currents. In the total intensity power spectra of Fig. 3.5 (a) we immediately identify the main branch of SP dynamics increasing in frequency across the full range of the current in the gain section. The initial frequency of the branch is close to 1 GHz at 35 mA, increasing to just over 4 GHz at a current of 68 mA. After the SP region the device enters a continuous-wave (CW) state.

We next consider the power spectral data from the short wavelength mode as shown in Fig. 3.5 (c). Starting from a large pump current and moving toward threshold, over a small interval of pump current values we clearly see a spectral feature corresponding to the relaxation-oscillation (RO) frequency that remains essentially constant. In this region the output intensity is entirely on the short wavelength mode, as the laser is in a single mode regime.

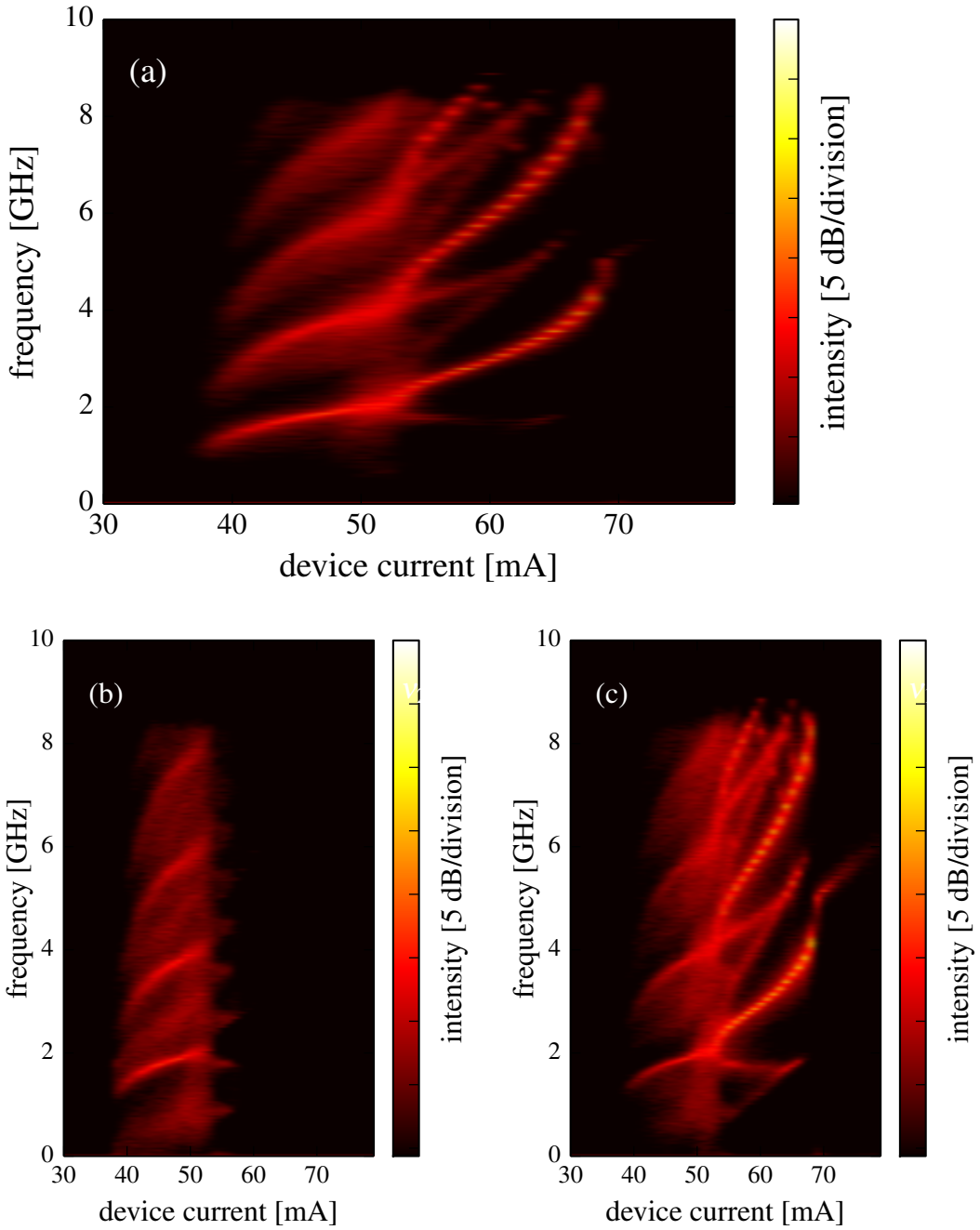

Figure 3.5: (a) Power spectrum of total intensity for a range of device currents. (b) and (c) Power spectra of the long (ν_2) and short (ν_1) wavelength primary modes. The bias applied to the absorber section in all cases is 0 V.

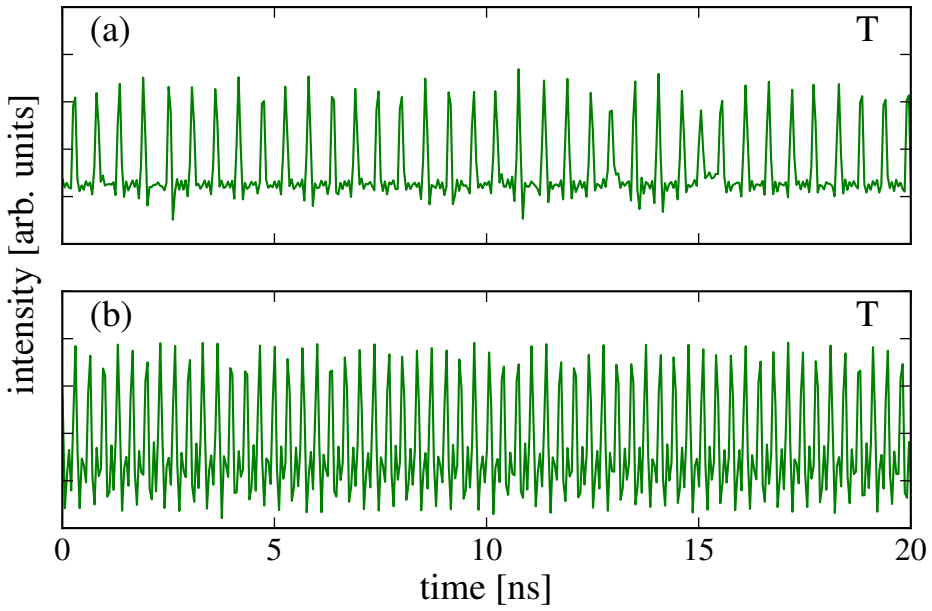

Figure 3.6: (a) Total intensity time traces for (a) 45 mA and (b) 60 mA in the gain section with reverse bias voltage of 0 V across the saturable absorber section.

Once the device enters the SP region below 70 mA, the variation in the primary frequency component begins to vary much more dramatically. This frequency decreases relatively rapidly, and at a pump current of 65 mA we see a period doubling bifurcation, where a new spectral feature appears at a value of one-half of the frequency on the primary branch around 3.5 GHz. The spectral feature corresponding to the period doubled branch then splits into two sub-branches. The upper of the these two sub-branches then collides with the primary branch and we enter a region where the spectrum becomes significantly broadened, and at a pump current of 55 mA, we can argue that the power spectrum is essentially continuous.

This period doubling is not visible in the power spectrum of ν_2 in Fig. 3.5 (b), although we regard this as being due to a weak signal intensity, that was not sufficient to register in our experimental apparatus. Evidence for this conclusion is provided by the weak signal in the single mode continuous wave region above 68 mA, where we see a signature of relaxation oscillations that is not present in the power spectrum of the total intensity. This suggests that the second mode is in fact active in this region so that these dynamics are in antiphase and do not therefore appear in the total output. Further evidence in support of our conclusion that these are dual-mode dynamics is provided by our numerical work presented in the previous chapter, where we find no evidence for a single mode state with these characteristics

It is worth noting that there is less low frequency structure visible in the power spectrum of the total intensity when compared with the mode resolved power spectra of Fig. 3.5

(b) and (c). This suggests the presence of antiphase dynamics throughout the region where the power spectral of the individual modes are broadened.

Further time traces of the total intensity taken from before and after the region of the almost continuous power spectrum at 52 mA are shown in Fig. 3.6. These traces highlight the increasing frequency of the underlying SP orbit as the current density in the gain section is increased. Fig. 3.6 shows the total intensity time trace at 45 mA, where the frequency and amplitude of the intensity dropouts are both reduced. In Fig. 3.6 (b), taken at a device current of 60 mA, the system is in the period doubled state. The dynamics in this state are quite regular, despite the fact that the underlying characteristic time-scale of the SP orbit has increased significantly. In this example one can clearly see the weak contribution from ν_2 visible between the large ν_1 pulsations.

3.3 Modelling of the device response

Modelling the dynamics of our experimental system while treating each mode individually is complicated by the relatively large number of independent parameters that will be necessary to characterise the response of the gain and absorber sections of the device [28, 49]. However, colleagues have successfully modelled the dynamics of dual-mode devices with optical injection and feedback in past work [38, 46], and the LSA model provides a guide for extending these models to the case of a two-section laser.

In physical units the multimode extension of the LSA system Eq. 2.22 reads:

$$\begin{aligned} \dot{S}_m &= [(1-\rho)\tilde{G}_m(N_g) + \rho\tilde{Q}_m(N_q) - \gamma_m]S_m \\ \dot{N}_g &= j - \frac{N_g}{\tau_s} - \sum_m \tilde{G}_m(N_g)S_m \\ \dot{N}_q &= \quad -\frac{N_q}{\tau_q} - \sum_m \tilde{Q}_m(N_q)S_m. \end{aligned} \tag{3.1}$$

Here S_m is the photon density of mode m. N_g and N_q are the carrier densities in the gain and absorber sections respectively. As before, the ratio of the absorber section length to the total device length is given by ρ. The total field losses of each mode are $\gamma_m = \alpha_{\text{mir}} + \alpha_{\text{int}} + \alpha_{\text{f}}^m$, where α_{mir} are the mirror losses and α_{int} are the internal losses assumed constant for all modes. Additional losses, α_{f}^m, due to the action of the spectral filter are also included. In the previous chapter the consideration of these additional losses was unnecessary as only a single mode was considered and the gain profile could be accurately described without the requirement for an additional degree of freedom. Once again, the current density in the gain section is j, while the carrier lifetimes in the gain and absorber sections are τ_s and τ_q respectively.

Typical profiles of the gain and absorption spectra in multimode semiconductor laser

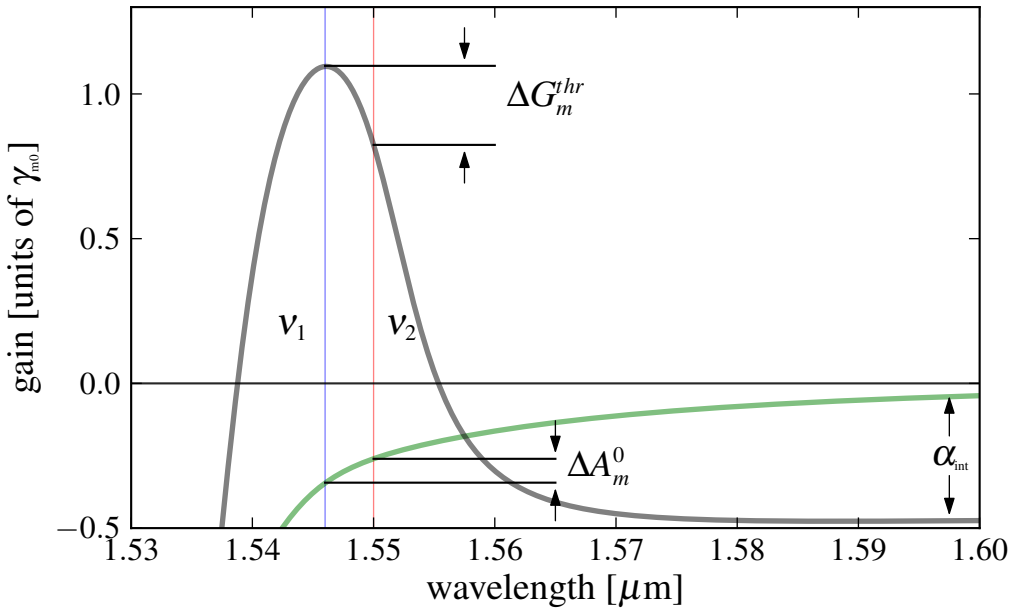

Figure 3.7: Schematic diagram of the material gain and absorption in a typical semiconductor laser. The locations of the two primary modes of the device ν_1 and ν_2 are indicated. The model parameters that describe the dispersion of the modal gain and absorption are also highlighted.

of the kind we consider are shown in Fig. 3.7. As before, the negative offset of the gain function at long-wavelength gives an estimate of the background losses, α_{int}. Here we have schematically indicated the locations of the two primary modes of the laser. We first fix a reference carrier density value, N_g^{thr}, in order to define the dispersion of the gain profile for our model. We take this reference value to be the threshold carrier density for the device assuming a transparent absorber section, and define the mode with the largest material gain at this carrier density as our reference mode, m_0. The threshold carrier density defines a reference value for the modal gain: $\tilde{G}_{m_0}(N_g^{\text{thr}}) = (1-\rho)^{-1}\gamma_{m_0}$, and a set of modal differential gain values, $\tilde{g}_{gm}$. The gain function for each mode can then be linearised around the reference value of the carrier density so that $\tilde{G}_m(N_g) = \tilde{G}_m(N_g^{\text{thr}}) + \tilde{g}_{gm}(N_g - N_g^{\text{thr}})$. Dispersion in the modal absorption is included by defining $\tilde{Q}_m(N_q) = \tilde{g}_{qm}N_q - Q_m^0$, where the differential absorption is $\tilde{g}_{qm}$, and unsaturated losses for each mode, Q_m^0, will be determined by the applied voltage. Once again, the modal absorption is thus defined with respect to the unsaturated (zero field) value.

To derive normalised equations, as in the previous chapter we rescale time in units of the photon decay rate of a plain FP cavity without spectral filtering: $\gamma = \alpha_{\text{mir}} + \alpha_{\text{int}}$. We define the normalised pump current, $p = (j - j_{\text{thr}})/j_{\text{thr}} \equiv j_s - 1$, where $j_{\text{thr}} = N_g^{\text{thr}}/\tau_s$, and we define the normalised carrier densities in each section of the device: $n_g = (N_g - N_g^{\text{thr}})/N_g^{\text{thr}}$ and $n_q = (N_0 - N_q)/N_g^{\text{thr}}$, where $N_0 = Q_{m_0}^0/\tilde{g}_{qm_0}$. In normalised units

the equations then read

$$\begin{aligned} \dot{I}_m &= [(1-\rho)G_m(n_g) + \rho Q_m(n_q) - \gamma_m^{'}]I_m \\ T\dot{n}_g &= p - n_g - \sum_m G_m(n_g)I_m \\ T\dot{n}_q &= \Delta(q_0 - n_q) + \sum_m Q_m(n_q)I_m \end{aligned} \tag{3.2}$$

where $q_0 = \frac{N_0}{N_g^{\text{thr}}}$, $T = \gamma\tau_s$, and $\Delta = \tau_s/\tau_q$. In these equations the normalised gain functions are

$$G_m(n_g) = G_m(n_g^{\text{thr}}) + g_{gm}N_g^{\text{thr}}n_g$$

where $G_m(n_g^{\text{thr}}) = \gamma^{-1}\tilde{G}_{m_0}^{\text{thr}} + \Delta G_m^{\text{thr}}$, $\gamma_m^{'} = \gamma_m/\gamma$, and $g_{gm} = \tilde{g}_{gm}/\gamma$. Here $\Delta G_m^{\text{thr}} \equiv \gamma^{-1}(\tilde{G}_m^{\text{thr}} - \tilde{G}_{m_0}^{\text{thr}})$ describes the dispersion of the reference linear gain profile. The normalised modal absorption functions are

$$Q(n_q) = -g_{qm}N_g^{\text{thr}}n_q + (g_{qm} - g_{qm_0})N_0 - \gamma^{-1}\Delta Q_m^0$$

where $g_{qm} = \tilde{g}_{qm}/\gamma$, and $\Delta Q_m^0 = Q_m^0 - Q_{m_0}^0$.

Note that the normalised carrier density in the absorber section is defined so that the modal absorption is linearised around the saturated value for the reference mode. The phase space of system (3.2) contains two invariant three dimensional sub-manifolds, defined by $I_m = 0$, for $m = \{1, 2\}$. The dynamics on each of these sub-manifolds reduces to the single-mode LSA system, and for this reason we will refer to these sub-manifolds as the single-mode manifolds of the system. Based on previous estimates obtained for similar devices [37], we take the carrier lifetime in the gain section, τ_s = 1 ns. The mirror losses of the device are calculated to be $\alpha_m = 13.8$ cm^{-1}, and we estimate the internal losses to be $\alpha_{\text{int}} = 9.2$ cm^{-1}. These losses determine the cavity decay rate for the plain FP laser to be $\gamma = 2 \times 10^{11}$ s^{-1}, and $T \simeq 200$.

In order to define the losses due to spectral filtering and to fix the value of N_g^{thr}, we compare our results with threshold data from a plain two-section FP laser from Chapter 2. With a uniform current density over the full device length, the threshold current of the FP laser was 13.5 mA. With zero volts applied to the absorber section, the threshold increased to 17 mA, with the peak emission at 1557.5 nm. The scale of N_g is defined so that the differential gain at threshold for the single-section FP is equal to one in normalised units. We therefore set N_g^{thr} equal to 2.2 based on estimates of the increase in the carrier density necessary to reach the defined threshold level at the wavelength of the reference mode.

3.4 Bifurcations of a dual-mode laser with saturable absorption: Case of small Δ

As we have discussed, the carrier lifetime in the absorber section can be much shorter than in the gain section, with a strong dependence on the applied bias [51]. Following the results of Chapter 2, we fix the carrier lifetime in the absorber section so that $\Delta = 3$. In order to complete the model we must specify the values of the linear gain, unsaturated absorption, and the differential gain and absorption for each primary mode of the device. Because of the large size of this parameter space, we begin by considering the dynamics of two coupled modes with similar parameters. Guided by the known dispersive properties of the semiconductor susceptibility, and by the observed behaviour of the device, we then make a series of further adjustments to these parameters until we have obtained satisfactory agreement with measured data.

For our numerical simulations, the parameters describing the gain function at the position of the reference mode, ν_1, are fixed. To begin we assume a flat gain and absorption curve and we examine the effects of dispersion in the differential gain and absorption on the dynamics of the coupled system. From Fig. 3.3 we see that in our experiment the device begins to lase with constant intensity output on the long wavelength mode, before entering a region of SP. With equal linear gain and unsaturated absorption, the mode with the largest differential gain will reach threshold first. On the other hand, a larger differential absorption will mean that a mode will saturate its losses more quickly above threshold and thereby dominate at larger pump values. To reproduce this behaviour, we set the differential gain and absorption in normalised units of mode ν_1 to be 1.0 and $0.8\rho^{-1}$ respectively. The ratio of these quantities for mode ν_1 is then $s_1 \equiv g_{q1}/g_{g1} = 14.5$. We set the differential gain and absorption of ν_2 to be 1.4 and $0.6\rho^{-1}$ respectively so that $s_2 = 7.8$. The remaining parameters values we choose to begin are $A^0_{[1,2]} = 0.6\gamma$ and $\Delta G^{\text{thr}}_{m[1,2]} = 0$. Note that the differential gain in normalised units is likely to be less than unity given the higher current density at threshold in the dual-mode device. We have decided not to make this correction in order to make a comparison of the various model parameters more transparent. We have also confirmed that our results are largely independent of the precise values chosen for this parameter.

Table 3.1: Parameters describing the gain and absorption for Figures 3.8 - 3.11.

	ν_1	ν_2
g_{gj}	1.0	1.4
$g_{qj}\rho^{-1}$	0.8	0.6
$A^0_{\text{j}}\gamma^{-1}$	0.6	0.6
$\Delta G^{thr}_{\text{mj}}\gamma$	0	0

Our chosen parameters are summarised in Table 3.1 and are consistent with the ob-

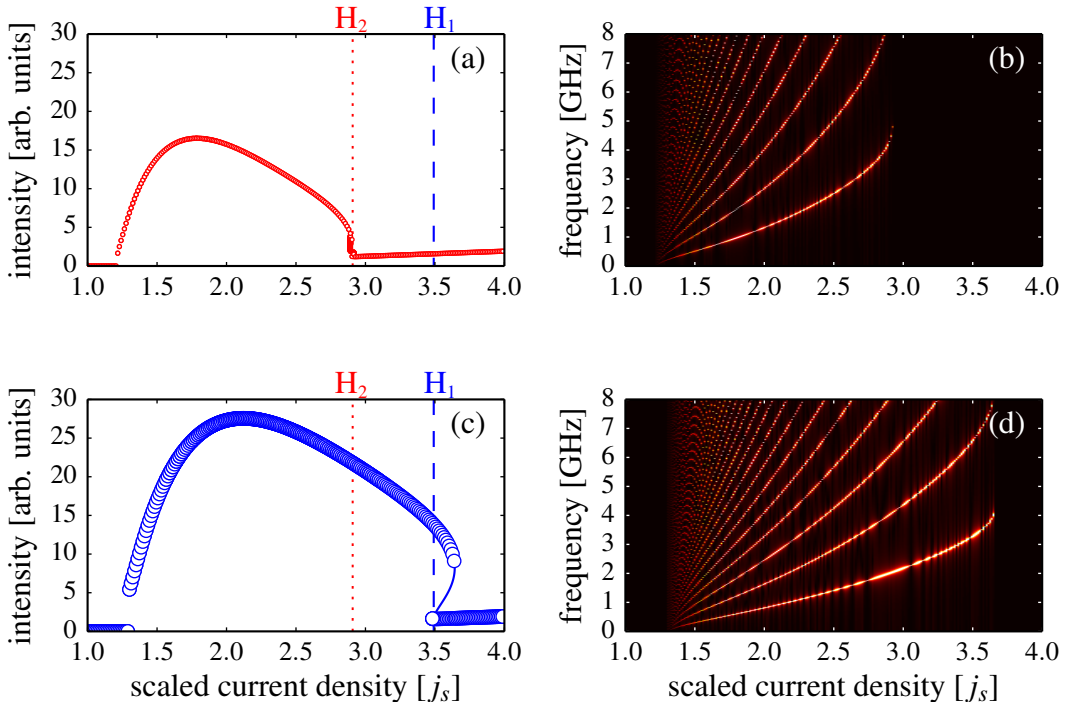

Figure 3.8: (a) Single mode simulation for parameters in Table 3.1 of the output intensity of ν_2. (b) Power spectral density for ν_2 in single mode system. (c) Single mode simulation for parameters in Table 3.1 of the output intensity of ν_1. (d) Power spectral density for ν_2 in single mode system. These simulations are all the result of both an upward sweep in the device current density. The Hopf bifurcations at large pump current for each of the modes are labelled H_2 and H_1 in red and blue respectively.

servation of a narrow region of constant output at threshold in our experiment. The underlying structure of the steady-state solutions is identical to the structure discussed in Chapter 2. We will find that the stability of the single-mode steady-states plays a fundamental role in organising the dynamics in our device, and we will therefore present numerical bifurcation diagrams for each of the single-mode solutions of our model as we vary the model parameters for each mode. We note that the measured increase in threshold of the dual-mode device, the placement of the spectral filter and the large separation between the selected modes are all factors that suggest large unsaturated absorption and enhanced dispersion of the model parameters.

Numerical bifurcation diagrams and intensity power spectra obtained using the parameters presented in Table 3.1 are shown in Figs. 3.8 and 3.9. Figs. 3.8 (a) and (b) describe the dynamics of both of the primary modes restricted to their respective single mode manifolds, obtained by setting the intensity of the inactive mode to zero for the time evolution of Eqn. (3.2). In Fig. 3.8 (a) the threshold behaviour of ν_2 is similar to the long wavelength mode in our experiment, with a region of constant output found after the zero field solution becomes unstable. The threshold behaviour of ν_1 is similar to that of Fig. 2.9 (e), where no stable steady states are available at threshold. The single mode threshold behaviour of the short wavelength mode is not experimentally significant

however, as the dual-mode system reaches threshold on the long wavelength mode. Following threshold, both modes then enter a region of SP, with the SP region bounded in each case by a Hopf bifurcation at larger pump current. In Fig. 3.8, dashed lines labelled H_1 and H_2 indicate the second Hopf bifurcation points that bound the SP region at larger pump values for each mode.

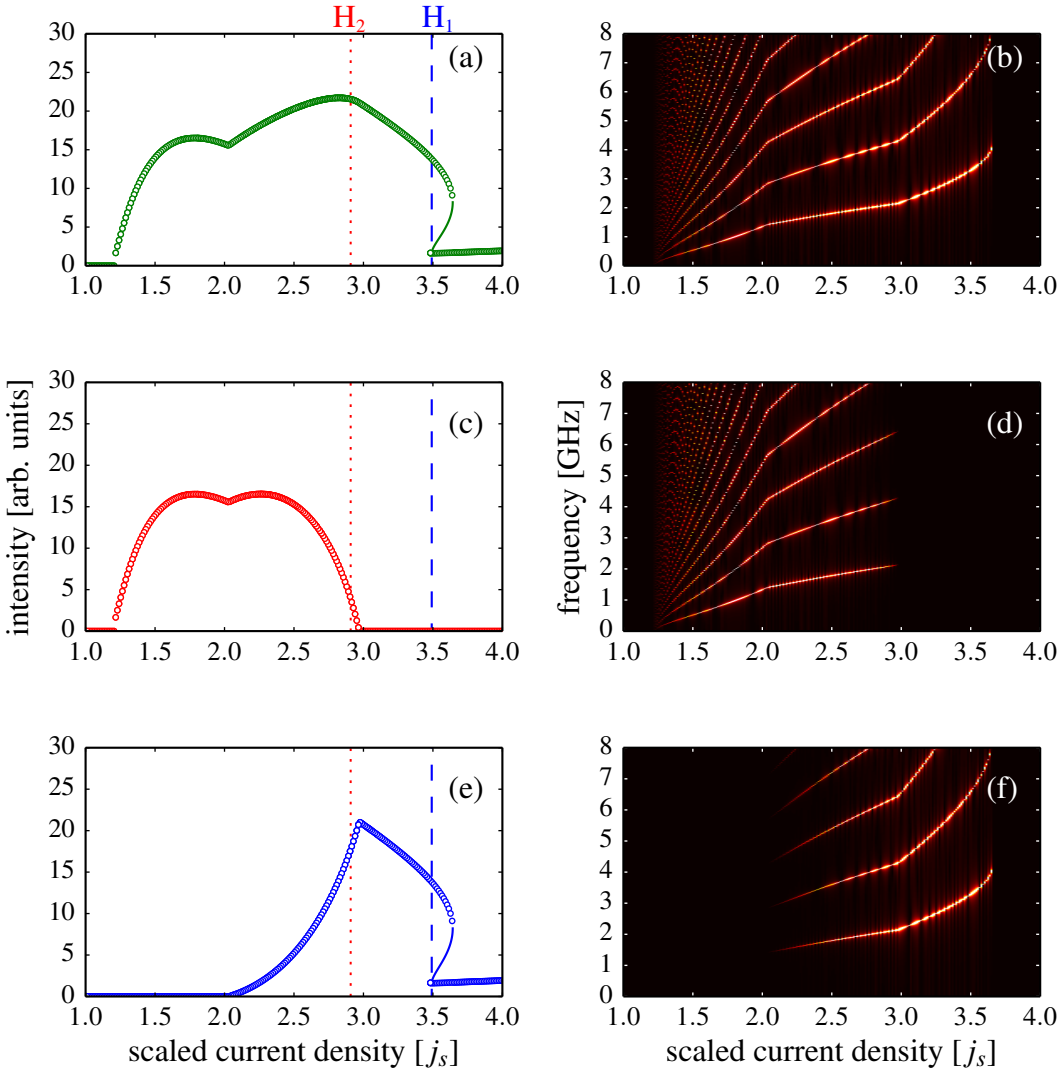

Figure 3.9: Simulations of the coupled system for parameters in Table 3.1. Left panels: simulated bifurcation diagrams. Right panels: Power spectral densities. (a) and (b): Total field. (c) and (d) Long wavelength mode ν_2. (e) and (f): Short wavelength mode ν_1. These simulations are all the result of both an upward sweep in the device current density. The Hopf bifurcations at large pump current for each of the modes are labelled H_2 and H_1 in red and blue respectively.

Mode resolved numerical bifurcation diagrams and power spectra for the two modes in the full coupled mode system are shown in Fig. 3.9. Chosen parameters ensure that the long wavelength mode reaches threshold first, and because the second mode is initially suppressed, mode ν_2 reproduces the dynamics found in the single mode system. However, before the region of single mode SP ends at the second Hopf bifurcation

shown in Fig. 3.8 (a), the dynamics become dual-mode, with the SP intensity gradually switching across to the shorter wavelength mode ν_1 as the pump is increased further. This dual-mode region comes to an end shortly after a pump value of $j_s = 3$ where the system enters a region of single mode SP on ν_1. The region of SP dynamics finally ends at the subcritical Hopf bifurcation of ν_1, and the dynamics switch to constant output in mode ν_1 for large values of the pump current.

The dual-mode region, beginning just after a pump current of $j_s = 2$ commences at a frequency of 1.5 GHz, which corresponds to the ν_2 single mode value. The single mode frequency of ν_1 however, is close to half this value, which is clear from Fig. 3.8 (b), where the fundamental frequency of ν_2 closely tracks the first harmonic of ν_1. By the end of the dual-mode region at $j_s = 3$ the frequency of the dual-mode system is 2.2 GHz, which now reflects the frequency of the single mode value of ν_1. It is worth noting that the end of the dual-mode region occurs at a pump current larger that the single mode Hopf bifurcation of ν_2. This dual-mode region involves a synchronisation of the fundamental SP frequencies for each of the modes. The increase and decrease of the single mode SP frequencies of modes ν_1 and ν_2 respectively leads to an "agreed" common frequency.

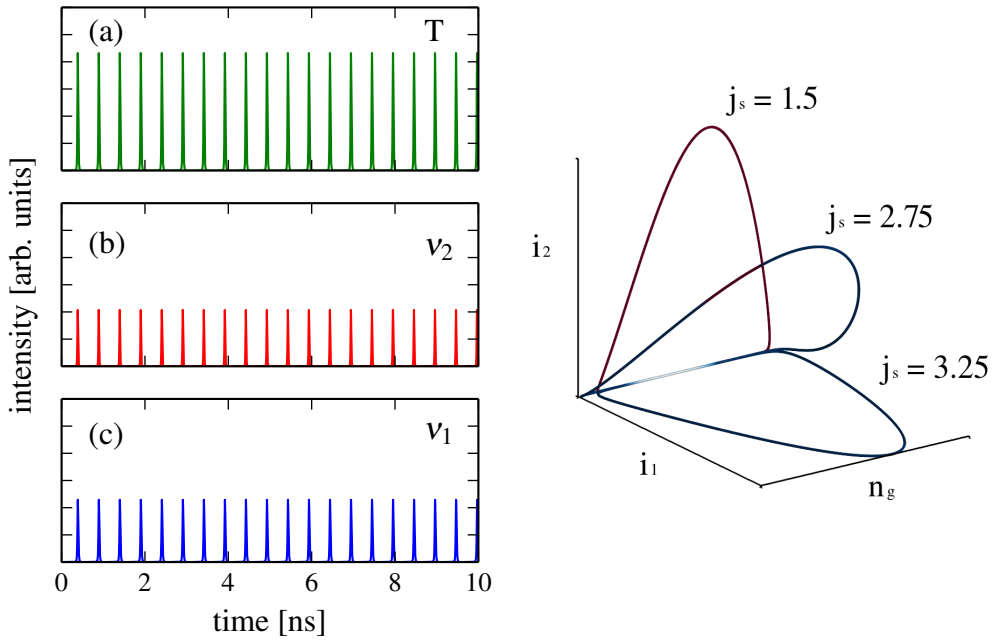

Figure 3.10: Left: Simulated time traces of the total intensity (upper panel), and of the individual modes (centre and lower panels). The pump current value is $j_s = 2.75$. Right: Phase space diagrams for three values of the pump current as shown. Parameters are as in Table 3.1.

If we compare the numerical variation of the SP frequency with our experiment, we see that the measured SP frequency appears with a large value of c. 1.5 GHz, and that it then remains relatively constant. Our simulations therefore underestimate the SP frequency at onset, and we overestimate its rate of increase. One can also see that the

extent of the SP region that we find numerically is much larger than the measured value. While the measured variation of the SP frequency may be partly due to an uncharacteristic behaviour of our device, it should be noted that we cannot expect to obtain quantitative agreement with experiment using the LSA model. We have already confirmed this conclusion with our comparison of the results of numerical simulations made using the LSA model and the delay-differential model of [29] presented in Chapter 2. Using experimentally calibrated parameters appropriate to a self-pulsating FP laser, in Chapter 2 we found that the LSA model will in general predict a far larger SP region, with a larger SP frequency than the delay-differential model. In addition, while we can adjust unknown parameters such as the absorber recovery time to match numerical and experimental results in the case of the delay-differential model, it is in general more difficult to reconcile experiment with the predictions of the LSA model. This comparison emphasises the importance of not assuming small gain and loss when building quantitative models of two-section semiconductor lasers.

Time traces taken from the centre of the dual-mode region with $j_s = 2.75$ are shown in the left panel of Fig. 3.10, while the right hand panel of Fig. 3.10 shows a phase space representation of the dynamics for three pump values, taken before, during and after the transition from ν_2 to ν_1. We see that the intensity shifts continuously from one mode to the other through a region of in-phase SP. As expected, the gradual transition of the dynamics from ν_2 to ν_1 that we observe in these simulations leads to agreement with the experimental measurements of Fig. 3.3 near threshold and at large values of the pump.

In order to better understand the bifurcation structure of Fig. 3.9 we can look at the geometry in the $p - \Delta$ plane. In Chapter 2 we studied the single mode manifolds of the LSA systems in this plane. Fig. 3.11 shows both dual and single mode bifurcations of ν_1 and ν_2 for the parameters of Table 3.1. Here, with both modes represented we use a color scheme which reflects the nature of the bifurcations. The blue and red lines denote bifurcations of ν_1 and ν_2 respectively, which also occur in the single mode manifold. The green lines represent bifurcations of dual mode states. Bifurcations are labeled using the following notation: SN (saddle node), HB (Hopf) and TC (transcritical). We focus on the dashed horizontal line at $\Delta = 3$, which was used in Figs. 3.8 and 3.9. Following this line from small pump current, the first bifurcation which we can observe experimentally is the transcritical bifurcation of ν_2, followed closely by a Hopf bifurcation of the same mode. As discussed in relation to Fig. 3.9, the next bifurcation occurs when the dynamics become dual-mode, with the SP intensity gradually switching across to ν_1. This switch begins and ends with transcritical bifurcations into and out of the dual-mode state. The final bifurcation in this sequence is the sub critical bifurcation of ν_1, whereupon the system enters a CW state with all of the output intensity on the short wavelength mode.

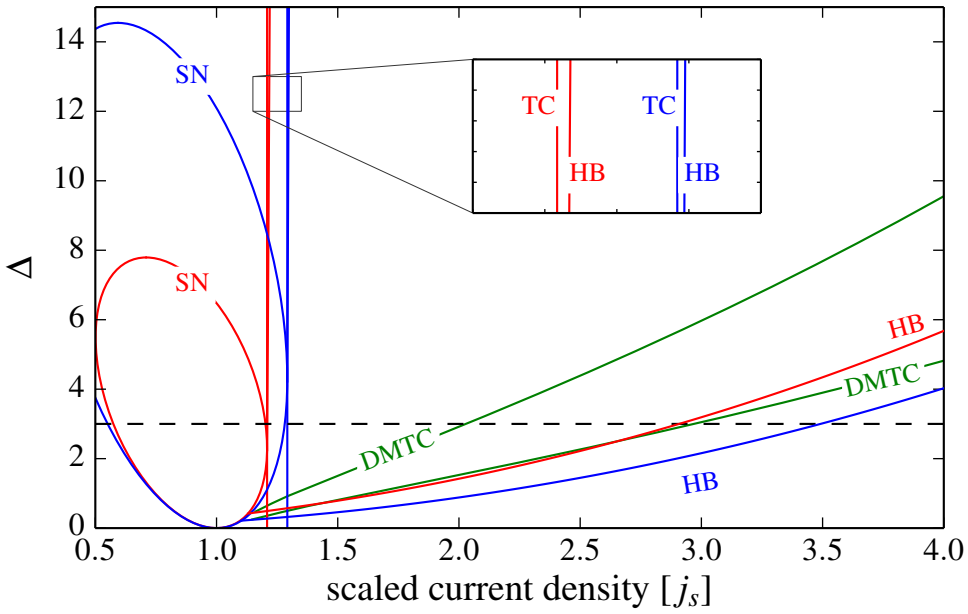

Figure 3.11: Bifurcation diagram in the j_s vs. Δ plane of Eqn. (3.2) calculated using the numerical continuation tool AUTO-07p with for the parameters in Table 3.1. Blue and red lines denote bifurcations of single mode states ν_1 and ν_2 respectively. Bifurcations of dual-mode states are shown in green. The different lines of bifurcations are indicated by SN (saddle node), HB (Hopf), TC (transcritical), DMTC (dual mode transcritical)

Table 3.2: Parameters describing the gain and absorption for Figures 3.12 & 3.13.

	ν_1	ν_2
g_{gj}	1.0	1.4
$g_{qj}\rho^{-1}$	1.0	0.6
$A_j^0\gamma^{-1}$	0.6	0.5
$\Delta G_{mj}^{thr}\gamma$	0	0

For our first example in this chapter, we chose a set of parameters with flat linear gain and unsaturated absorption. We adjusted the differential gain and absorption to set up the experimentally observed transition from ν_2 to ν_1 on the basis of the knowledge gained from our study of the single mode system in Chapter 2. However, as shown in the schematic of the gain and absorption of Fig. 3.7, the linear gain and absorption of each mode has the potential to be markedly different. Here we choose differences in these quantities that can represent a typical dual mode device as suggested in Fig. 3.7. The short wavelength mode, ν_1, is given a slightly larger unsaturated absorption to reflect the increased absorption moving away from the absorber section band-edge. We also increase the differential absorption of the short wavelength mode, which is consistent with its location further from the band-edge. The parameters chosen for our next example are shown in Table 3.2. The integrated bifurcation diagrams with these parameters are shown in Figs. 3.12 and 3.13.

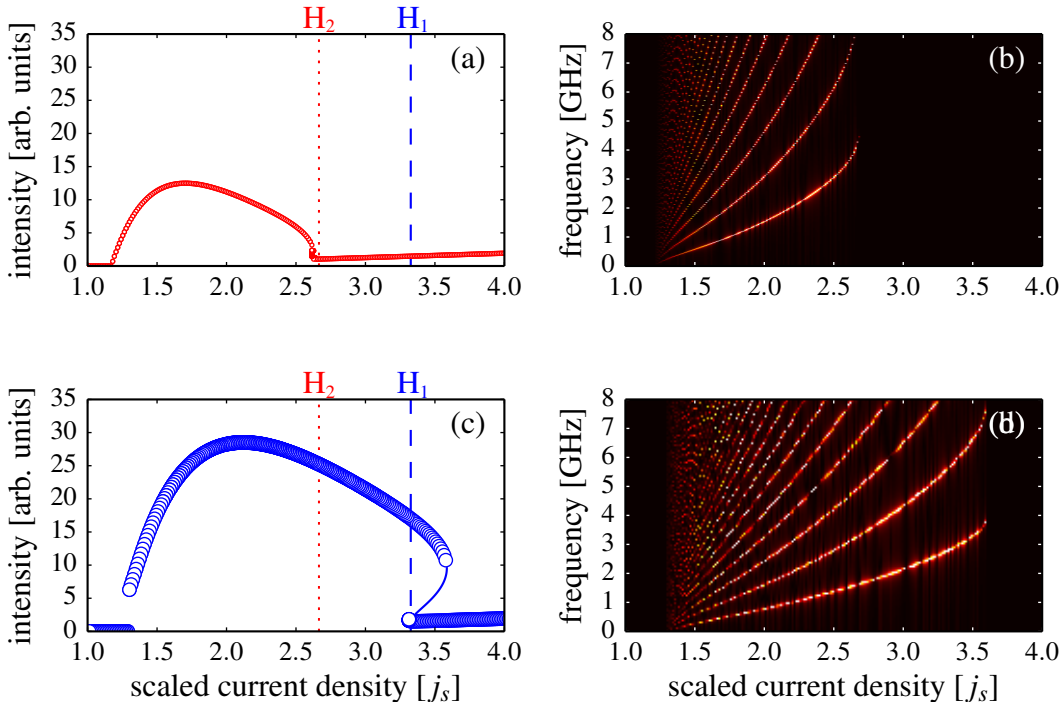

Figure 3.12: (a) Single mode simulation for parameters in Table 3.2 of the output intensity of ν_2. (b) Power spectral density for ν_2 in single mode system. (c) Single mode simulation for parameters in Table 3.2 of the output intensity of ν_1. (d) Power spectral density for ν_2 in single mode system. These simulations are all the result of both an upward sweep in the device current density. The Hopf bifurcations at large pump current for each of the modes are labelled H_2 and H_1 in red and blue respectively.

For the short wavelength mode, the net effect of the increase in differential absorption is that the Hopf bifurcation at large pump current is moved to a slightly smaller pump current value, bringing it closer to the device threshold. In the single mode power spectra shown in Fig. 3.12 (b), we see that the fundamental SP frequency of ν_2 has increased, becoming much closer to the second harmonic of the SP frequency of ν_1. With these changes, in the coupled system shown in Fig. 3.13 we find that a pair of period doublings occur on the dual-mode SP limit cycle. The dual-mode region in this case is larger than before, extending from $j_s = 2$ to $j_s = 3$, and the coupled state beginning at $j_s = 2$ undergoes a period-doubling at 2.3 units of pump current. The appearance of this state in the power spectra of Figs. 3.13 (b),(d) and (f) bears comparison with what we identified as a period doubling in our experimental power spectra of Fig. 3.5. Although the fundamental frequency of the period doubled state is less than half that of the experimentally observed state, it seems as though the same mechanism is playing a role in both cases. In our numerical simulation there is only a single pair of period doublings whereas the experimental results seem to show a cascade of period doublings, particularly when entering the state from large pump current.

By further adjustment of the parameters from Table 3.2 we decrease the linear gain of

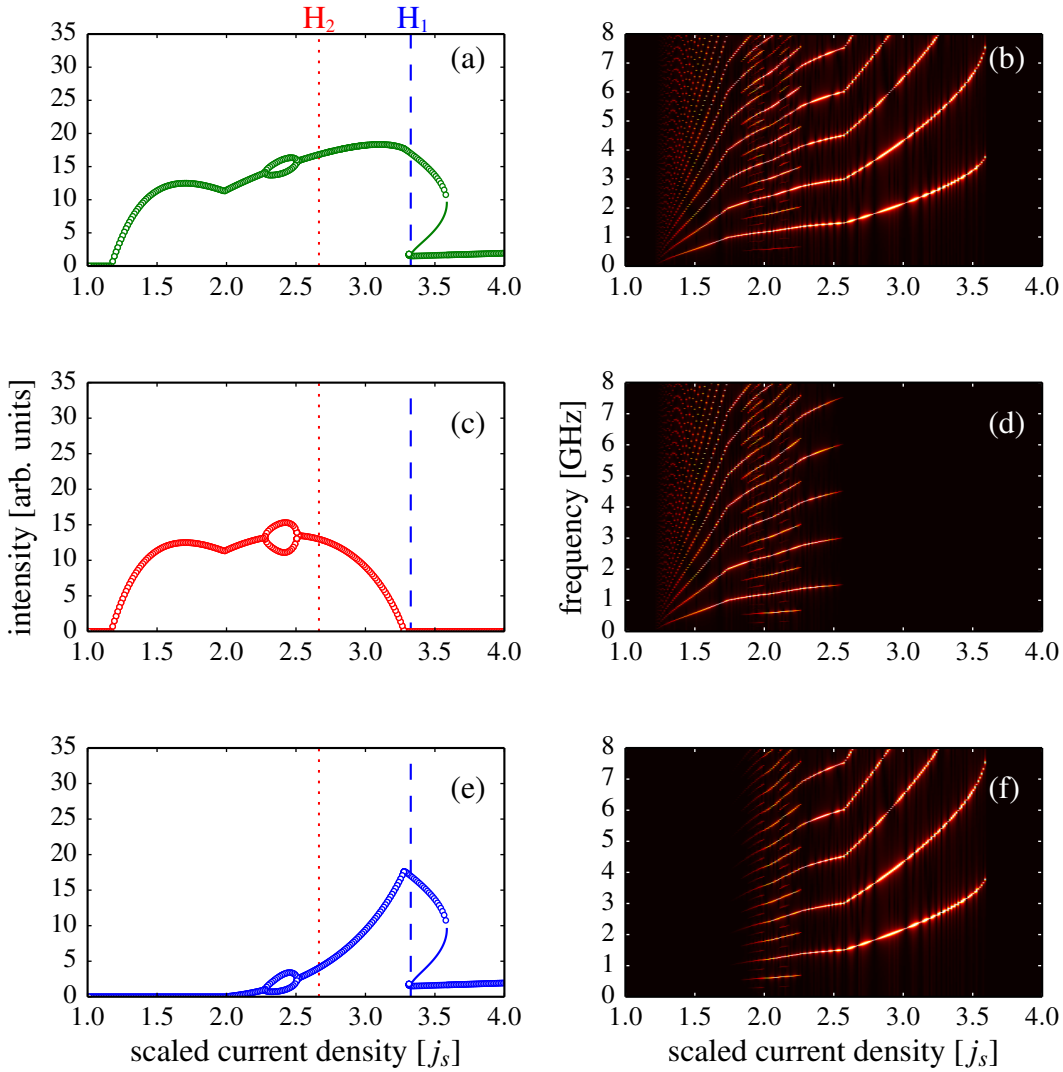

Figure 3.13: Simulations of the coupled system for parameters in Table 3.2. Left panels: simulated bifurcation diagrams. Right panels: Power spectral densities. (a) and (b): Total field. (c) and (d) Long wavelength mode ν_2. (e) and (f): Short wavelength mode ν_1.

ν_2 relative to ν_1. We make this change to reflect the curvature of the gain peak away from its peak near the short wavelength mode, as reflected in the schematic of Fig. 3.7. We also further increase the differential absorption of ν_1, which is also consistent with the dispersion illustrated in Fig. 3.7. This has the effect of moving the location of the Hopf bifurcation at large pump current closer to the device threshold and to the large pump current Hopf bifurcation of ν_2. The effects of our changes are shown in Figs. 3.14 and 3.15, which were obtained using the complete set of parameters shown in Table 3.3. In Fig. 3.14 we can see that the large pump current Hopf bifurcations of both modes are now much closer together.

We have noted and shown in the example of Fig. 3.9 the importance of the ability of both coupled modes to be able to agree on a common SP frequency. This ability leads

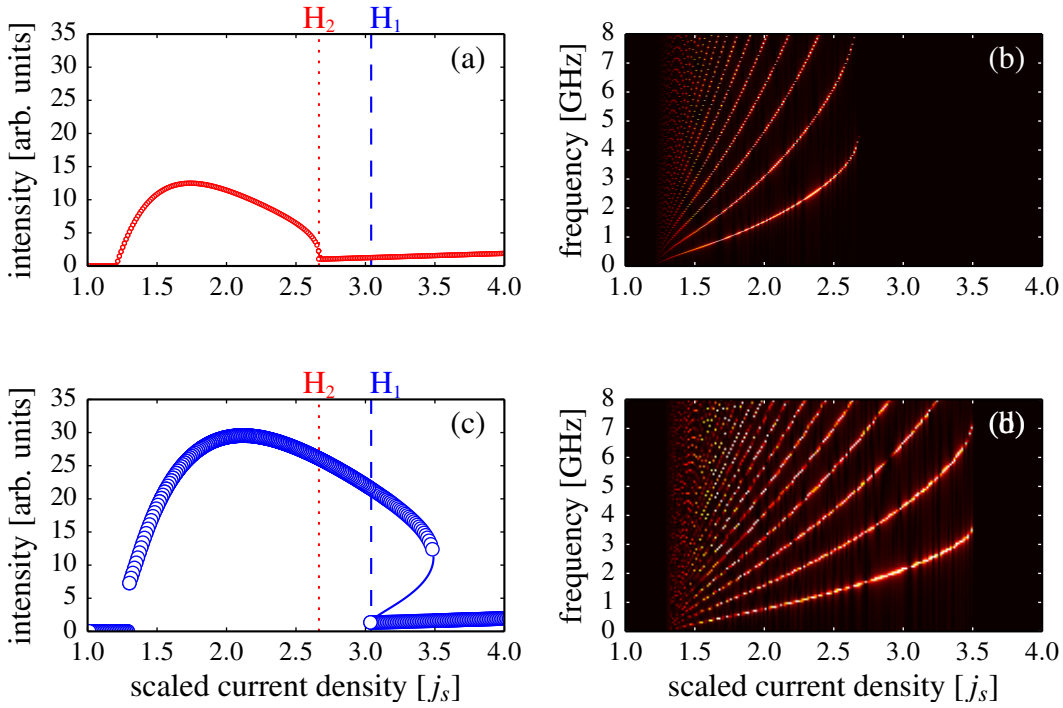

Figure 3.14: (a) Single mode simulation for parameters in Table 3.3 of the output intensity of ν_2. (b) Power spectral density for ν_2 in single mode system. (c) Single mode simulation for parameters in Table 3.3 of the output intensity of ν_1. (d) Power spectral density for ν_2 in single mode system. These simulations are all the result of both an upward sweep in the device current density. The Hopf bifurcations at large pump current for each of the modes are labelled H_2 and H_1 in red and blue respectively.

to a single continuous region of dual-mode SPs where the modes oscillate in phase. With further adjustment of parameters we found in Fig. 3.13 that the region of dual-mode SPs is no longer continuous, but instead a pair of period doubling bifurcations occur along the dual-mode SP branch. In this case a lower frequency appears in the system, and we can interpret this phenomenon as resulting from the inability of the two interacting modes to agree on a single shared oscillation frequency over the whole region of dual-mode SPs.

The dynamics of the dual-mode system that we find with the parameters of Table 3.3 are shown in Fig. 3.15. Here, we find that as a consequence of the further increase in the dispersion of the gain and absorption the simple SP or period doubled dynamics give way to a much more complex dynamics where, for example, there is evidence for a continuum of frequencies being present in the numerical power spectral data of the individual modes and of the total intensity.

Although these numerical results are by no means in complete agreement with our experimental results, several aspects of this numerical bifurcation picture closely resemble aspects of the experimental results in Figs. 3.3, 3.4 and 3.5. This approximate correspondence allows us to suspect that some of the same physical factors and mechanisms

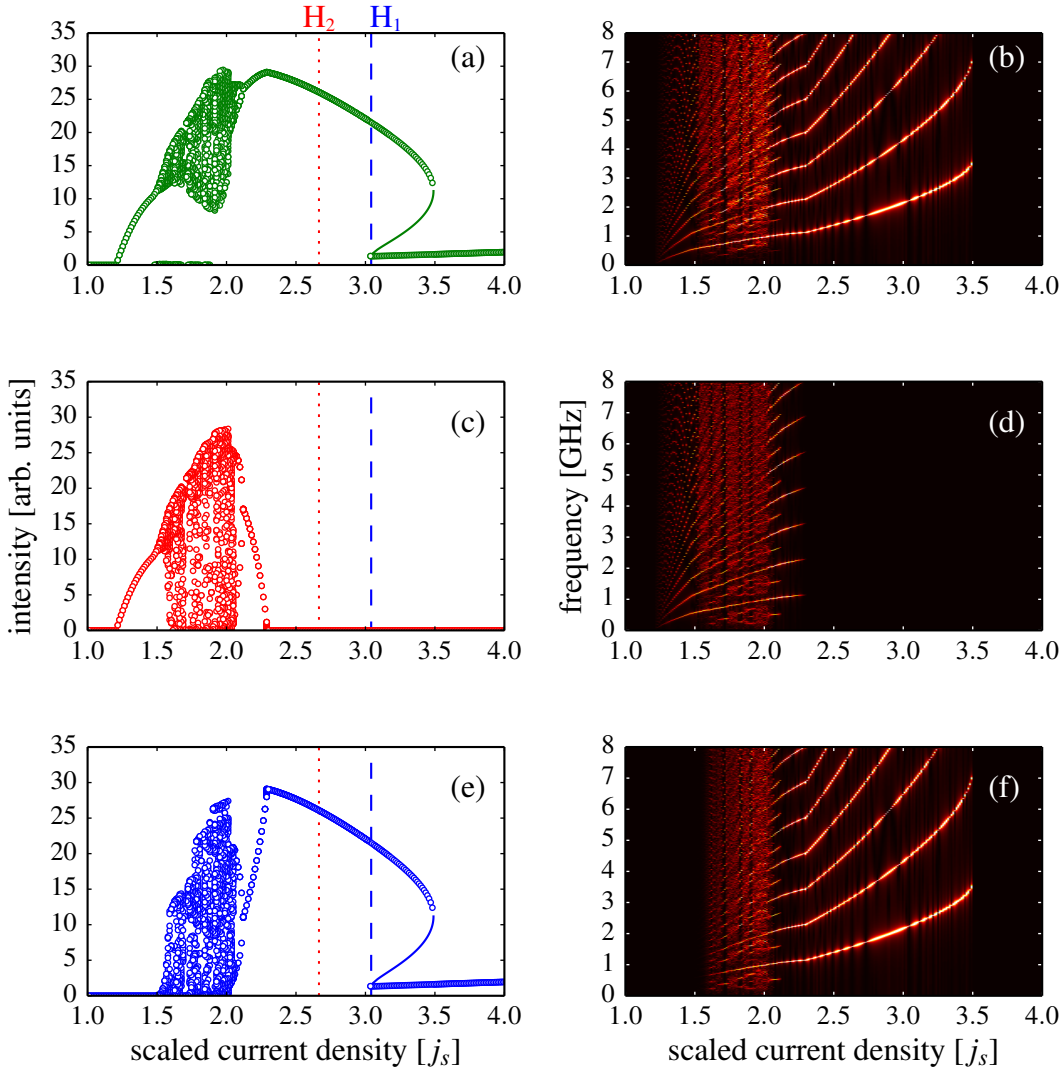

Figure 3.15: Simulations of the coupled system for parameters in Table 3.3. Left panels: simulated bifurcation diagrams. Right panels: Power spectral densities. (a) and (b): Total field. (c) and (d) Long wavelength mode ν_2. (e) and (f): Short wavelength mode ν_1.

Table 3.3: Parameters describing the gain and absorption for Figures 3.14 - 3.19.

	ν_1	ν_2
g_{gj}	1.0	1.4
$g_{qj}\rho^{-1}$	1.4	0.6
$A_{\mathrm{j}}^{0}\gamma^{-1}$	0.6	0.5
$\Delta G_{\mathrm{mj}}^{thr}\gamma$	0	-2.5

are at play.

We first note that as the pump current is reduced from a large value the device enters a dual-mode SP state and then a period doubling bifurcation occurs in a similar way to the dynamics observed in Fig. 3.13. As the pump current is decreased further however, the sequence of bifurcations is radically different, and we find instead a series of densely spaced transitions into progressively more complex behaviour. To assist with interpretation of these numerical results in the context of our experimentally measured data, we can examine the structure of the intensity time traces and power spectra throughout the region.

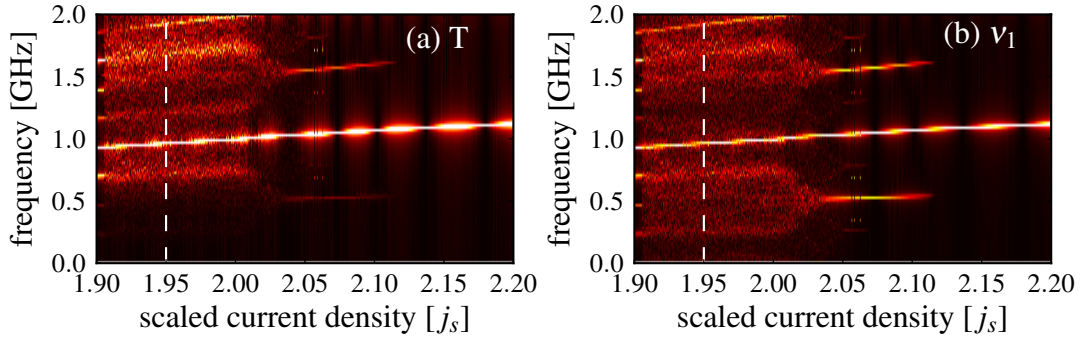

Figure 3.16: Zooms of power spectra from Fig. 3.15 (b) and (e). Left panel: Total. Right panel: ν_1. The dashed vertical line in both cases is at $j_s = 1.95$. Other parameters are as in Table 3.3.

We can first observe that many of the more complex aspects of the dynamics have antiphase character. For example, the maxima and minima determined by the turning points in the total intensity as shown in Fig. 3.15 (a) have a very different distribution to those of the individual modes. The turning points in the individual modes are distributed continuously, whereas there is a large region at intermediate intensities where the total intensity does not display any turning points.

In addition, evidence for an interpretation of these dynamics as resulting from a complete loss of the ability of the system of coupled modes to synchronise is evidenced in Fig. 3.15 (a). Here we see that in the region of period doublings there are signatures of turning points in the total intensity output near zero intensity. Close examination of the structure of the intensity time traces shows that this signature is caused by the timing of the pulses in each individual mode's intensity drifting out of step with each other. This is a fundamental difference with the previous examples where we found that pulses are synchronised in the time domain, including in the region of period doubled dynamics.

Fig. 3.16 shows a detailed closeup of the numerical power spectral data from the period doubling region in Figs. 3.15 (b) and (e). Here we can very see clearly the antiphase nature of the dynamics, with the low frequency component almost completely absent from the total power spectrum as in Fig. 3.5. The power spectrum of ν_1 appears to be

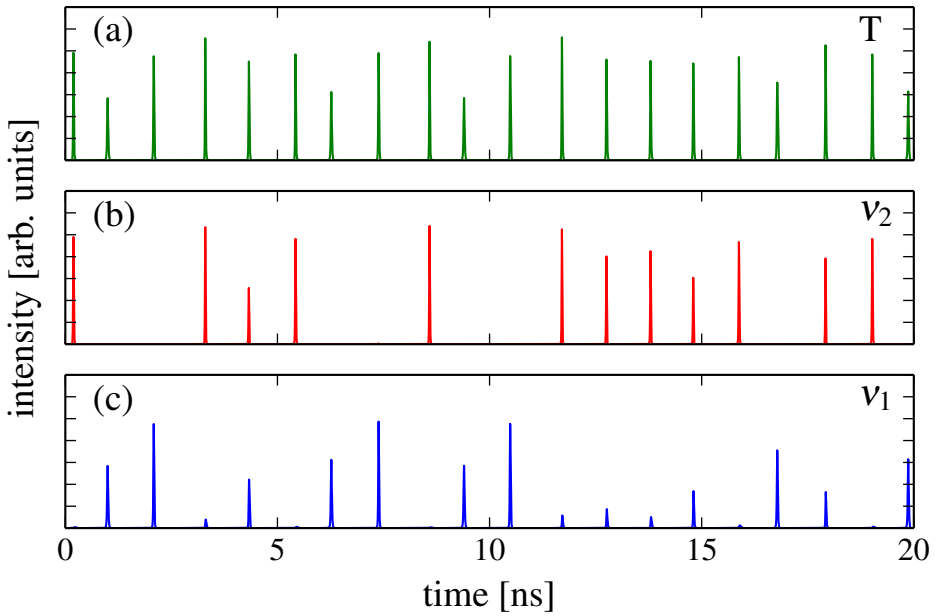

Figure 3.17: Simulated time traces of the total intensity (upper panel), and of the individual modes (centre and lower panels). The pump current value is $j_s = 1.95$. Other parameters are as in Table 3.3.

continuous after a series of period doublings, which strongly indicates the presence of chaos.

Fig. 3.17 shows an example of mode resolved intensity time traces from within the period doubling region at $j_s = 1.95$. Comparing Fig. 3.17 with the experimental result of Fig. 3.4 we can see that the fundamental frequency of the numerical simulation is approximately half that of the experiment. We can see that the peaks in the numerical total intensity output are more variable when compared with the experiment results, and it is less clear which of the two modes is dominant in the numerical data. However, there is clearly a considerable degree of agreement between this result and the experimental results of Fig. 3.4.

Fig. 3.18 shows a phase space diagram of the time traces shown in Fig. 3.17. In this representation we can see that most of pulses with a variety of amplitudes remain close to the single mode manifold of either ν_1 or ν_2. However, there are several excursions into the dual-mode space, where the trajectories of the pulse are drawn away from the single mode manifolds. Fig. 3.19 shows the geometry of the relevant bifurcations in the $p - \Delta$ plane with the same colour scheme and labelling scheme as in Fig. 3.11 with the addition of PD (period doubling) bifurcations. Once again a dashed line at $\Delta = 3$ indicates the slice taken for our numerical simulations in Figs. 3.14 - 3.18. Here we can see the emergence of a bubble of period doubling bifurcations from $\Delta < 1$ which lie between the pair of dual-mode transcritical bifurcations.

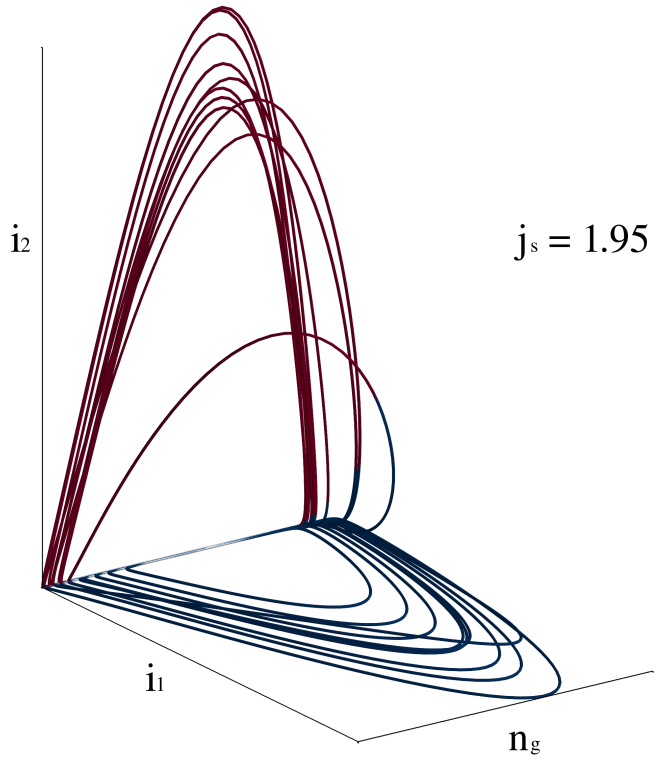

Figure 3.18: Phase space diagram of time traces for a pump current of $j_s = 1.95$. Parameters are as in Table 3.3.

There are further nested cascades of period doublings inside the bubble shown, but due to the large number of bifurcations and degeneracies at small values of Δ they are difficult to resolve. Figure 3.20 shows a zoom of the period doubling branch from Fig. 3.15, from which we can discern the first three period doublings with the naked eye. In this particular instance the cascade of period doublings proved too difficult to follow using numerical continuation methods. There are also a series of Bogdanov-Takens points at the intersection of the SN and HB lines which make the use of continuation tools difficult. However, in the same system with different parameters we were able to precisely locate the period doubling locations as far as the sixth branch point. In these cases we observed that the distance between successive period doublings closely followed the expected Feigenbaum scaling [59].

We note finally that the geometry of the bifurcations in the $p - \Delta$ phase space confirms our previous estimate of the experimental Δ value. The bubble of period doubling bifurcations is confined to lower values of Δ, and we have found that this is the case for a wide range of parameter values. It therefore seems that it would be difficult to

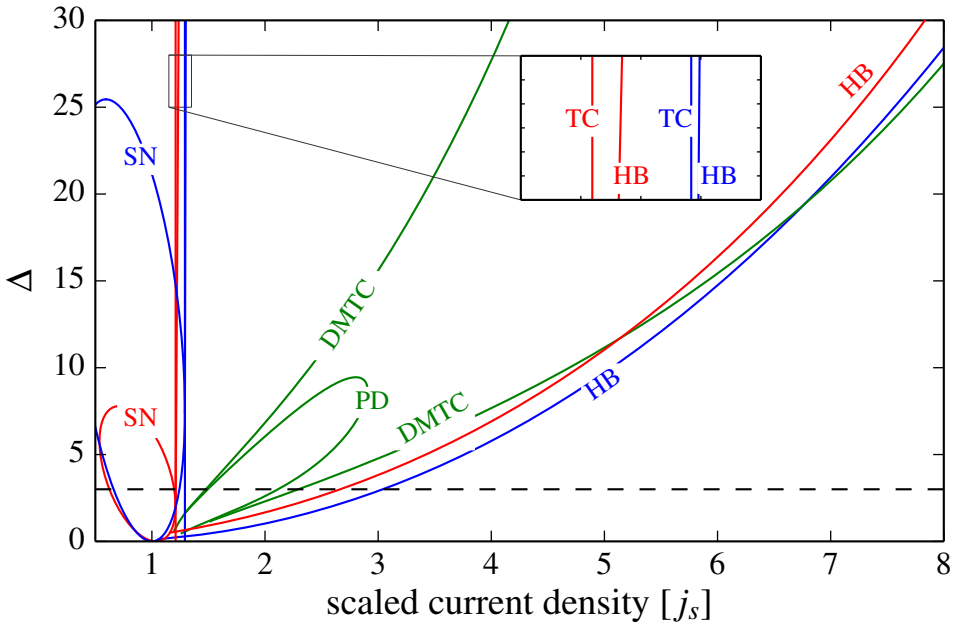

Figure 3.19: Bifurcation diagram in the j_s vs. Δ plane of Eqn. (3.2). Blue and red lines denote bifurcations of single mode states ν_1 and ν_2 respectively. Bifurcations of dual-mode states are shown in green. The different lines of bifurcations are indicated by SN (saddle node), HB (Hopf), TC (transcritical), DMTC (dual mode transcritical) and PD (period doubling). Parameters are as in Table 3.3.

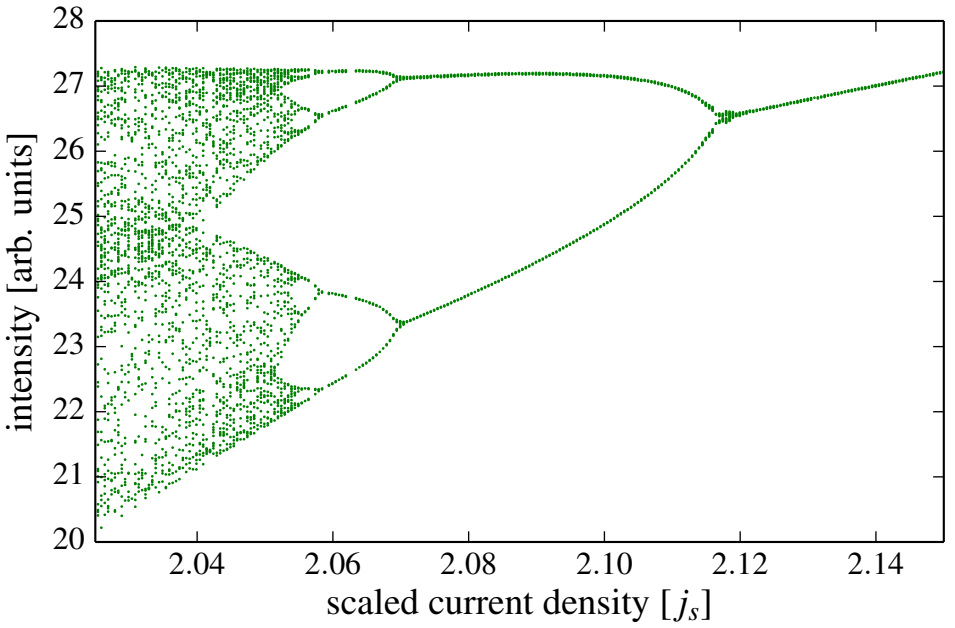

Figure 3.20: Zoom showing period doubling branches of the total intensity output from Fig. 3.15. Parameters are as in Table 3.3.

find the period doublings seen experimentally if the true value of Δ was considerably larger than the value we estimated in the previous chapter.

3.5 Conclusions

In these simulations we have successfully obtained some degree of qualitative agreement with experiment, but it is also clear our numerical model has some serious deficiencies in this case. For example, the frequency of the underlying SP orbit is about half that of the experimentally observed value, with a considerably larger variation in the overall intensity output. The power spectral data are also significantly different, and, in particular, the branching structure of the experimental power spectrum has not been fully reproduced. The continuous nature of the power spectrum of ν_1 after the series of period doublings suggests that the dynamics may be of a chaotic nature, although it is hard to say with certainty. In any event, it is also true that if the numerics shown here are not chaotic, the experimental results may still be. The work presented in this chapter therefore represents a first step towards developing a more complete understanding of the observed dynamics. However, certain key elements of the behaviour observed experimentally are present in the numerical simulations, and we have framed our discussion of the underlying physical mechanism in terms of synchronisation phenomena. We pointed to the significance of the intensity drop outs and phase slips as important signatures of loss of synchronisation in the coupled dual-mode system.

The numerical continuation tool that we employed here can be difficult to use in cases where the SP orbit closely approaches zero intensity as here. In particular, the large number of Bogdanov-Takens bifurcations (two on each of the single-mode manifolds) renders the system very prone to instabilities when attempting to follow branches of dynamics using these types of numerical tools.

We can imagine a number of possible alternatives that may allow us to obtain better agreement between modelling or numerical results and experiment. Making an explicit ansatz to represent the underlying periodic orbit could allow one to reduce the dimensionality of the problem, although this might be difficult in practice given the strongly non-sinusoidal nature of the dynamics. An alternative would be to represent the coupled dynamics in terms of a discrete mappings with coupling terms, which may allow one to study sychronisation phenomena in a much simplified framework. This approach has proven to be useful in systems with the characteristic separation of timescales and associated singular behaviour, so-called slow-fast systems [41], that we have considered here.

Chapter 4

Dual-mode dynamics: Time-reversed spiralling orbits

4.1 Introduction

In this chapter we continue our study of the dual-mode two-section system, but here we will consider a second device, which has a slightly different material dispersion at threshold. We will present experimental measurements where we have found that single mode self-pulsations evolve into a complex dynamical dual-mode state. In this state the total intensity experiences regular bursts of pulsations on a constant background. Spectrally resolved measurements will reveal that in this state the individual modes of the device can follow highly symmetric but oppositely directed spiralling orbits. We will also discuss the relationship between these states and the underlying SP dynamics of the system. Using the dual-mode generalisation of the rate equation description studied in Chapter 3, we will show that these orbits appear as a consequence of the interplay between the material dispersion in the gain and absorption sections of the laser.

As a consequence of the fabrication uncertainty associated with the manufacturing process, the spectral location of the primary modes and the filter implementation is slightly different from the device of the previous chapter. These uncertainties arise because of the cleaving process that defines the cavity length, but also from the etching process which can be over-etched leading to more lossy index-step features. Evidence that the particular set of dual-mode devices considered in this thesis have excess losses is provided by the optical spectrum in the dual-mode state, which displays some 10 dB less spectral purity than previous dual-mode examples. Any over-etching of the devices that would result in excess loss can lead to greater apparent material differences between nominally identical devices fabricated on the same wafer but

formed by distinct cleaving steps.

The result is that we find that a related but different set of parameters are appropriate for describing the dual-mode device considered in this chapter. For the purposes of developing our numerical simulations, we will use a similar method as in Chapter 3. With this approach, we will once more start with two similar modes and move through the parameter space guided by the observed experimental and numerical results. Here we will find a new sequence of dynamics as the pump current is varied and we will examine the Lyapunov stability of steady states of the system and discuss the role that transverse stability of single-mode states play in the bifurcation sequences observed.

The structure of this chapter is as follows: In order to motivate the discussion of self-pulsation dynamics to be presented, we will first discuss a novel example of dual-mode dynamics observed in a device with optical injection. As was the case in the previous chapter, we will find that the injected dual-mode system can display dynamical states and bifurcations that are closely related to those we have observed in our study of the dual-mode two-section device. We will then introduce our device and experimental setup, and we will present optical and mode resolved power spectra as well as a series of characteristic intensity time traces illustrating a progression to a region of complex dual-mode dynamics. We will then move on to simulating the experimental results numerically and uncovering the bifurcation structure of the system. Finally, we will reconcile the results of the last chapter with the dynamical sequence and bifurcation structure of the current chapter and offer a unified picture of the dynamical states of these devices.

4.1.1 Antiphase dynamics in a semiconductor laser with optical injection

Semiconductor laser systems subject to optical injection continue to receive considerable attention since their original discovery [60, 61]. These systems provide ideal test beds for testing understanding of fundamental concepts in nonlinear dynamics [43, 62]. In Figs. 4.1 and 4.2 we present previous work on optically injected dual-mode devices carried out by colleagues [38]. This same system was also discussed in the previous chapter in Section 3.1.2, and is characterised by the presence of a single three-dimensional invariant sub-manifold that contains the dynamics of the injected primary mode. Figure 4.1 presents experimental and numerical results obtained at a frequency detuning of 10 GHz, with injection at the long wavelength mode ν_2.

Figure 4.1 again highlights the excellent agreement between theory and experiment that was found in these dual-mode injection experiments. Note, for example, that the experimental and numerical frequency detunings are identical in each set of example time traces, and that we find a very close correspondence between the experimental and numerical data at the level of the frequency of the sawtooth style modulation

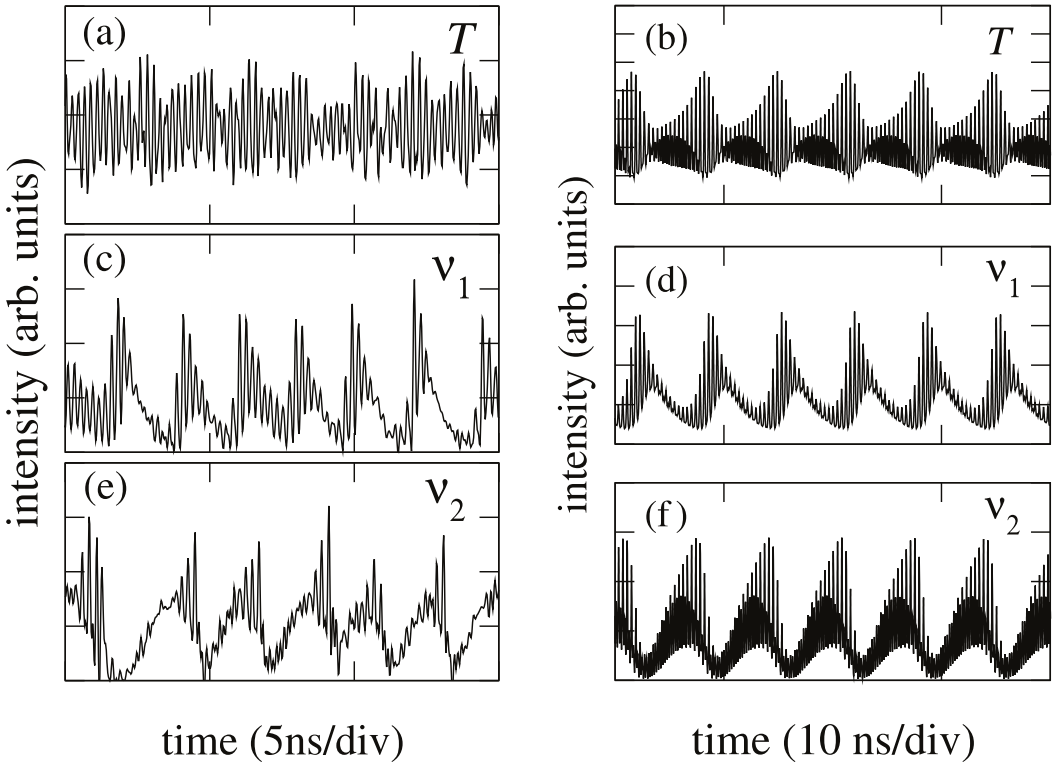

Figure 4.1: Experimental and Numerically computed intensity time traces, region (i). The frequency detuning is 10.0 GHz. The injected field strength is K $= 0.008$. (a) and (b): Total Intensity. (c) and (d): uninjected mode. (e) and (f): Injected mode.

envelope, with a frequency of c. 400 MHz, [38], and of the individual peaks that make up each of these "teeth".

What is notable about these traces is not only their sawtooth structure, but also the fact that the individual modes are tracing sawtooth patterns that are oppositely directed in time. In addition, these waveforms are strongly antiphased, as we can see that the total intensity is modulated around a constant background level, while the envelopes of the individual modes are modulated close to zero intensity in each case.

A one-dimensional bifurcation diagram that illustrates this structure is shown in Fig. 4.2. The vertical arrow labelled (i) marks the location of the data from Fig. 4.1 at 10 GHz detuning. One can see that at the largest positive detunings shown, the device is a dual-mode single period limit cycle state, and that this state transitions via a period-doubling bifurcation around 11.5 GHz detuning. As the detuning decreases towards 10 GHz, a bifurcation into the complex dynamical state of Fig. 4.1 is found. Using numerical continuation tools, it was shown in [38], that these dynamics originate in a torus bifurcation of the dual-mode periodic orbit.

Although this novel dynamical state was found in the dual-mode injected device, which is a forced system of coupled oscillators, we will present measurements and numerical results in this chapter that have many similar elements. These include oppositely

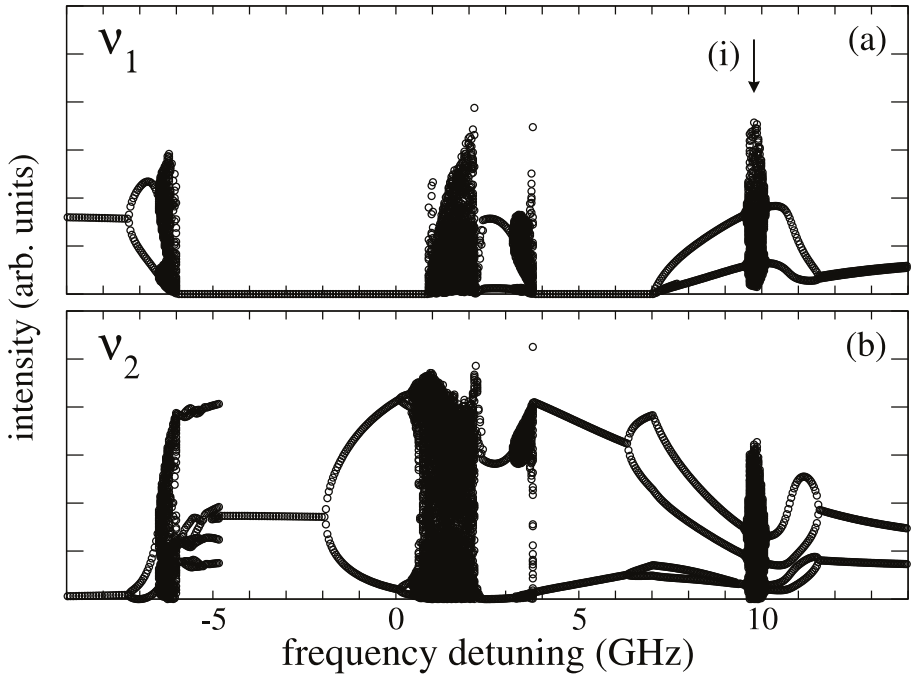

Figure 4.2: Local extrema of the field intensities (a) $|E_1|^2$ and (b) $|E_2|^2$ obtained from numerical integration of Eqs. (1)– (3) as a function of the detuning. The injected field strength is $K = 0.008$. Upper panel: uninjected field. Lower panel: Injected field.

directed, saw-tooth type characteristic waveforms, and a role for a torus bifurcation in the transition to complex dynamics. This is despite the fact that the dual-mode two-section device is not a forced system but one that becomes spontaneously unstable on account of the presence of the saturable absorber. In addition, we will find that the agreement between the experimental measurements that we will present in this chapter and our numerical results are much stronger than in the previous chapter. This level of agreement compares to that illustrated in Fig. 4.1, and provides convincing evidence that our model for the dual-mode two-section device captures many of the features of the physical system.

4.2 Experimental measurements of spiralling orbits in a two-section semiconductor laser

Once again, the device we now consider is a multi-quantum well Indium Phosphide based ridge-waveguide Fabry-Perot laser with one high-reflection (HR) coated mirror. The total device length is 545 μm with a saturable absorber section of length 30 μm

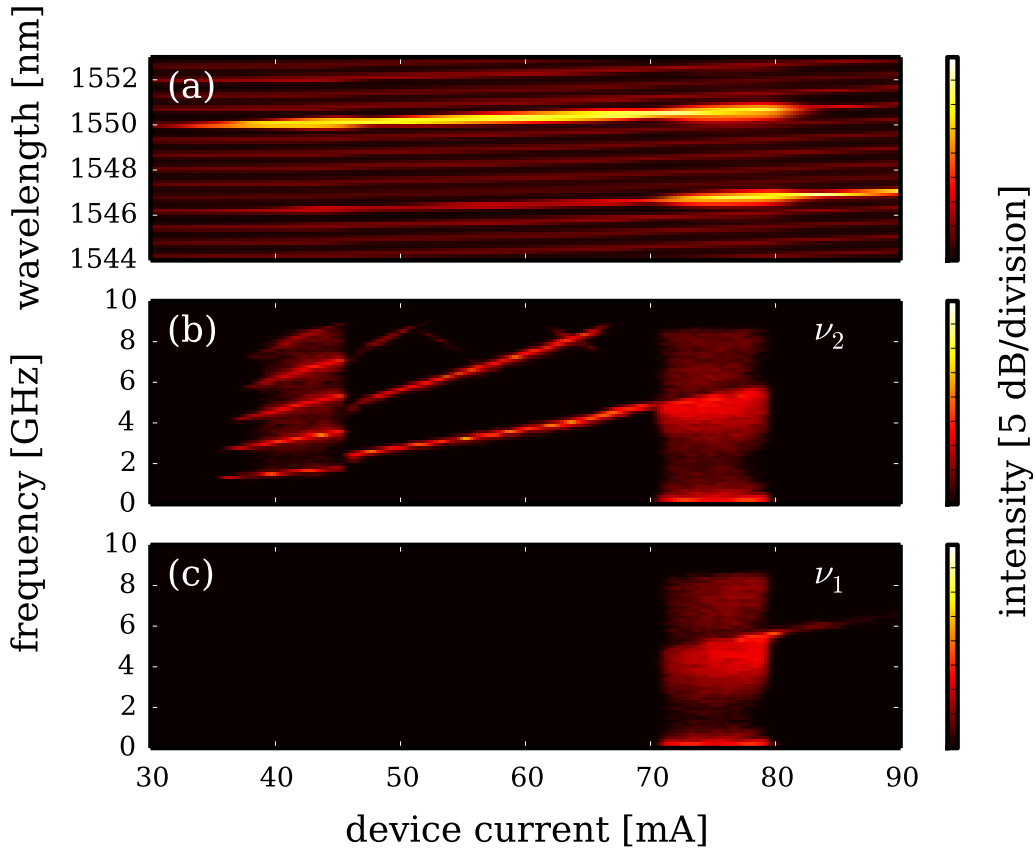

Figure 4.3: (a) Optical spectrum of the dual-mode two-section device as the device current is varied. The bias applied to the absorber section is 0 V. (b) and (c) Corresponding power spectra of the short (ν_1) and long (ν_2) wavelength primary modes.

adjacent to the HR mirror. The device has a peak gain near 1550 nm, and slotted regions in the laser ridge define a spectral filter as before. The primary modes spacing is 480 GHz. Fig. 4.3 (a) shows the optical spectrum of the laser as the drive current in the gain section of the device is varied. These spectra were obtained keeping a constant bias on the short contact of 0 V and varying the pump current in the gain section from below lasing threshold at 30 mA to a value of 90 mA. All measurements of this device were carried out at a temperature of 16.3°C.

From Fig. 4.3 (a) we see that the long wavelength mode of the device reaches threshold first at a drive current of 30 mA. The two primary lasing modes are located near 1550 nm and 1546 nm and they have a spacing of six fundamental cavity modes. These primary modes dominate the spectrum throughout the parameter region of interest. The corresponding power spectral densities for each of the primary modes are shown in Fig. 4.3 (b) and (c). As in the previous chapter, these measurements were not taken simultaneously, but a 0 V reverse bias in the absorber section was maintained in all cases. Structure appears in the power spectral density of ν_2 at approximately 35 mA, indicating the onset of dynamical modulation with a frequency of c. 1.5 GHz. This

transition is also reflected in a clear spectral broadening visible in the optical spectrum of the mode. We identify these dynamics as single mode self-pulsations, which appear following a region of constant output in mode ν_2 at threshold. The self-pulsations are initially sinusoidal and their frequency increases gradually with device current until a further transition at c. 45 mA. Near this value of the device current a discontinuity appears in the frequency of the intensity modulation, which subsequently increases again until a device current of 70 mA, where a dramatic switch to a region of dual-mode dynamics is observed. In the region of dual-mode dynamics the power spectra become symmetrical with a large range of frequencies present, including a signature of low-frequency modulation in the 100 MHz range. This region extends over a current range of approximately 10 mA, with the dynamics switching abruptly to the short wavelength mode ν_1 near 80 mA. Following the dual-mode region we observe a single peak in the intensity power spectrum that gradually diminishes in strength, indicating that, for the largest values of the device current shown, we have reached a state of constant output on the mode at short wavelength.

Representative time traces for the intensity of the long wavelength mode in the first and second regions of dynamics are shown in Fig. 4.4 (a) and (b). The device currents are 44 and 59 mA respectively. Fig. 4.4 (a) shows characteristic self-pulsation dynamics, where the intensity reaches small values between pulses and the pulse duration is significantly less than the interval between pulses. The dynamics in the second region as shown in Fig. 4.4 (b) are also strongly modulated but they are much closer to sinusoidal than in the region of self-pulsations. The sinusoidal nature of this modulation suggests that this modulation is of a different nature to the self-pulsating dynamics seen at smaller values of the pump current.

Time traces of the total intensity and of the individual modes taken from the region of dual-mode dynamics are shown in Fig. 4.4. (c-h). The device current in the long contact for these measurements was 75 mA. One can see that the total intensity experiences regular bursts of fast pulsations that are modulated by a much lower frequency envelope. The individual modes in this dynamical state display a distinctive symmetrical saw-tooth structure, where each mode closely follows a time-reversed trajectory of the other. One can see that there is a significant antiphase component to these dynamics, as the intensity of the individual modes reaches values close to zero over a considerable interval, whereas the total intensity is modulated around a finite background level.

4.3 Bifurcations of a dual-mode laser with saturable absorption: Case of large Δ

As discussed in the previous chapter, the carrier lifetime in the absorber section can be much shorter than that of the gain section. Motivated by the results of Chapter 2,

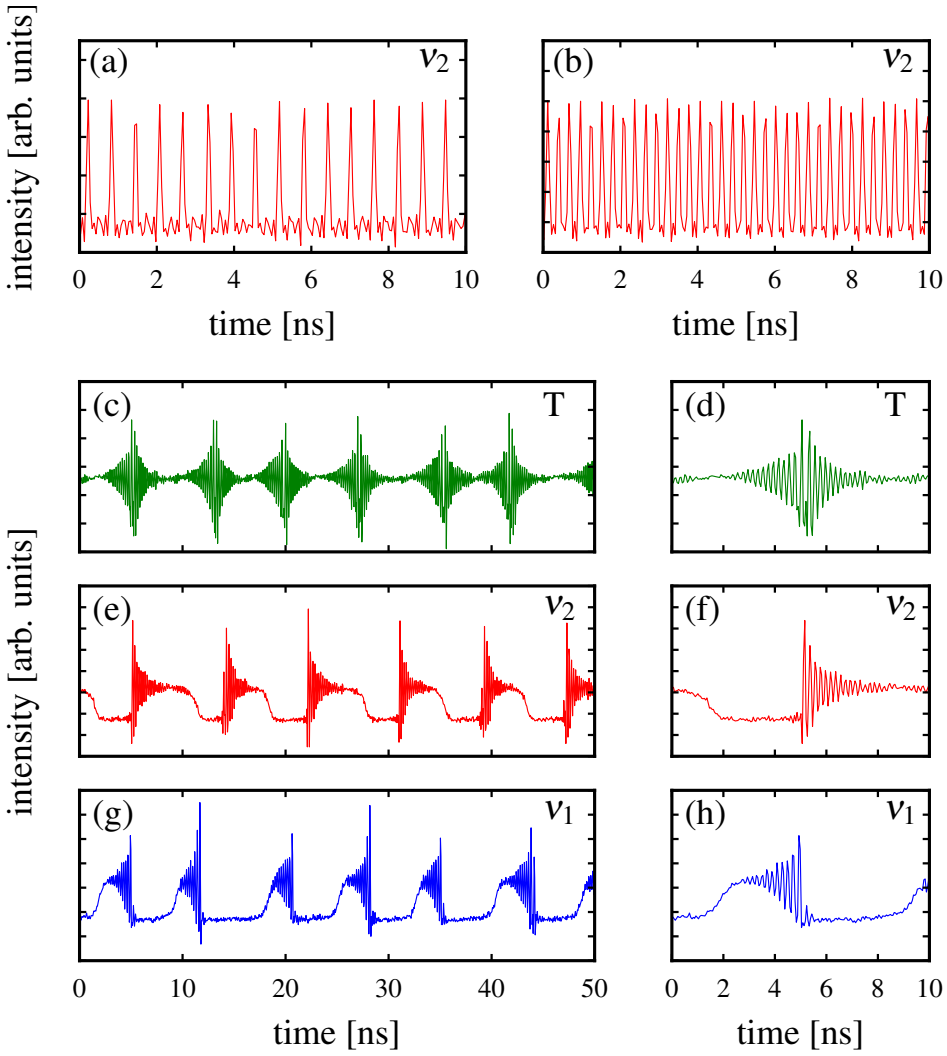

Figure 4.4: (a) and (b) Measured time traces for the long-wavelength mode ν_2 for a device current in the gain section of 44 and 59 mA respectively. (c) and (d) Time traces of the total intensity at a current of 75 mA in the gain section. (e)-(h) Mode resolved time traces at a current of 75 mA in the gain section. The bias applied to the absorber section is 0 V in all cases.

in our previous chapter we fixed the carrier lifetime of the gain section so that $\Delta = 3$. However, values quoted in the literature for similar systems are typically significantly larger [51]. In order to demonstrate that our experimental results presented in the current chapter do not require a small value of the Δ parameter, in this section we will fix the carrier lifetime in the absorber section to be 50 ps, so that the value of Δ is approximately equal to 20. Later we will also show how the dynamics observed in this chapter and in the previous chapter are organised as the Δ parameter is varied over a wide range.

In Fig. 3.7 we plotted a schematic of the dispersion of a typical gain and absorption spectrum, and used it as a guide for our simulation parameters. Here we present Fig. 4.5, which shows a similar schematic, but with a smaller amount of linear absorption. This change is motivated by the fact that the threshold current in this example is 30

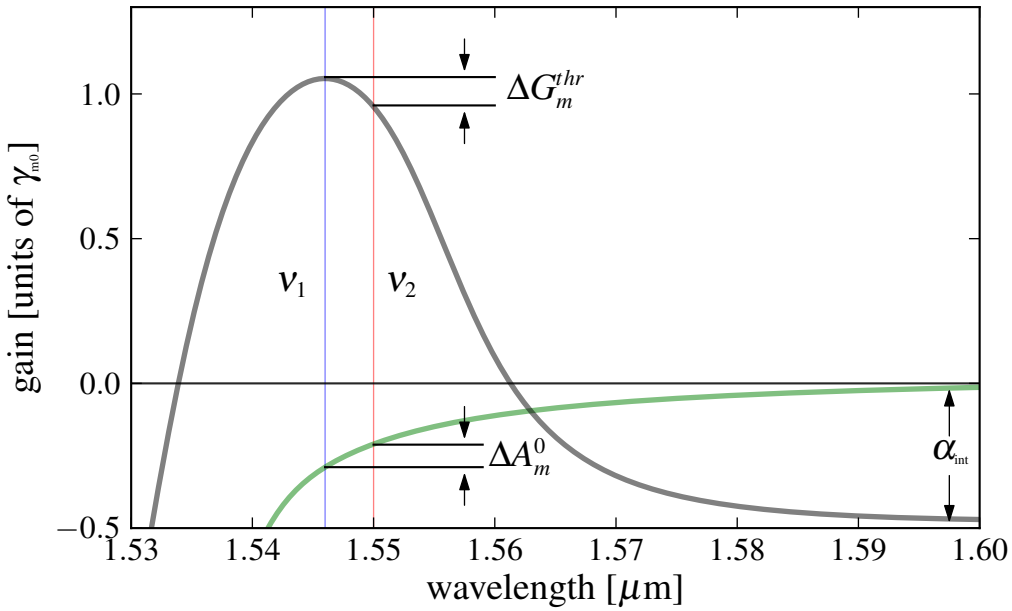

Figure 4.5: Schematic diagram of the material gain and absorption in a typical semiconductor laser. The locations of the two primary modes of the device ν_1 and ν_2 are indicated. The model parameters that describe the dispersion of the modal gain and absorption are also highlighted.

mA, which is a significant reduction from the 35 mA of the previous Chapter. We have once again schematically indicated the locations of the two primary modes of the laser.

With parameters taken from Table 4.1, mode resolved numerical bifurcation diagrams and power spectra for the two modes in the full coupled mode system are shown in Fig. 4.6 (c)-(f). As was the case in Chapter 3, these parameters ensure that the long wavelength mode reaches threshold first, and because the second mode is initially suppressed, mode ν_2 reproduces the dynamics found in the single mode system. As in the previous chapter, the region of single mode SP ends at the second Hopf bifurcation shown in Fig. 4.6 (a), the dynamics become dual-mode, with the SP intensity gradually switching across to the shorter wavelength mode ν_1 as the pump is increased further. This dual-mode region comes to an end shortly after a pump value of $j_s = 3$, where the system enters a region of single mode SP on ν_1. At large values of the pump current, as in Chapter 3, the region of SP dynamics finally ends at the subcritical Hopf bifurcation of ν_1, and the dynamics switch to constant output in mode ν_1 for large values of the pump current.

Table 4.1: Parameters describing the gain and absorption for Fig. 4.6

	ν_1	ν_2
g_{gj}	1.0	1.4
$g_{qj}\rho^{-1}$	1.2	0.6
$A_j^0\gamma^{-1}$	0.2	0.2
$\Delta G_{mj}^{thr}\gamma$	0	0

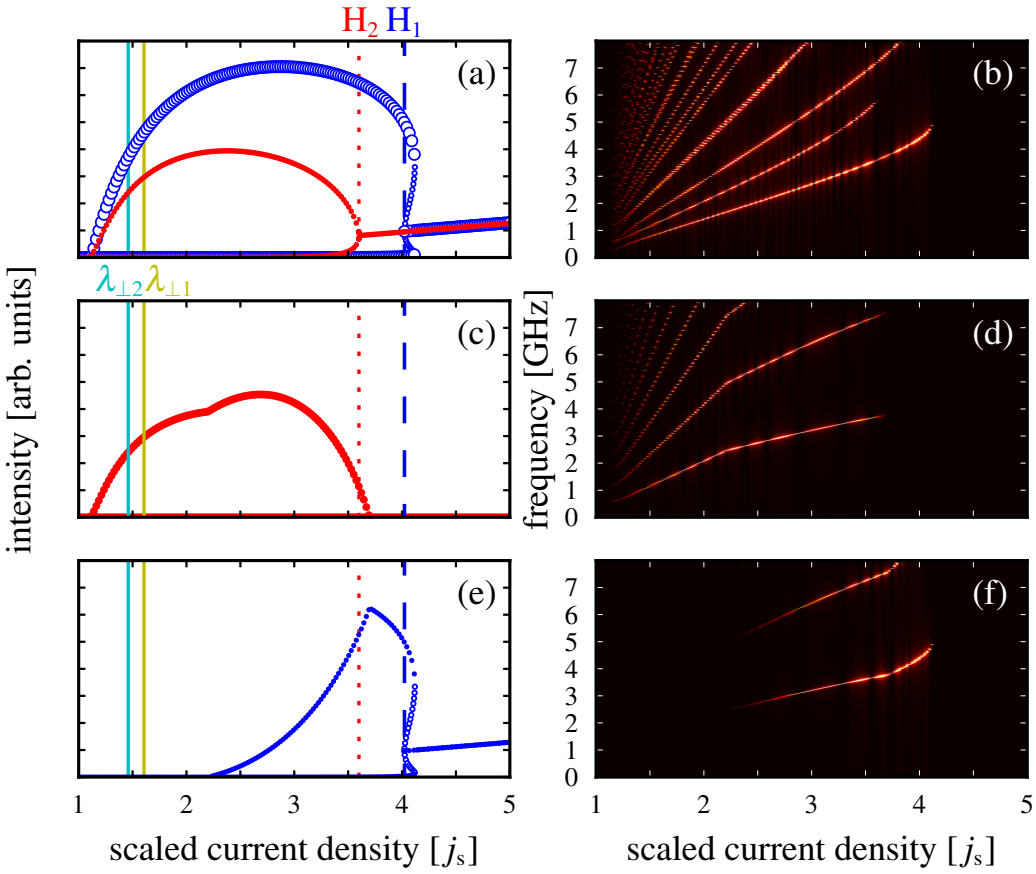

Figure 4.6: Left panels: Simulated bifurcation diagrams. Right panels: Power spectral densities. (a) and (b): Single-mode dynamics. Note: Here we have combined both sets of single mode simulations in a single figure. (c) and (d): Short wavelength mode ν_1. (e) and (f): Long-wavelength mode ν_2. Parameters are as in Table 4.1.

Valuable insight into what factors can lead to better agreement with experiment can be gained from a close examination of the time traces presented in Fig. 4.4 (c-h). From these figures, we see that for the majority of the orbit duration the intensity is close to the single mode manifold of one mode or the other. In Fig. 4.4 (h) we see the large intensity oscillations of ν_2 decaying toward a state with almost constant output, and the intensity then quickly switching to a similar state in ν_1 from which the oscillations grow again. The clear observation of this near single mode state with constant output at the beginning and end of these pulse packages suggests that the single mode steady states of (3.2) may be playing an important role in organising the observed dynamics. In particular, given the presence of symmetric invariant sub-manifolds in the phase-space, we should examine the dependence of the transverse stability of the single mode equilibrium solutions on the model parameters.

The transverse stability of the single-mode equilibrium solution for mode ν_i, I_i^0, is

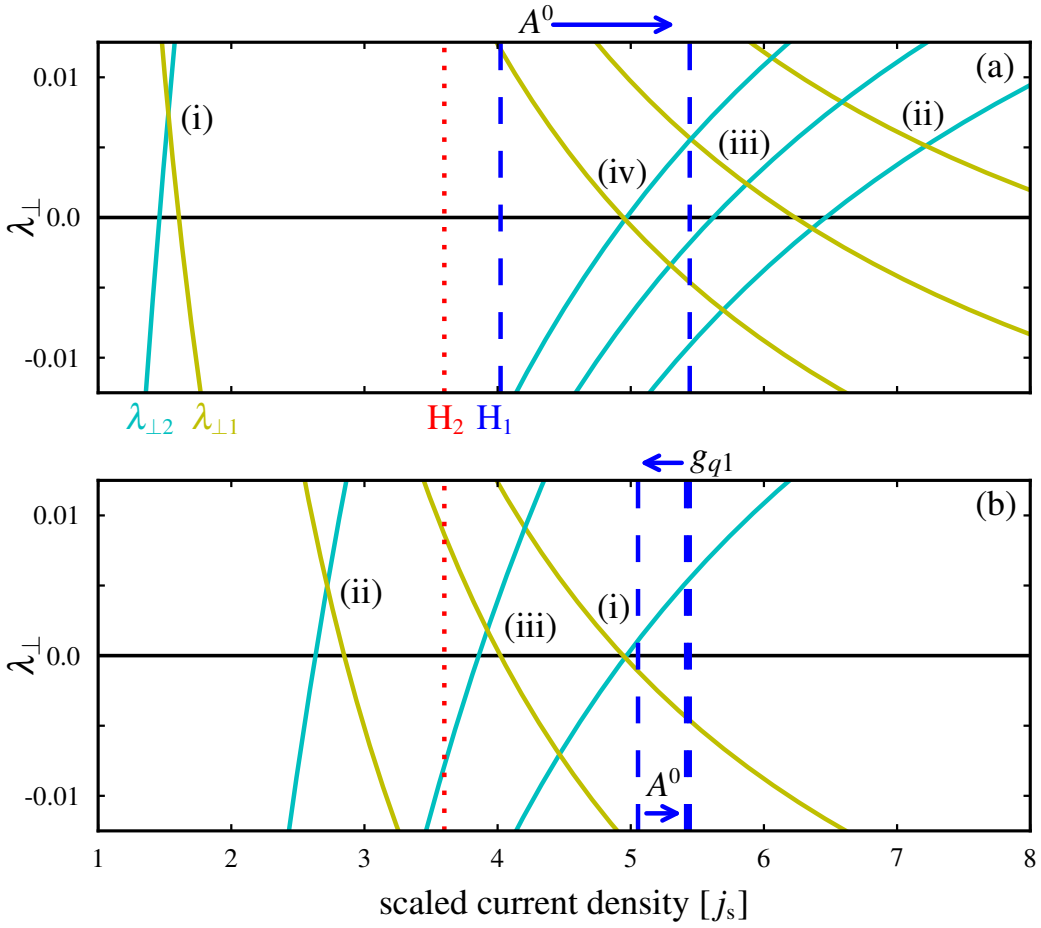

Figure 4.7: Effect of including dispersion in model parameters on the transverse Lyapunov exponent and the location of the second Hopf bifurcation of each single-mode equilibrium of the model. Dashed and dotted lines indicate Hopf bifurcations of ν_1 and ν_2 respectively. Solid lines are the transverse Lyapunov exponents of each mode as indicated. (a) (i) Parameters as in Fig. 4.6, (ii)-(iv)$A_1^0 = 0.35\gamma$ and $\Delta G_{m2}^{\text{thr}} = [\text{(ii)}0, \text{(iii)} - 0.25, \text{(iv)} - 0.5]\gamma^{-1}$. (b) (i) Parameters as in (iv) of (a), (ii),(iii)$g_{q1} = 1.5$, and $A_1^0 = \text{(ii)}0.35\gamma$, (iii)$0.4\gamma$.

determined by the sign of its transverse Lyapunov exponent

$$\lambda_{\perp i} = (1-\rho)G_j(I_i^0) + \rho A_j(I_i^0) - \gamma_j \tag{4.1}$$

where $\{i, j\} = \{1, 2\}$ and mode ν_i is transversally stable for negative values of $\lambda_{\perp i}$. For illustration purposes, we have plotted and labelled solid lines in Fig. 4.6 that indicate where the changes in transverse stability occur for the chosen parameter values. Note that in this case ν_1 becomes transversally stable while ν_2 becomes transversally unstable with increasing j_s. The impact of dispersion of linear gain and unsaturated absorption on the dynamics of our model can be illustrated by a plot of the locations of the Hopf bifurcations and changes in transverse stability of the single mode steady-states as the relevant parameters are varied. In Fig. 4.5, the physical dispersion of the unsaturated absorption suggests a larger value of A^0 for ν_1, and stability changes for both modes

obtained with A_1^0 increased to a value of 0.35γ, and $\Delta G_{m2}^{\text{thr}}$ ranging from 0 to $-0.5\gamma^{-1}$ are shown in Fig. 4.7 (a). In these figures vertical dashed and dotted lines indicate the locations of the second Hopf bifurcation for ν_1 and ν_2 respectively. Curved solid lines plot the value of the transverse Lyapunov exponent for each mode as indicated, with sign changes of these quantities indicating changes in transverse stability. One can see the impact that a change of only 0.5 cm^{-1} to the linear gain profile has on the transverse stability properties of these modes. The cumulative net effect of these changes is that there is now a much larger separation between the second Hopf bifurcation points of both modes. In addition, the sign changes of the transverse Lyapunov exponents for each mode now occur between the pair of Hopf bifurcations.

Table 4.2: Parameters describing the gain and absorption for Fig. 4.8

	ν_1	ν_2
g_{gj}	1.0	1.4
$g_{qj}\rho^{-1}$	1.2	0.6
$A_j^0\gamma^{-1}$	0.35	0.2
$\Delta G_{mj}^{thr}\gamma$	0	-0.5

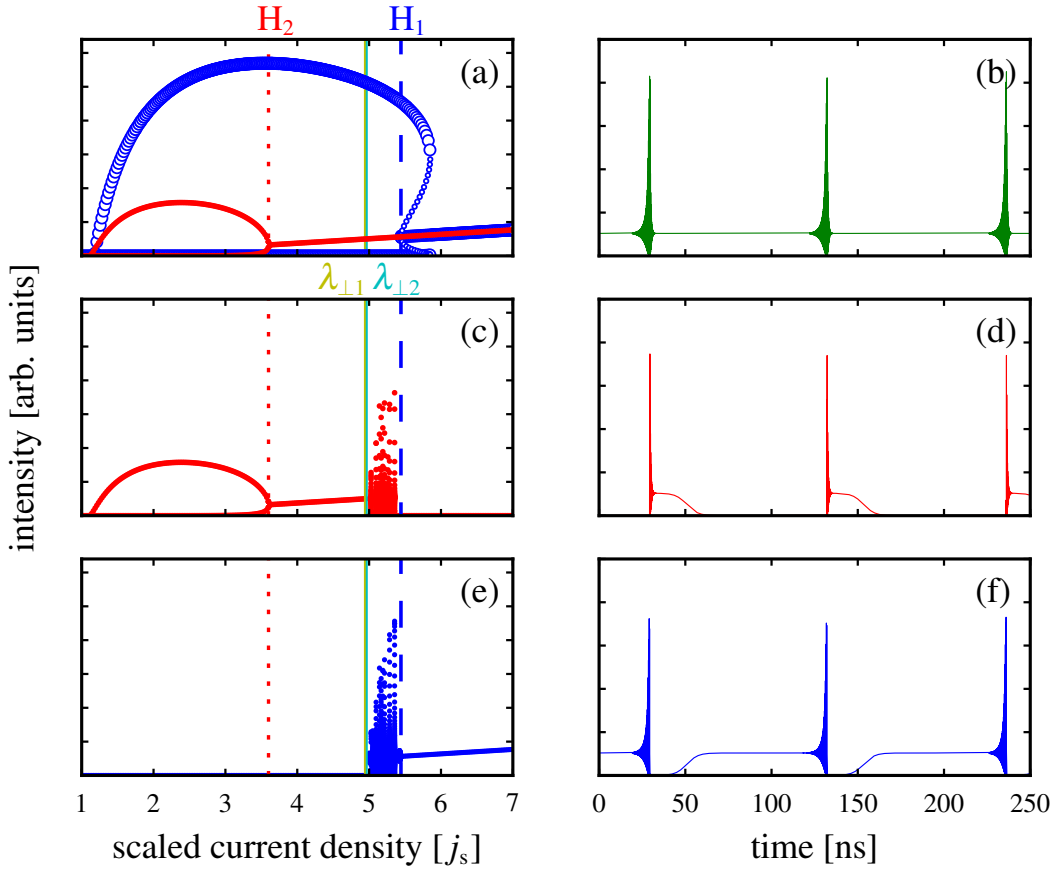

Figure 4.8: Left panels: Simulated bifurcation diagrams. Right panels: Intensity time traces. (a) Single-mode dynamics. (b) Total intensity. (c) and (d) Short wavelength mode ν_1. (e) and (f) Long-wavelength mode ν_2. Parameters are as in Table 4.2.

Numerical bifurcation diagrams obtained for parameter set (iv) of Fig. 4.7 (a) are plotted in in the left hand panels of Fig. 4.8. Here, $A_1 = 0.35\gamma$, $\Delta G_{m2}^{\text{thr}} = -0.5\gamma^{-1}$, and all other parameters are unchanged from Fig. 4.6. The increased unsaturated losses mean that mode ν_1 is suppressed for longer and, in contrast to the results of Fig. 4.6, mode ν_2 now completes a region of single-mode SP bounded by two single mode Hopf bifurcations. Following the SP region, the system enters a region of single-mode constant output. However, as we increase the pump current still further we find the dynamics are dramatically "blown-out" from the single mode manifold and we enter a region of coupled dynamics in both modes. The location of the blow-out is determined by the loss of transverse stability of ν_2, and this point is located shortly after ν_1 has become transversally stable. The region of dual-mode dynamics is again bounded at larger values of the pump current by a subcritical Hopf bifurcation of mode ν_1.

In order to compare the measurements of Fig. 4.4 in the dual-mode region with the simulation results of Fig. 4.8, we have plotted mode-resolved and total intensity time traces with $j_s = 5.1$ in the right-hand panels of Fig. 4.8. The similar nature of the two dynamical states is clear, with the numerical results reproducing the observed bursts of fast pulsations in the total intensity and also the switching sequence with the intensity rising on the short wavelength mode before switching and falling on the long wavelength mode. However, the frequency of the bursts that we find numerically is much too low at around 50 MHz. It is possible that the addition of noise to the simulations would improve this agreement, as this would increase the likelihood of triggering a pulse. In addition however, the numerical bifurcation sequence is not in full agreement with our measurements. We find a large region of constant output between the second Hopf bifurcation of ν_2 and the onset of coupled mode dynamics and we also do not see any evidence of a discontinuity in the frequency of the intensity modulation at intermediate values of the pump.

By further adjustment of parameters we can shift the point where the transverse stability of the equilibrium state of ν_1 changes to smaller values of the pump. This will result in a narrowing of the region of constant output in agreement with experiment. Fig. 4.7 (b) illustrates the effect of an increase in g_{q1} combined with a further increase of A_1^0. The net effect of these adjustments is that the positions of the Hopf bifurcations remain largely the same, but the changes of transverse stability happen much closer in pump current to the second Hopf bifurcation of ν_2. Numerical bifurcation diagrams and intensity power spectra with $g_{q1} = 1.5$ and $A_1^0 = 0.4$ are shown in Fig. 4.9. Until the single mode steady state of ν_2 becomes transversally unstable, the bifurcation sequence we observe is the same as in Fig. 4.8. However, instead of a dramatic transition to a region of complex coupled dynamics, in this case we find a very narrow region where a dual-mode equilibrium state of the system is stable. This state appears here for the first time in our simulations, and it appears because the order of the changes in transverse stability of the single-mode steady-states has been reversed compared to

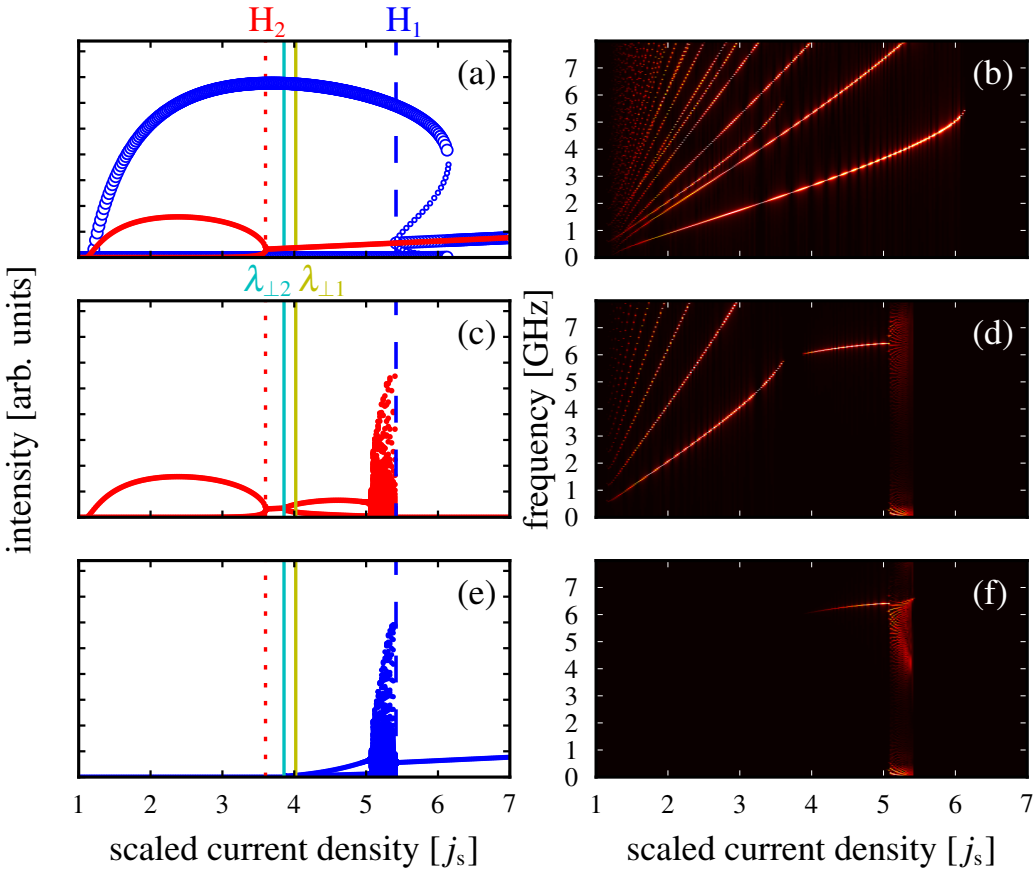

Figure 4.9: Left panels: Simulated bifurcation diagrams. Right panels: Power spectral densities. (a) and (b): Single-mode dynamics. (c) and (d): Short wavelength mode ν_1. (e) and (f): Long-wavelength mode ν_2. Parameters are as in Table 4.3.

the previous example. We find that the dual-mode equilibrium state quickly evolves into a dual-mode limit cycle at a Hopf bifurcation point. This dual-mode limit cycle is unusual in that the amplitude of ν_1 over the cycle is very weak to begin. With a further increase in the pump current, the dual mode limit cycle loses stability, and we observe a dramatic transition to a region of complex coupled dynamics in both modes. As in the previous example, the region of complex dynamics is bounded at a large pump current by a subcritical Hopf bifurcation in ν_1.

Table 4.3: Parameters describing the gain and absorption for Figures 4.9 - 4.11.

	ν_1	ν_2
g_{gj}	1.0	1.4
$g_{qj}\rho^{-1}$	1.5	0.6
$A_{\mathrm{j}}^{0}\gamma^{-1}$	0.4	0.2
$\Delta G_{\mathrm{mj}}^{thr}\gamma$	0	-0.5

A plot of the mode-resolved and total intensity time traces taken from the region of complex coupled dynamics in Fig. 4.9 with $j_s = 5.2$ is shown in the left-hand panels of Fig. 4.10. When compared to our experimental results, there is a greater degree

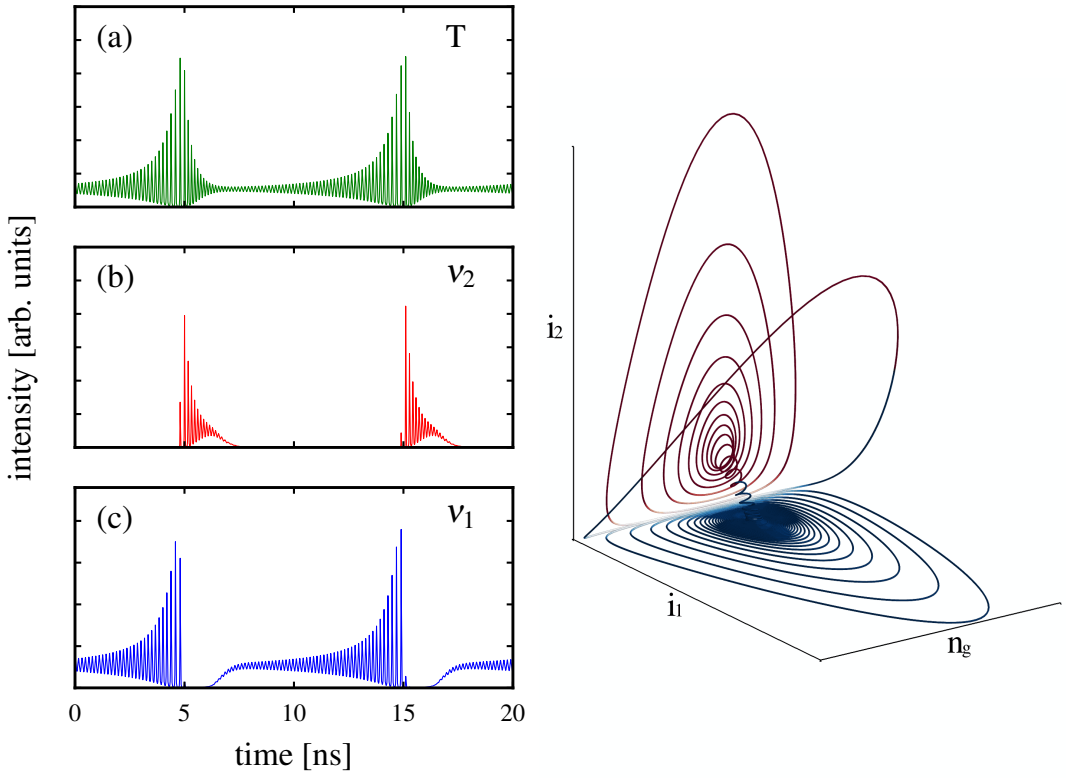

Figure 4.10: Left: Simulated intensity time traces. (a) Total intensity. (b) Short wavelength mode ν_1. (c) Long-wavelength mode ν_2. Right: Phase space diagram. Parameters are as in Table 4.3.

of asymmetry between the dynamics of the two modes in this example. Unlike the previous example however, the frequency of the bursts of fast pulsations of the total intensity is now accurately matched to our experimental results. We note also that the observed bifurcation sequence provides an explanation for the dynamics we found at intermediate values of the pump current in our experiment. We can now see that the discontinuity in the frequency of the intensity modulation of ν_2 was due to the momentary appearance of a stable dual-mode steady state in the system, leading to the absence of any structure in the intensity power spectrum over this interval. In addition, we must reinterpret the region after the discontinuity as a dual-mode state with strong intensity modulation, but where the amplitude of the component in ν_1 is very weak.

The time traces of Fig. 4.10 are depicted in a phase-space representation on the right of Fig. 4.10. If we consider trajectories close to the single-mode equilibrium state of ν_1, these trajectories are attracted towards the single mode manifold as the single-mode equilibrium state has a negative transverse Lyapunov exponent. Because this state is unstable in the single-mode manifold, as the trajectory approaches the manifold it is repelled into a spiralling orbit towards the SP limit cycle, which is stable within the ν_1 manifold. This is the origin of the fast pulsations that grow from the quasi-single

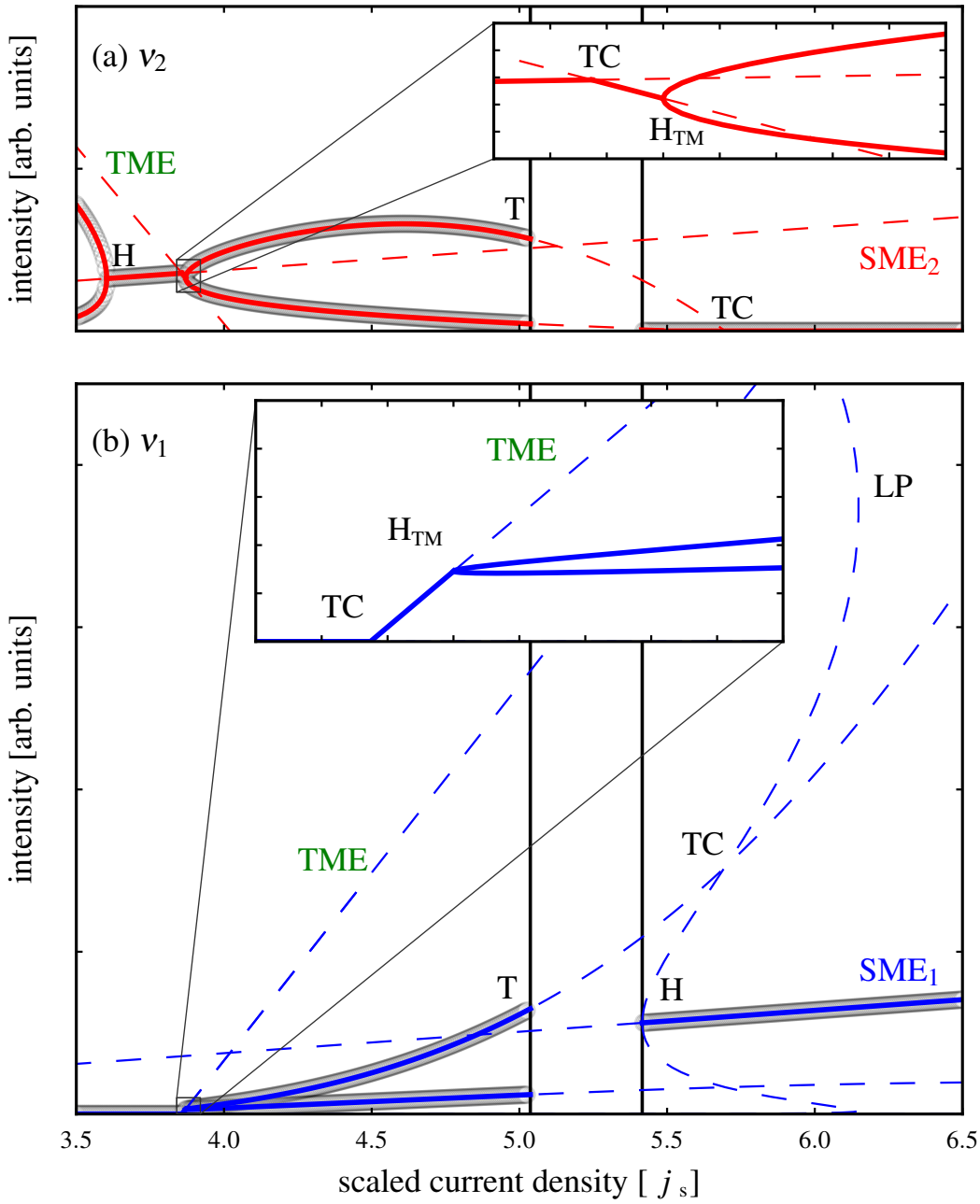

Figure 4.11: Bifurcation diagrams of ν_2 (upper panel) and nu_1 (lower panel). Single and dual-mode equilibrium states are labeled SME_j and TME respectively. Bifurcation points are single-mode Hopf bifurations (H), transcritical (TC), dual-mode Hopf bifurcations (H_{TM}), Torus bifurcations (T) and limit point (LP). Solid and dashed lines indicate stable and unstable objects respectively. The results of numerical simulations of the coupled system are superposed as a guide. The parameters here are as in Table 4.3.

mode steady state of ν_1. Once the trajectory approaches the SP limit cycle, it feels the transverse instability of this limit cycle and is ultimately ejected from the region near the single-mode manifold, undergoing a large amplitude excursion where both fields have large intensity. This large excursion leads the trajectory to enter the slow region near zero intensity, where it is drawn towards the single mode manifold of ν_2, where the single mode equilibrium state is stable within the manifold. This leads to the cycle of fast pulsations that decay towards the single mode equilibrium state of ν_2. Finally, as the trajectory approaches the equilibrium, it is repelled on account of the positive transverse Lyapunov exponent of this state. This repulsion drives the trajectory towards the transversally attracting equilibrium state of ν_1 and the cycle begins again. The switch in intensity from ν_2 to ν_1 is along a corkscrew type trajectory that is wound around the line connecting the equilibrium states in the two single mode manifolds. This winding may be a signature of the dual-mode limit cycle present before the region of complex dynamics.

To investigate this question and to shed more light on the bifurcation structure in this system, we have plotted numerical continuation results in Fig. 4.11. These results indicate that the instability of the dual-mode limit cycle leading to complex dynamics is due to a supercritical torus bifurcation (T). We can also see that the dual-mode limit cycle is present as an unstable object throughout the region of complex dynamics, and that there is evidence for further bifurcations of interest involving this object beyond the boundary of the region of complex dual-mode dynamics. In particular, we can see that the unstable dual-mode limit cycle collides with the unstable branch of single-mode SPs of mode ν_1 in a transcritical bifurcation (TC). This results in the unstable branch of single-mode SPs becoming transversally stable for decreasing pump values until the subcritical Hopf bifurcation of ν_1 is reached. This narrow region of transverse stability for this unstable branch of SPs may explain the sharp feature near the relaxation oscillation frequency found in the power spectral data of Fig. 4.3. The diminishing strength of this feature with increasing current could be a result of the growth of the limit cycle away from the location of the stable equilibrium.

4.4 Spiralling orbits at small values of the Δ parameter

In this thesis we have presented two contrasting examples of experimentally observed coupled dual-mode dynamics (Figs. 3.4 and 4.4). Both of these examples occur in devices which are nominally identical but which have slightly different dispersions in the gain and absorption parameters at the locations of the primary lasing modes. However, in Chapter 3, we concluded that the antiphase self-pulsation dynamics presented were only observable for relatively small values of Δ, whereas the results of this chapter, presented in the previous sections, were obtained at a considerably larger value of Δ. The question therefore arises as to whether we can adjust parameters in

order to approximately reproduce our experimental results in numerical simulations, but with a fixed value of the Δ parameter. In addition, we can ask over what range of the Δ parameter can we obtain both examples of characteristic experimental dynamics in numerical simulations, while only making physically appropriate adjustments to the parameters that describe the material dispersion in our devices.

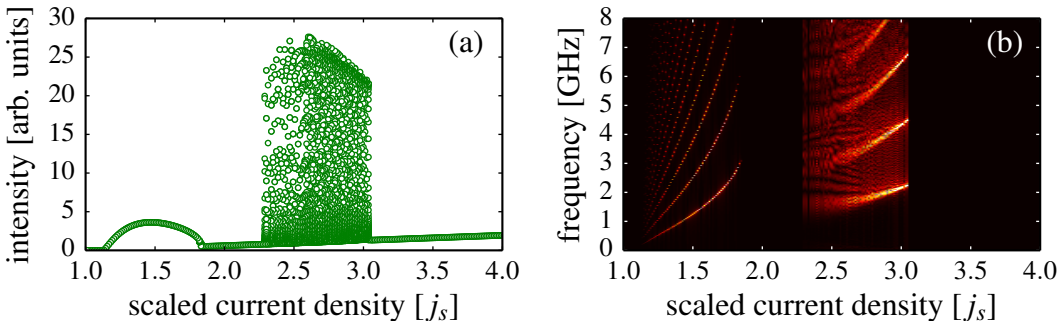

Figure 4.12: Left panel: Simulated bifurcation diagram of the total field intensity. Right panels: Power spectral density of the total field intensity. Parameters are as in Table 4.4.

With this in mind we return to the final parameter set and simulations of Chapter 3, as presented in Table 3.3 and Fig. 3.4. Referring to Fig. 3.4, by reducing the linear absorption A_2^0 we move the Hopf bifurcation present at large pump current much closer to threshold. In doing so, we ensure that ν_2 has already reached a steady state as we increase the pump current and begin the transition from ν_2 to ν_1. As we have shown in this chapter the value of the transverse Lyapunov exponent of the respective modes then becomes significant in determining the dynamics. Figure 4.12 shows the numerical bifurcation diagram and intensity power spectrum of the total intensity for the parameters shown in Table 4.4. The only parameter change here from the final result of Chapter 3 is in A_2^0. This sequence of bifurcations is identical to that presented in Fig. 4.8. For illustrative purposes, in Fig. 4.13 we present intensity time traces from these results for a pump current value of 2.5. The right panel of Fig. 4.13 allows us to see the nature of the fast switch between quasi-single mode states along a pencil like trajectory in the phase space.

Table 4.4: Parameters describing the gain and absorption for Fig. 4.12

	ν_1	ν_2
g_{gj}	1.0	1.4
$g_{qj}\rho^{-1}$	1.4	0.6
$A_{\mathrm{j}}^0\gamma^{-1}$	0.6	0.25
$\Delta G_{\mathrm{mj}}^{thr}\gamma$	0	-2.5

Figure 4.14 shows a two dimensional bifurcation diagram of the $p-\Delta$ parameter space. Once again, we see that the dramatic blow-out from the single-mode manifold coincides with loss of transverse Lyapunov stability of ν_2. This happens subsequent to ν_1 becoming transversally stable as we increase pump current from threshold. We

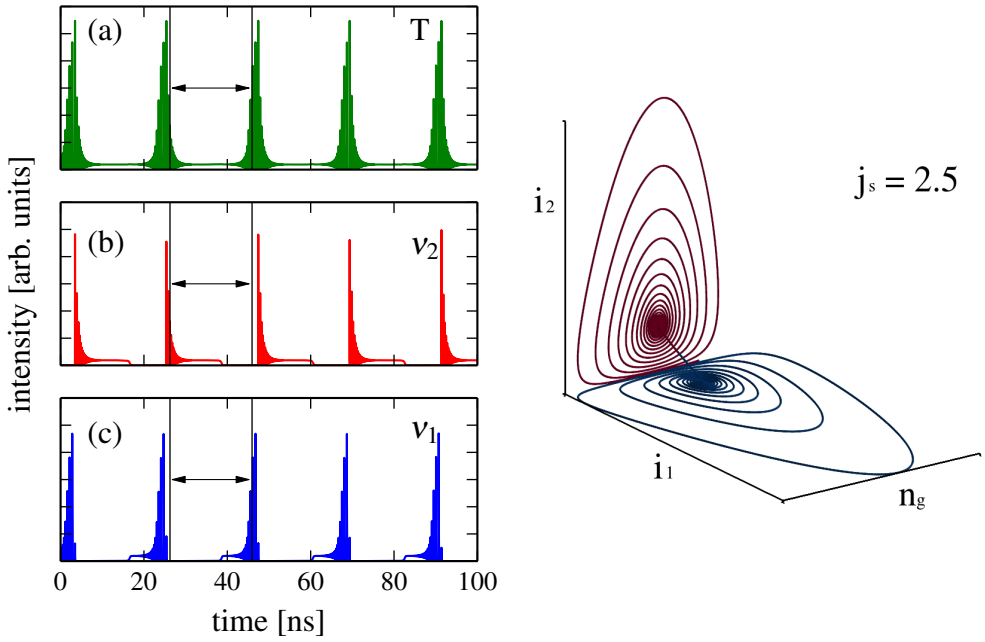

Figure 4.13: Left panel: Simulated time traces with a pump current of $j_s = 2.5$ for the parameters shown in Table 4.4. Right panel: Simulated phase space.

can see from Fig. 4.14 that this sequence is viable for a large range of Δ. A sizeable region of spiralling dynamics is bounded by the cyan line labeled $\lambda_{\perp 2}$ corresponding to the point where ν_2 becomes transversally unstable, and the blue HB line for the Hopf bifurcation of ν_1.

We see that in the case Fig. 4.14, where we observe a transition to spiralling time-reversed orbits in the two-section device, the relevant bifurcations occur on branches of single-mode steady-state solutions. This means that we can track transitions using the Lyapunov exponent, which can be calculated explicitly. In Fig. 3.19 by contrast, the physically significant period doubling bifurcations occur on branches of dual-mode limit cycle solutions. In the case of Fig. 3.19 the transition from single to dual-mode dynamics occurs earlier via a transcritical bifurcation where the single mode SP limit cycle "lifts" out from the single mode manifold.

Earlier in this chapter we moved from the results of Fig. 4.8 to Fig. 4.9 by adjusting the parameters to reverse the order of the changes in transverse stability of the single-mode equilibria. We did so by increasing the differential gain of ν_2 and increasing the linear absorption of ν_1. Here we make a change in the same spirit, by marginally increasing the differential absorption of ν_1 and reducing the dispersion of the linear gain ΔG_2^{thr}. Figure 4.15 was generated using the parameters shown in Table 4.5. Here we have reproduced the results of Fig. 4.9 at a small value of the Δ parameter ($\Delta = 3$). This is significant in the sense that we have now successfully generated a plausible picture of the experimental results of this chapter and of Chapter 3 at a single value of Δ, which

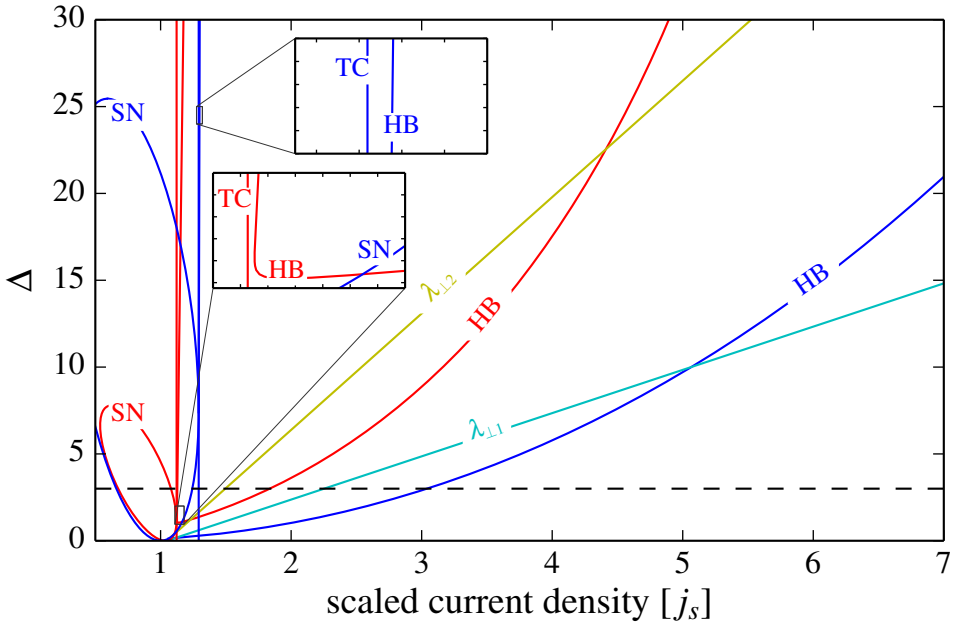

Figure 4.14: Bifurcation diagram in the j_s vs. Δ plane of Eqn. (3.2). Blue and red lines denote bifurcations of single mode states ν_1 and ν_2 respectively. Bifurcations of dual-mode states are shown in green. Yellow and cyan lines indicate changes in transverse stability of ν_1 and ν_2 respectively, with ν_1 becoming transversally stable and ν_2 becoming transversally unstable. The different lines of bifurcations are indicated by SN (saddle node), HB (Hopf) and TC (transcritical). Parameters are as in Table 4.4.

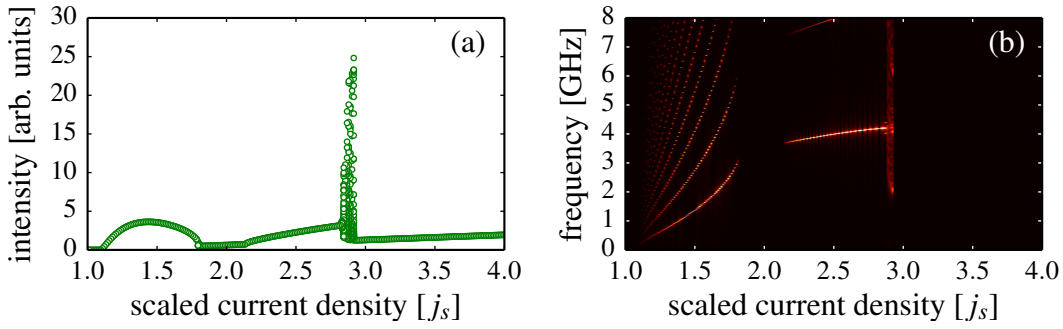

Figure 4.15: Left panel: Simulated bifurcation diagram of the total field intensity. Right panels: Power spectral density of the total field intensity. Parameters are as in Table 4.5.

suggests it may be an appropriate reflection of the physical values.

Table 4.5: Parameters describing the gain and absorption for Fig. 4.15

	ν_1	ν_2
g_{gj}	1.0	1.4
$g_{qj}\rho^{-1}$	1.6	0.6
$A_{\mathrm{j}}^{0}\gamma^{-1}$	0.6	0.25
$\Delta G_{\mathrm{mj}}^{thr}\gamma$	0	-0.25

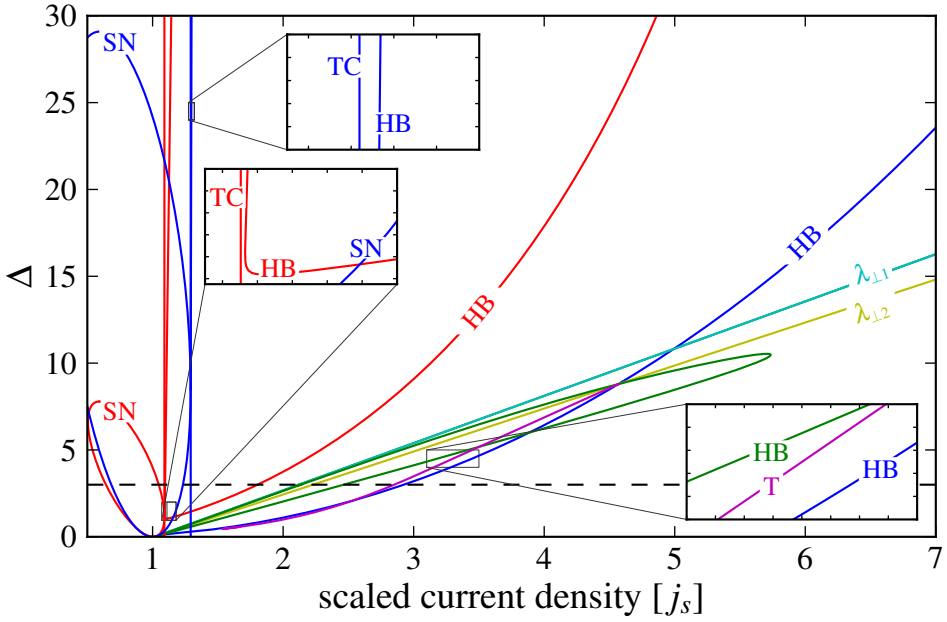

Figure 4.16: Bifurcation diagram in the j_s vs. Δ plane of Eqn. (3.2). Blue and red lines denote bifurcations of single mode states ν_1 and ν_2 respectively. Bifurcations of dual-mode states are shown in green. Yellow and cyan lines indicate changes in transverse stability of ν_1 and ν_2 respectively, with ν_1 becoming transversally stable and ν_2 becoming transversally unstable. The different lines of bifurcations are indicated by SN (saddle node), HB (Hopf), TC (transcritical) and T (torus). Parameters are as in Table 4.5.

Figure 4.16 shows the two dimensional map of the $p - \Delta$ parameter space for these values. This figure allows us to put the results of the previous section in context, and get a sense of the large scale structure of the region. The reversal of the transverse Lyapunov stability changes coincides with the appearance of a dual mode steady state, followed by a Hopf bifurcation of the dual mode state, and a subsequent torus bifurcation, all for increasing pump current. The region is bound at large pump current by a Hopf bifurcation of ν_1, whereupon the system returns to the single mode state.

In the current example depicted in Fig. 4.16, the order of the transverse Lyapunov stability changes once more plays a significant role. In the simple case, ν_2 is already transversally unstable by the time ν_1 gains transverse stability, meaning the dynamics completely blow out of the steady state near the ν_2 single mode manifold. With the order of the transverse stability changes reversed an extremely narrow region of two

mode steady state dynamics appears, beginning when ν_2 becomes transversally stable. From this state, a two mode Hopf bifurcation occurs. This bubble of dual-mode Hopf bifurcations is bounded at large pump current by a torus bifurcation, at which the blow out occurs. It is interesting that the bifurcation structure that governs the appearance of spiralling time-reversed orbits in the example of Fig. 4.1 is in some sense a hybrid of the bifurcation structures we have found in in the dual-mode two-section examples presented in this thesis. In the dual-mode injected system of Fig. 4.1, the spiralling orbits appear and disappear via torus bifurcations, which are found inside a larger structure of period doubling bifurcations. Although a further study of the underlying physical mechanisms that lead to the shared characteristics and subtle differences between the dual-mode injected and two-section systems is beyond the case of this thesis, we have highlighted interesting potential avenues for further research.

4.5 Conclusions

In this chapter we have presented a second experimental and numerical study of interesting dynamics in a dual-mode semiconductor laser with a saturable absorber. Our experimental method was closely related to that followed in Chapter 3. Fixing the voltage applied to the absorber section, we performed a sweep in drive current in the gain section of the device. In this case we found that the dynamics evolved from familiar self-pulsations in a single mode of the device into a complex dynamical state of both modes. Using the same rate equation model for the semiconductor laser with a saturable absorber that we employed in Chapter 3, we were able to reproduce the observed dynamics, and in this case we showed the fundamental role played by the transverse stability of single-mode steady states of the system in governing the appearance of the observed dynamics.

To demonstrate the general nature of our results, in this chapter we used a much larger value of the Δ parameter, but we also showed that the observed dynamics were not inconsistent with the small value employed in Chapter 3. Taken together, our results lend support to the conclusion that our devices are characterised by an unusually small value of Δ, and they demonstrate that the differences in the observed dynamics between two nominally identical devices are due to fabrication uncertainty and the presence of enhanced losses due to the etched regions that from the spectral filter. This origin is consistent with a change in the material dispersion parameters for the primary modes in each device, and also with constant values for the gain and absorber recovery times, which should not be affected by the manufacturing process to a significant degree.

Chapter 5

Conclusions and Outlook

In this thesis we have presented experimental measurements of self-pulsation phenomena from a variety of two-section semiconductor lasers. In each case we have sought to obtain numerical agreement and provide theoretical insight based on systems of rate-equations for the carrier densities and field intensities in each of the considered devices.

In our introduction to this thesis we began by highlighting the unique aspects and advantages of our laser design approach. We briefly discussed the discrete-mode laser design method that is based on spectral filtering of the Fabry-Pérot lasing modes and expressed using Fourier transforms. We described the promising performance characteristics of passively mode-locked discrete-mode devices and we discussed how semiconductor lasers with novel cavity geometries that provide tailored spectra have the potential to address important applications in advanced telecommunications and signal processing. We also showed how our study of self-pulsation phenomena could lead to a better understanding of the physical mechanisms that determine the stability of pulsed modes of operation that are important in modern applications.

In our second chapter we mapped the phase-space structure of self-pulsation dynamics in a two-section Fabry-Pérot laser as a function of injected current and reverse bias applied to the saturable absorber section. We then introduced the laser with a saturable absorber [LSA] rate equation model of the dynamics and we showed how one could derive physically appropriate model parameters using a semi-analytic approximation for the gain and absorption in the two sections of the laser. Using model parameters obtained from the measured material dispersion, we presented a detailed discussion of the bifurcation structure that governs the appearance of self-pulsations in two-section devices. We established typical parameter ranges by comparing the results of numerical simulations with experimental measurements. We found that the LSA model had certain shortcomings and in order to achieve greater certainty in our estimate

for the ratio of the carrier lifetimes in the device, we introduced a more accurate delay-differential model of the device. This model provided better agreement with experiment and confidence in our estimates of the relevant time-scales in the system.

In the following two chapters, we presented two distinct examples of experimental measurements from dual-mode two-section devices. In Chapter 3, we first showed how to extend the LSA model to the multimode case, and we then presented experimental results showing how single mode self-pulsations evolved into a coupled dual-mode state characterised by dropouts in the total intensity and a seeming loss of frequency synchronisation between the two coupled modes. We presented optical and mode resolved power spectra as well as a series of characteristic intensity time traces illustrating this progression, and we were able to qualitatively reproduce this observed behaviour in numerical simulations following a procedure of adjusting model parameters in order to reflect the material dispersion and the observed characteristic series of bifurcations in our experiment. Using numerical continuation tools to determine the global bifurcation structure, we finally presented evidence that suggests that we may have observed an example of chaotic SPs in the dual-mode system. We also argued that our experimental results can be interpreted in terms of an inability of the coupled modes to synchronise their individual SPs that may be the origin of the complex dynamics in this case.

In Chapter 4, we presented a second example of coupled dual-mode dynamics. Although the device considered was nominally identical to the device of Chapter 3, this example was significantly different and characterised by time-reversed sawtooth waveforms that had a parallel in an optical injected dual-mode example considered previously by colleagues. We presented evidence suggesting that the differences between these devices could be explained by the manufacturing process that leads to small but significant variations between devices fabricated on different parts of the semiconductor wafer. Following a similar strategy in adjusting model parameters to the example of Chapter 3, we showed that these dynamics could be reproduced with high accuracy using our extended LSA model. To complete our study of dual-mode two-section devices we revisited the example of Chapter 3, and we showed how the two examples of complex dynamics that we observed can be understood in a unified picture. The results of this section showed that our results were consistent with a single set of time-scales for the carrier recovery times in each device and that variations in the material dispersion imposed by the spectral filter could explain the difference in the characteristic dynamics observed with each of the two devices.

5.1 Outlook

The work presented in this thesis can provide a number of interesting avenues for further research. In our final section we discuss some of the future research directions

that we have identified in modelling of two-section semiconductor lasers and their potential applications in integrated optics.

Our work presented here has focussed on the study of multimode SP phenomena, and we have highlighted a number of interesting parallels with nonlinear dynamics of optically injected dual-mode systems. Further work will be necessary to understand fully the origin of the complex SP dynamics discussed in Chapter 3, and to demonstrate conclusively that we have observed a transition to chaos in our experiments. We have outlined a strategy based on deriving a low-dimensional description of the system in terms of coupled maps that may allow us to describe a transition to chaos within the framework of synchronisation of coupled SPs of the individual modes.

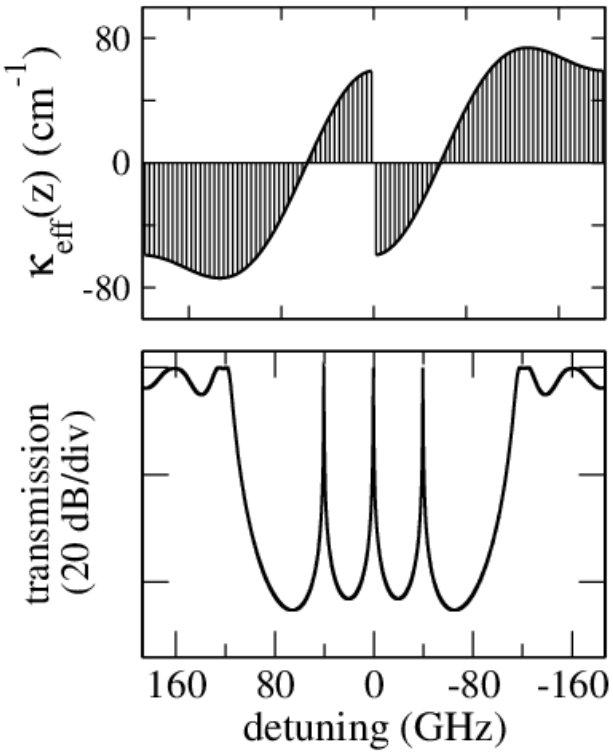

Figure 5.1: Upper panel: Effective coupling constant of a 40 GHz spaced filter. Lower panel: Transmission of the lossless filter [63].

We have also discussed how extensions of the multimode LSA system that we have employed here can become useful tools for the understanding of mode-locked devices with tailored spectra. Although the LSA model has some serious limitations, including its neglect of dynamics at the device round trip frequency and its assumption of small gain and absorption, it does capture certain aspects of the modal dynamics that are not as well described by total field descriptions, such as that of the delay-differential model. In particular, we have demonstrated clearly how dispersion in the material gain and absorption and their effects are described in a natural way by the LSA model. By extending the model to include mutual coupling of fields via four-wave mixing

terms, the model can also describe the local refractive index dispersion in a two-section device, and its impact on the stability of mode-locked states of the system. This ability to capture the local material dispersion and its effects, together with the effects of a complex grating spectral filter can complement modelling efforts describing the nonlinear saturation in the device more accurately.

We should emphasise here also that because the LSA model does not describe the dynamics at the round trip frequency in the device, a mode-locked state of an extended LSA model would be described as a steady-state representing a mutually injection locked comb of modes. As a result, we cannot describe the intensity and carrier density modulation at the round-trip frequency. However, in cases where the mode-locked bandwidth is limited, this may not be an unreasonable approximation, as the amplitude of the modulation in this case will also be limited.

Regarding future research into applied problems and technology development, we have discussed how the development of integrated laser sources has experienced tremendous progress in recent years, and, in our introduction, we have highlighted two recent designs that can address important applications in integrated optics. We have pointed to the fundamental physical relationships that suggest that we can adapt our discrete-mode laser design approach to obtain high-performance mode-locked devices using design methods from silicon photonics technology. A major advantage of devices defined by distributed feedback grating filters is the minimisation of lasing wavelength errors associated with the definition of the device length. These filters can be readily incorporated into more complex photonic circuits, and silicon photonics provides a low-cost means to implement low-loss grating structures based on high-resolution deep-ultraviolet lithography. This will enable the design of optical circuits comprising grating filters and Bragg mirrors that are defined simultaneously, thereby minimising cavity length uncertainty. Optical gain and absorption is still an issue in silicon photonics, although there are a number of promising potential solutions emerging, including micro-transfer printing of epitaxial layers, as demonstrated by colleagues at Tyndall National Institute [64].

Colleagues have also recently demonstrated numerically that distributed grating design concepts can be extended to the multi-wavelength domain. These grating filters define discrete combs of transmission channels at predefined wavelengths, which can then be the basis for defining high-performance and integrated mode-locked devices with tailored spectra. The example of Fig. 5.1 illustrates the structure of an open grating resonator that supports three transmission channels spaced at 40 GHz [63]. The wavelength of the central channel in this example is set by the Bragg wavelength at 200 THz frequency [1.5 μm].

The lower panel of Fig. 5.1 shows the transmission of the passive filter plotted on a logarithmic scale. The transmission resonances of the grating are placed accurate to

within 1.5 GHz, and the spacing to within 100 MHz. These resonances of the ideal structure have very narrow linewidths of 180 MHz [Q $\simeq 1.1 \times 10^6$], with an extinction of approximately 40 dB.

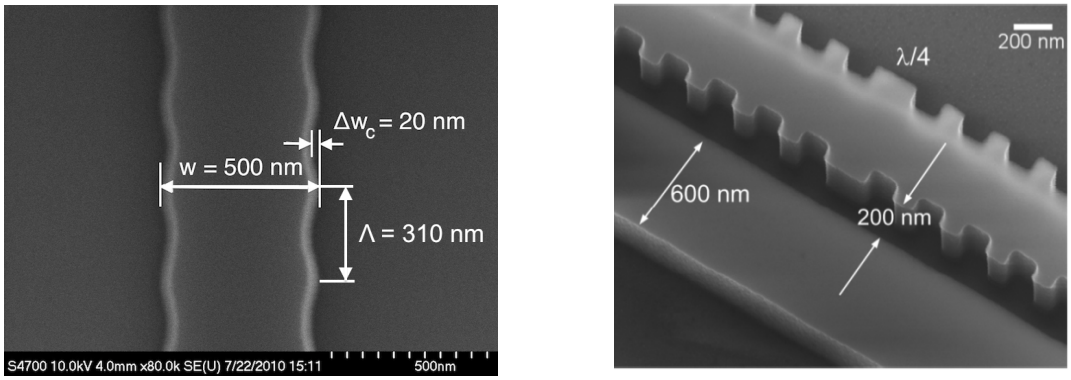

Figure 5.2: Waveguide grating structures fabricated in silicon-on-insulator [65, 66].

The applications potential of this design approach will critically depend on the quality of the grating implementation in a real device. Recent results obtained in silicon-on-insulator sampled strip waveguide gratings have demonstrated coupling constants of $\simeq 50$ cm^{-1}, with negligible scattering losses, fabricated using deep ultraviolet lithography [65, 66]. Examples of grating implementations in silicon photonics waveguides are shown in Fig. 5.2. The fabrication of a non-uniform grating profile, as in Fig. 5.1, using waveguide gratings such as these presents no additional difficulty, when compared with a uniform grating profile. The progress in fabrication platform technology development that these gratings and related devices demonstrate provides strong support for further theoretical and numerical research to support discrete-mode devices and their adaptation to integrated optics.

Bibliography

[1] T. Erneux, "Q-switching bifurcation in a laser with a saturable absorber," *J. Opt. Soc. Am. B*, vol. 5, no. 5, p. 1063, 1988.

[2] P. Vasilev, *Ultrafast Diode Lasers: Fundamentals and Applications*. Artech House Boston, 1995.

[3] S. M. Baer and T. Erneux, "Singular hopf bifurcation to relaxation oscillations," *SIAM Journal on Applied Mathematics*, vol. 46, no. 5, pp. 721–739, 1986.

[4] G. Oppo and A. Politi, "Toda potential in laser equations," *Zeitschrift für Physik B Condensed Matter*, vol. 59, no. 1, pp. 111–115, 1985.

[5] D. Kouznetsov, J. Bisson, J. Li, and K. Ueda, "Self-pulsing laser as oscillator toda: approximations through elementary functions," *Journal of Physics A: Mathematical and Theoretical*, vol. 40, no. 9, p. 2107, 2007.

[6] L. Sulmoni, J. M. Lamy, J. Dorsaz, A. Castiglia, J. F. Carlin, W. Scheibenzuber, U. Schwarz, X. Zeng, D. Boiko, and N. Grandjean, "Static and dynamic properties of multi-section ingan-based laser diodes," *J. Appl. Phys.*, vol. 112, no. 10, 103112, 2012.

[7] A. Klehr, B. Sumpf, K. H. Hasler, J. Fricke, A. Liero, T. Hoffmann, G. Erbert, and G. Tränkle, "High-peak-power pulse generation with GHz repetition rate using a Q-switched 1060nm DBR tapered laser," in *Opto*, pp. 76161J – 76161J, International Society for Optics and Photonics, 2010.

[8] V. Z. Tronciu, M. Yamada, T. Ohno, S. Ito, T. Kawakami, and M. Taneya, "Self-pulsation in an InGaN laser-theory and experiment," *IEEE J. Quantum Electron.*, vol. 39, no. 12, pp. 1509 – 1514, 2003.

[9] T. Miyajima, H. Watanabe, M. Ikeda, and H. Yokoyama, "Picosecond optical pulse generation from self-pulsating bisectional GaN-based blue-violet laser diodes," *Appl. Phys. Lett.*, vol. 94, no. 16, 161103, 2009.

[10] J. Dorsaz, D. L. Boïko, L. Sulmoni, J. F. Carlin, W. G. Scheibenzuber, U. T. Schwarz, and N. Grandjean, "Optical bistability in InGaN-based multisection laser diodes," *Appl. Phys. Lett.*, vol. 98, no. 19, 191115, 2011.

[11] A. M. Yacomotti, S. Haddadi, and S. Barbay, "Self-pulsing nanocavity laser," *Phys. Rev. A*, vol. 87, no. 4, 041804, 2013.

[12] W. G. Scheibenzuber, C. Hornuss, U. T. Schwarz, L. Sulmoni, J. Dorsaz, J.-F. Carlin, N. Grandjean, *et al.*, "Self-pulsation at zero absorber bias in GaN-based multisection laser diodes," *Appl. Phys. Exp.*, vol. 4, no. 6, p. 2702, 2011.

[13] C. Harder, K. Y. Lau, and A. Yariv, "Bistability and pulsations in semiconductor lasers with inhomogeneous current injection," *Quantum Electronics, IEEE Journal of*, vol. 18, no. 9, pp. 1351–1361, 1982.

[14] J. L. Dubbeldam, B. Krauskopf, and D. Lenstra, "Excitability and coherence resonance in lasers with saturable absorber," *Physical Review E*, vol. 60, no. 6, p. 6580, 1999.

[15] D. Rachinskii, A. Vladimirov, U. Bandelow, B. Hüttl, and R. Kaiser, "Q-switching instability in a mode-locked semiconductor laser," *J. Opt. Soc. Am. B*, vol. 23, no. 4, pp. 663 – 670, 2006.

[16] T. Kolokolnikov, M. Nizette, T. Erneux, N. Joly, and S. Bielawski, "The Q-switching instability in passively mode-locked lasers," *Physica D: Nonlinear Phenomena*, vol. 219, no. 1, pp. 13 – 21, 2006.

[17] S. T. Cundiff and J. Ye, "Femtosecond optical frequency combs," *Rev. Mod. Phys.*, vol. 75, pp. 325 – 342, 2003.

[18] D. Z. Kandula, C. Gohle, T. J. Pinkert, W. Ubachs, and K. S. E. Eikema, "Extreme ultraviolet frequency comb metrology," *Phys. Rev. Lett.*, vol. 105, no. 063001, 2010.

[19] T. Rosenband, D. B. Hume, P. O. Schmidt, C. W. Chou, A. Brusch, L. Lorini, W. H. Oskay, R. E. Drullinger, T. M. Fortier, J. E. Stalnaker, S. A. Diddams, W. C. Swann, N. R. Newbury, W. M. Itano, D. J. Wineland, and J. C. Bergquist, "Frequency ratio of AL and HG single-ion optical clocks; metrology at the 17th decimal place," *Science*, vol. 319, no. 5871, pp. 1808 – 1812, 2008.

[20] P. Klopp, U. Griebner, M. Zorn, and M. Weyers, "Pulse repetition rate up to 92 ghz or pulse duration shorter than 110 fs from a mode-locked semiconductor disk laser," *Appl. Phys. Lett.*, vol. 98, no. 7, 071103, 2011.

[21] F. O'Callaghan, D. Bitauld, and S. O'Brien, "Design optimization of passively mode-locked semiconductor lasers with intracavity grating spectral filters," *IEEE J. Quantum Electron.*, vol. 50, no. 11, pp. 863–873, 2014.

[22] Z. Lu, J. Liu, S. Raymond, P. Poole, P. Barrios, and D. Poitras, "312-fs pulse generation from a passive C-band InAs/InP quantum dot mode-locked laser," *Opt. Express*, vol. 16, no. 14, pp. 10835–10840, 2008.

[23] M. Heuck, S. Blaaberg, and J. Mørk, "Theory of passively mode-locked photonic crystal semiconductor lasers," *Opt. Express*, vol. 18, pp. 18003 – 18014, August 2010.

[24] S. Bischoff, M. P. S. andrensen, J. M. andrk, S. D. Brorson, T. Franck, J. M. Nielsen, and A. M. a. andLarsen, "Pulse shaping mechanism in colliding pulse mode locked laser diodes," *Appl. Phys. Lett.*, vol. 67, no. 26, pp. 3877 – 3879, 1995.

[25] U. Keller, "Recent developments in compact ultrafast lasers," *Nature*, vol. 424, no. 6950, pp. 831–838, 2003.

[26] G. New, "Pulse evolution in mode-locked quasi-continuous lasers," *IEEE J. Quantum Electron*, vol. 10, no. 2, pp. 115–124, 1974.

[27] H. Haus, "Theory of mode locking with a slow saturable absorber," *IEEE J. Quantum Electron.*, vol. 11, no. 9, pp. 736–746, 1975.

[28] J. Javaloyes and S. Balle, "Mode-locking in semiconductor fabry-perot lasers," *IEEE J. Quantum Electron.*, vol. 46, no. 7, pp. 1023 – 1030, 2010.

[29] A. G. Vladimirov, D. Turaev, and G. Kozyreff, "Delay differential equations for mode-locked semiconductor lasers," *Opt. Lett.*, vol. 29, no. 11, pp. 1221 – 1223, 2004.

[30] V. Moskalenko, J. Javaloyes, S. Balle, M. Smit, and E. Bente, "Theoretical study of colliding pulse passively mode-locked semiconductor ring lasers with an intracavity mach zehnder modulator," *IEEE J. Quantum Electron.*, vol. 50, no. 6, pp. 415–422, 2014.

[31] S. Srinivasan, A. Arrighi, M. Heck, J. Hutchinson, E. Norberg, G. Fish, and J. Bowers, "Harmonically mode-locked hybrid silicon laser with intra-cavity filter to suppress supermode noise," *IEEE Journal of Selected Topics in Quantum Electronics*, vol. 20, no. 4, pp. 8–15, 2014.

[32] D. Bitauld, S. Osborne, and S. O'Brien, "Passive harmonic mode locking by mode selection in fabry–perot diode lasers with patterned effective index," *Opt. Lett.*, vol. 35, no. 13, pp. 2200–2202, 2010.

[33] S. O'Brien, S. Osborne, D. Bitauld, N. Brandonisio, A. Amann, R. Phelan, B. Kelly, and J. O'Gorman, "Optical synthesis of terahertz and millimeter-wave frequencies with discrete mode diode lasers," *IEEE Transactions on Microwave Theory and Techniques*, vol. 58, no. 11, pp. 3083 – 3087, 2010.

[34] S. O'Brien, S. Osborne, K. Buckley, R. Fehse, A. Amann, E. P. O'Reilly, L. P. Barry, P. Anandarajah, J. Patchell, and J. O'Gorman, "Inverse scattering approach to multiwavelength Fabry-Pérot laser design," *Phys. Rev. A*, vol. 74, no. 42, 063814, 2006.

[35] S. O'Brien, A. Amann, R. Fehse, S. Osborne, E. P. O'Reilly, and J. M. Rondinelli, "Spectral manipulation in Fabry-Perot lasers: Perturbative inverse scattering approach," *J. Opt. Soc. Am. B*, vol. 23, no. 6, pp. 1046–1056, 2006.

[36] D. Bitauld, S. Osborne, and S. O'Brien, "Timing characterization of 100 GHz passively mode-locked discrete mode laser diodes," *Opt. Express*, vol. 19, no. 15, pp. 13989 – 13999, 2011.

[37] S. Osborne, K. Buckley, A. Amann, and S. O'Brien, "All-optical memory based on the injection locking bistability of a two-color laser diode," *Opt. Express*, vol. 17, no. 8, pp. 6293–6300, 2009.

[38] S. Osborne, A. Amann, K. Buckley, G. Ryan, S. P. Hegarty, G. Huyet, and S. O'Brien, "Antiphase dynamics in a multimode semiconductor laser with optical injection," *Phys. Rev. A*, vol. 79, no. 2, 023834, 2009.

[39] S. Balle, "Simple analytical approximations for the gain and refractive index spectra in quantum-well lasers," *Phys. Rev. A*, vol. 57, pp. 1304 – 1312, 1998.

[40] M. Ueno and R. Lang, "Conditions for self-sustained pulsation and bistability in semiconductor lasers," *J. Appl. Phys.*, vol. 58, no. 4, pp. 1689 – 1692, 1985.

[41] J. Dubbeldam and B. Krauskopf, "Self-pulsations of lasers with saturable absorber: dynamics and bifurcations," *Optics Communications*, vol. 159, p. 325, 1999.

[42] H. Haken, *Light: Laser Light Dynamics*. North-Holland Pub. Co., 1985.

[43] F. Arecchi, G. Lippi, G. Puccioni, and J. Tredicce, "Deterministic chaos in laser with injected signal," *Optics Communications*, vol. 51, no. 5, pp. 308–314, 1984.

[44] L. M. Narducci and N. B. Abraham, *Laser physics and laser instabilities*. World Scientific, 1988.

[45] L. Lugiato, L. Narducci, E. Eschenazi, D. Bandy, and N. Abraham, "Multimode instabilities in a homogeneously broadened ring laser," *Phys. Rev. A*, vol. 32, no. 3, p. 1563, 1985.

[46] N. Brandonisio, P. Heinricht, S. Osborne, A. Amann, and S. O'Brien, "Bistability and all-optical memory in dual-mode diode lasers with time-delayed optical feedback," *IEEE Photonics Journal*, vol. 4, no. 1, pp. 95 – 103, 2012.

[47] S. Osborne, P. Heinricht, N. Brandonisio, A. Amann, and S. O'Brien, "Wavelength switching dynamics of two-colour semiconductor lasers with optical injection and feedback," *Semicond. Sci. Technol.*, vol. 27, no. 9, 094001, 2012.

[48] C. R. Mirasso, G. H. M. V. Tartwijk, E. Hernandez-Garcia, D. Lenstra, S. Lynch, P. Landais, P. Phelan, M. S. Miguel, and W. Elsaber, "Self-pulsating semiconductor lasers: Theory and experiment," *IEEE J. Quantum Electron.*, vol. 35, p. 764, 1999.

[49] P. M. Stolarz, J. Javaloyes, G. Mezosi, L. Hou, C. N. Ironside, M. Sorel, A. C. Bryce, and S. Balle, "Spectral dynamical behavior in passively mode-locked semiconductor lasers," *IEEE Photonics Journal*, vol. 3, no. 6, pp. 1067 – 1082, 2011.

[50] A. M. Yacomotti, L. Furfaro, X. Hachair, F. Pedaci, M. Giudici, J. Tredicce, J. Javaloyes, S. Balle, E. A. Viktorov, and P. Mandel, "Dynamics of multimode semiconductor lasers," *Phys. Rev. A*, vol. 69, no. 5, 053816, 2004.

[51] J. R. Karin, R. J. Helkey, D. J. Derickson, R. Nagarajan, D. S. Allin, J. E. Bowers, and R. L. Thornton, "Ultrafast dynamics in field enhanced saturable absorbers," *Appl. Phys. Lett.*, vol. 64, no. 6, pp. 676 – 678, 1994.

[52] J. Mulet, M. Kroh, and J. Mørk, "Pulse properties of external-cavity mode-locked semiconductor lasers," *Opt. Express*, vol. 14, no. 3, pp. 1119 – 1124, 2006.

[53] A. G. Vladimirov and D. Turaev, "Model for passive mode locking in semiconductor lasers," *Phys. Rev. A*, vol. 72, no. 3, 033808, 2005.

[54] C. Otto, K. Lüdge, A. G. Vladimirov, M. Wolfrum, and E. Schöll, "Delay-induced dynamics and jitter reduction of passively mode-locked semiconductor lasers subject to optical feedback," *New Journal of Physics*, vol. 14, no. 11, 113033, 2012.

[55] R. P. Green, M. Haji, L. Hou, G. Mezosi, R. Dylewicz, and A. E. Kelly, "Fast saturable absorption and 10 ghz wavelength conversion in al-quaternary multiple quantum wells," *Optics express*, vol. 19, no. 10, pp. 9737–9743, 2011.

[56] S. Osborne, A. Amann, D. Bitauld, and S. O'Brien, "On-off intermittency in an optically injected semiconductor laser," *Phys. Rev. E*, vol. 85, no. 5, 056204, 2012.

[57] E. Ott, *Chaos in Dynamical Systems*. Cambridge University Press, 2002.

[58] V. Kovanis, A. Gavrielides, T. Simpson, and J.-M. Liu, "Instabilities and chaos in optically injected semiconductor lasers," *Appl. Phys. Lett.*, vol. 67, no. 19, pp. 2780–2782, 1995.

[59] M. J. Feigenbaum, "Universal behavior in nonlinear systems," *Physica D: Nonlinear Phenomena*, vol. 7, no. 1, pp. 16–39, 1983.

[60] C. Bonatto, M. Feyereisen, S. Barland, M. Giudici, C. Masoller, J. R. R. Leite, and J. R. Tredicce, "Deterministic optical rogue waves," *Physical review letters*, vol. 107, no. 5, p. 053901, 2011.

[61] B. Kelleher, C. Bonatto, G. Huyet, and S. Hegarty, "Excitability in optically injected semiconductor lasers: Contrasting quantum-well-and quantum-dot-based devices," *Phys. Rev. E*, vol. 83, no. 2, p. 026207, 2011.

[62] Y. Gu, D. K. Bandy, J.-M. Yuan, and L. M. Narducci, "Bifurcation routes in a laser with injected signal," *Physical Review A*, vol. 31, no. 1, p. 354, 1985.

[63] S. O'Brien, "Comb transmission filters defined by phase-shifted superstructure Bragg gratings," *Opt. Lett.*, vol. 39, no. 4, pp. 1085–1088, 2014.

[64] J. Justice, C. Bower, M. Meitl, M. B. Mooney, M. A. Gubbins, and B. Corbett, "Wafer-scale integration of group III-V lasers on silicon using transfer printing of epitaxial layers," *Nature Photon.*, vol. 6, no. 9, pp. 610–614, 2012.

[65] X. Wang, W. Shi, R. Vafaei, N. A. Jaeger, and L. Chrostowski, "Uniform and sampled bragg gratings in soi strip waveguides with sidewall corrugations," *IEEE Photonics Technology Letters*, vol. 23, no. 5, p. 290, 2011.

[66] V. Veerasubramanian, G. Beaudin, A. Giguère, B. L. Drogoff, V. Aimez, and A. G. Kirk, "Waveguide-coupled drop filters on soi using quarter-wave shifted sidewalled grating resonators," *Opt. Express*, vol. 20, no. 14, pp. 15983–15990, 2012.